



# AGR-5/6/7 Thermal Model with Non-uniform Gas Gaps

October 2023

Grant Hawkes  
Binh Pham  
Courtney Otani  
*Idaho National Laboratory*



*INL is a U.S. Department of Energy National Laboratory  
operated by Battelle Energy Alliance, LLC*

#### **DISCLAIMER**

This information was prepared as an account of work sponsored by an agency of the U.S. Government. Neither the U.S. Government nor any agency thereof, nor any of their employees, makes any warranty, expressed or implied, or assumes any legal liability or responsibility for the accuracy, completeness, or usefulness, of any information, apparatus, product, or process disclosed, or represents that its use would not infringe privately owned rights. References herein to any specific commercial product, process, or service by trade name, trade mark, manufacturer, or otherwise, does not necessarily constitute or imply its endorsement, recommendation, or favoring by the U.S. Government or any agency thereof. The views and opinions of authors expressed herein do not necessarily state or reflect those of the U.S. Government or any agency thereof.



# **AGR-5/6/7 Thermal Model with Non-uniform Gas Gaps**

**Grant Hawkes  
Binh Pham  
Courtney Otani  
Idaho National Laboratory**

**October 2023**

**Idaho National Laboratory  
Advanced Reactor Technologies  
Idaho Falls, Idaho 83415**

**<http://www.art.inl.gov>**

**Prepared for the  
U.S. Department of Energy  
Office of Nuclear Energy  
Under DOE Idaho Operations Office  
Contract DE-AC07-05ID14517**

*Page intentionally left blank*

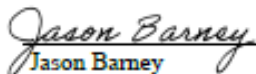
INL ART Program

**AGR-5/6/7 Thermal Model with Non-uniform Gas Gaps**

INL/RPT-23-73074 Rev1

October 2023

Technical Reviewer: (Confirmation of mathematical accuracy, and correctness of data and appropriateness of assumptions.)

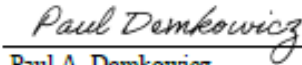


Jason Barney  
Thermal Analyst, Irradiation Experiments Thermal  
Hydraulics Analysis, Department C140

10/18/2023

Date

Approved by:



Paul A. Demkowicz  
AGR Program Technical Director

10/23/2023

Date



Travis R. Mitchell  
INL ART Program Manager

10/23/2023

Date



Michelle T. Sharp  
INL Quality Assurance

10/23/2023

Date

*Page intentionally left blank*

## ABSTRACT

Fuel compact temperatures are a crucial factor in assessing the irradiation performance of tristructural isotropic fuel particles. In the absence of direct measurement, fuel compact temperatures were calculated using a three-dimensional finite-element thermal model, which is subject to simulation uncertainty. The most dominant factor in the uncertainty of calculated fuel temperatures is the gas gap uncertainty due to the nub-to-shell clearance caused by a design error in AGR-5/6/7 capsules. The thermal model was revised to examine the most probable graphite offset position for six different days during the irradiation for Capsules 1 and 2. The analysis varied the offset distance and azimuthal direction at both the top and bottom of the holder. The best-fit offset was estimated based on the minimum root mean square error of the residuals (measured minus calculated) for the operational thermocouples (TCs). These results led to the following conclusions:

- (1) The holder offsets led to slightly lower average temperatures but wider temperature variations (lower minimum and higher peak fuel temperatures) for both Capsule 1 and 2.
- (2) During earlier cycles (162A–164B), when numerous TCs were still operational, the best-fit offset distance varied over a specific range for both the top and bottom (0.002–0.0035 in. for Capsule 1 and 0.003–0.004 in. for Capsule 2). In contrast, the offset azimuthal direction varied widely, especially for the offset at the bottom of the Capsule 1 holder. This is because holder movement was somewhat constrained at the top of Capsule 1 by the TC leads running through the capsule head and into the holder and by the through tubes in Capsule 2, but the Capsule 1 bottom did not have this type of constraint.
- (3) During later cycles, when all TCs failed, applying the maximum possible offset of 0.006 in. to the northwest direction for both the top and bottom resulted in a calculated peak fuel temperature of 1557°C in Capsule 1 (i.e., a 135°C increase from 1422°C with zero offset on September 20, 2019 [166A]); the maximum offset of 0.0068 in. to the south for both top and bottom resulted in a calculated peak fuel temperature of 1110°C in Capsule 2 on April 20, 2020 (i.e., a 116°C increase from 994°C with zero offset [168A]). High peak fuel temperatures in Capsule 1 during Cycle 166A could be the cause of massive particle failure near the end of this cycle.
- (4) Even though the highest temperature at the tip of Type-N TCs, such as TC-1-7, only slightly exceeded 1000°C, the temperature along the TC wire reached as high as 1335°C, assuming an offset of 0.006 in. in the northwest region of the Capsule 1 holder near the end of Cycle 166A. This temperature significantly exceeds the temperature threshold at which TC degradation is expected. The nickel released by degradation contributed to considerable particle failures in Capsule 1. For eight Type-N TCs in Capsule 2, the peak TC line temperature was much lower (i.e., 1029°C for TC-2-5), assuming a maximum offset of 0.0068 in. to the south during Cycle 168A.

*Page intentionally left blank*

# CONTENTS

ABSTRACT.....	vii
ACRONYMS.....	xv
1. INTRODUCTION.....	1
2. ADVANCED GAS REACTOR-5/6/7 EXPERIMENT .....	1
3. THERMAL MODEL FOR AGR-5/6/7 CAPSULES.....	4
3.1 Capsule Configuration .....	4
3.2 Thermal Model Description .....	5
3.3 Thermal Model Inputs.....	7
3.3.1 Fuel Compacts .....	7
3.3.2 Graphite Holders .....	9
3.3.3 Outer Gas Gaps and Gas Mixture .....	12
3.3.4 Heat Rates .....	15
3.3.5 Fast Neutron Fluence .....	16
3.3.6 Thermocouples and Thermocouple Protective Sleeve.....	16
3.3.7 Capsule 1 Spring Thermal Conductivity.....	18
3.3.8 Neolube Thickness.....	19
3.4 Thermal Analysis Results .....	20
4. CAPSULE OFFSET EXAMINATION .....	23
4.1 Thermal Model with Offset Holder.....	23
4.1.1 Offset Model Description.....	23
4.1.2 Runs for Offset Examination .....	25
4.2 Capsule 1 Offset Holder Analysis.....	26
4.2.1 March 3, 2018, ATR Cycle 162B .....	29
4.2.2 July 15, 2018, ATR Cycle 164A.....	33
4.2.3 August 12, 2018, ATR Cycle 164A.....	36
4.2.4 September 20, 2019, ATR Cycle 166A .....	40
4.2.5 Capsule 1 Offset Discussion .....	44
4.3 Capsule 2 Offset Holder Analysis.....	47
4.3.1 March 3, 2018, ATR Cycle 162B .....	49
4.3.2 October 8, 2018, ATR Cycle 164B.....	52
4.3.3 Highest Possible Temperature, April 20, 2020, ATR Cycle 168A.....	55
4.3.4 Capsule 2 Offset Discussion .....	56
5. CONCLUSIONS.....	58
6. REFERENCES.....	59
Appendix A Capsule 1 Compact Temperatures for Zero and Best-fit Offset Calculated for Selected Dates.....	61

Appendix B Capsule 2 Compact Temperatures for Zero and Best-fit Offset Calculated for Selected Dates.....	70
---	----

## FIGURES

Figure 1. AGR5/6/7 northeast flux trap location in the Advanced Test Reactor core cross section.....	2
Figure 2. Schematic view of the AGR-5/6/7 test train rotated 90 degrees from actual orientation (Capsule 1 is at the bottom of the test train). .....	2
Figure 3. AGR-5/6/7 daily average measured TC temperatures. ....	3
Figure 4. Cross sections of the AGR-5/6/7 capsules, showing the compact stacks and through tubes.....	4
Figure 5. Cutaway view of finite element mesh of the entire capsule train (Hawkes 2021). ....	5
Figure 6. Thermal conductivity varying with fast neutron fluence and temperature for Capsules 1 and 5. ....	8
Figure 7. Unirradiated thermal diffusivity of IG-430 nuclear-grade graphite. ....	9
Figure 8. Conductivity multiplier ( $k_{irr}/k_0$ ) varying with temperature ( $^{\circ}\text{C}$ ) and fast neutron fluence (Shibata et al., 2010). ....	11
Figure 9. Coefficient of thermal expansion multiplier ( $\alpha_{irr}/\alpha_0$ ) varying with temperature ( $^{\circ}\text{C}$ ) and fast neutron fluence (Shibata et al., 2010). ....	11
Figure 10. Thermal conductivity of IG-430 varying with temperature ( $^{\circ}\text{C}$ ) and fast neutron fluence. ....	12
Figure 11. Diametric change of the AGR-5/6/7 Capsule 1 graphite holder, plotted with IG-430 graphite specimens, as a function of fast neutron fluence with PIE measurements. ....	13
Figure 12. Diametric change of the AGR-5/6/7 Capsule 2 graphite holder, plotted with IG-430 graphite specimens, as a function of fast neutron fluence with PIE measurements. ....	13
Figure 13. Helium-neon gas mixture thermal conductivity ( $\text{mW}/\text{m}\cdot\text{K}$ ) varying with neon fraction and temperature ( $^{\circ}\text{C}$ ). ....	14
Figure 14. Compact heat rates ( $\text{W}/\text{cm}^3$ ) for cycle 162B, day 20. ....	15
Figure 15. Graphite holders heat rates ( $\text{W}/\text{cm}^3$ ) for cycle 162B, day 20. ....	15
Figure 16. Component heat rates ( $\text{W}/\text{cm}^3$ ) for cycle 162B, day 20. ....	16
Figure 17. Finite element mesh cut-away view of the HGR ( $\text{W}/\text{cm}^3$ ) for TC-1-8 cycle 162B, day 20. ....	17
Figure 18. TC-1-8 cut-away view of the top of the protective sleeve, with HGR ( $\text{W}/\text{cm}^3$ ) contours for cycle 162B, day 20.....	17
Figure 19. TC-1-8 and its protective sleeve (bottom end view), with HGR ( $\text{W}/\text{cm}^3$ ) contours for cycle 162B, day 20. ....	18
Figure 20. CAD model of the Capsule 1 spring.....	18
Figure 21. Temperature contour plot of the spring, with an $800^{\circ}\text{F}$ boundary temperature and $\text{NeF} = 0.75$ .....	19



Figure 22. Effective thermal conductivity of Capsule 1 spring varying with NeF and temperature. ....	19
Figure 23. Temperature contour plot cutaway view of Capsule 1 fuel during Cycle 162B, day 20. ....	20
Figure 24. Daily minimum, maximum, and volume-averaged fuel temperatures (the light-colored dots for Capsule 1 are for the assumed leadout neon fraction [instead of zero]). ....	21
Figure 25. Difference between the measured and the calculated thermocouple temperatures for each capsule. ....	22
Figure 26. Gap calculation diagram, with capsule wall (blue circle) offset h units (x direction) and k units (y direction). ....	24
Figure 27. Temperature contour plots showing a cut section in Capsule 1 at 1.5 in. from the top of graphite holder varying by offset in eight directions, as taken on the second-to-last day of the first ATR irradiation cycle, Cycle 162B (Hawkes 2021). The circles with numbers are the 10 fuel stacks. ....	25
Figure 28. Cross section showing the 17 thermocouples embedded throughout the Capsule 1 graphite holder. ....	27
Figure 29. Capsule 1 thermocouple residuals during the first three cycles, showing the first three selected dates (blue vertical lines). ....	28
Figure 30. Cutaway view of heat generation rate ( $\text{W}/\text{cm}^3$ ) for the Capsule 1 fuel for March 3, 2018 (top left); July 15, 2018 (top right); August 12, 2018 (bottom left); and September 20, 2019 (bottom right). ....	29
Figure 31. Fast neutron fluence ( $1.0 \times 10^{25}$ neutrons/ $\text{m}^2$ ( $E_n > 0.18$ MeV)) for the Capsule 1 holder for March 3, 2018 (top left); July 15, 2018 (top right); August 12, 2018 (bottom left); and September 20, 2019 (bottom right). ....	29
Figure 32. Residuals of 17 TCs as a function of offset direction (Table 2) for the best-fit offset, showing the smallest variation of TC residuals to be at Step 36 for March 3, 2018 (Cycle 162B). ....	31
Figure 33. Average and RMSE residuals from the 17 TCs as a function of offset direction step (Table 2), showing the best offset position to be at Step 36 for March 3, 2018 (Cycle 162B). ....	31
Figure 34. TC residuals of zero and best-fit offset for March 3, 2018 (Cycle 162B). ....	32
Figure 35. Temperature ( $^{\circ}\text{C}$ ) contour plot of the 0.25 in. slice (level 7) in which the highest temperature occurs for March 3, 2018, the best-fit offset position being 0.002 in. top west and 0.0035 in. bottom north. ....	32
Figure 36. Residuals of the eight operational TCs as a function of offset direction (Table 2) for the best-fit offset, showing the smallest variation of TC residuals to be at Step 41 for July 15, 2018 (Cycle 164A). ....	34
Figure 37. Average, RMSE, and standard deviation of TC residuals as a function of offset direction step. ....	34
Figure 38. TC residuals of zero and best-fit offset for July 15, 2018 (Cycle 164A). ....	35
Figure 39. Temperature ( $^{\circ}\text{C}$ ) contour plot of the 0.25 in. slice (level 8) in which the highest temperature occurs for July 15, 2018, the best-fit offset position being 0.003 in. top west and 0.003 in. bottom southeast (Step 41). ....	35

Figure 40. Residuals of the seven operational TCs as a function of offset direction (Table 2) for the best distances, showing the smallest variation of TC residuals to be at Step 45 for August 12, 2018 (Cycle 162B). .....	36
Figure 41. Average, RMSE, and standard deviation of the TC residuals as a function of offset direction step (Table 2), showing the best offset position to be at Step 45 for August 12, 2018 (Cycle 164A). .....	37
Figure 42. TC residuals of zero and best-fit offset for August 12, 2018 (Cycle 164A).....	37
Figure 43. Temperature (°C) contour plot of the 0.25 in. slice (level 8) in which the highest temperature occurred for August 12, 2018, the best-fit offset position being 0.0035 in. top southwest and 0.0035 in. bottom northwest Step 45. ....	38
Figure 44. Residuals of the six operational TCs (TC-1-4 was excluded) as a function of offset direction (Table 2) for the best distances, showing the smallest variation of TC residuals at Step 53 for August 12, 2018 (Cycle 162B). ....	39
Figure 45. Average, RMSE, and standard deviation of the TC residuals (excluding TC-1-4) as a function of offset direction step (Table 2), showing the best offset position to be at Step 53 for August 12, 2018. ....	39
Figure 46. Temperature (°C) contour plot of the 0.25 in. slice (level 8) in which the highest temperature occurs for August 12, 2018, the best-fit offset position being 0.0035 in. top south and 0.0035 in. bottom northwest Step 53 (excludes TC-1-4). ....	40
Figure 47. Surface temperature (°C) of the Capsule 1 holder for September 20, 2019—offset 0.006 in. to NW from four different perspective angles. ....	42
Figure 48. Cutaway view of the Capsule 1 fuel temperature (°C) for Sep 20, 2019—offset 0.006 in. to NW from four different perspective angles. ....	42
Figure 49. Temperature (°C) contour plot of the 0.25 in. slice (level 7) in which the highest temperature occurs for September 20, 2019, with the offset position being 0.006 in. top northwest and 0.006 in. bottom northwest.....	43
Figure 50. Temperature distribution along TC-1-7 from the holder top to tip, for four offset options (zero, 0.002, 0.004, and 0.006 in.) for both the top and bottom shifted northwest for September 20, 2019.....	44
Figure 51. Photo of the holder showing the fuel stacks and major deposits. ....	46
Figure 52. Cross section showing the eight TCs embedded throughout the Capsule 2 holder. ....	47
Figure 53. Capsule 2 TC residuals during the first four cycles, showing the first two selected dates (blue vertical lines). ....	48
Figure 54. Heat generation rates (W/cm <sup>3</sup> ) for the Capsule 2 fuel for March 3, 2018 (left), and Oct 8, 2018 (right). ....	49
Figure 55. Fast neutron fluence ( $1.0 \times 10^{25}$ neutrons/m <sup>2</sup> ( $E_n > 0.18$ MeV) for the Capsule 2 holder for March 3, 2018 (left) and Oct 8, 2018 (right).....	49
Figure 56. Capsule 2 residuals of eight TCs as a function of offset direction (Table 2) for the best-fit offset, showing the smallest variation of TC residuals to be at Step 14 for March 3, 2018 (Cycle 162B).....	50
Figure 57. Capsule 2 average and RMSE residuals from the eight TCs as a function of offset direction step (Table 2), showing the best offset position to be at Step 14 for March 3, 2018 (Cycle 162B).....	51

Figure 58. Capsule 2 TC residuals of zero and best-fit offset for March 3, 2018 (Cycle 162B).	51
Figure 59. Capsule 2 temperature (°C) contour plot of the 0.25 in. slice (level 4) in which the highest temperature occurs for March 3, 2018, the best-fit offset position being 0.004 in. top northeast and 0.003 in. bottom west (Step 14).	52
Figure 60. Capsule 2 residuals of six TCs as a function of offset direction (Table 2) for the best-fit offset, showing the smallest variation of TC residuals to be at Step 5 for October 8, 2018 (Cycle 164B).	53
Figure 61. Capsule 2 average and RMSE residuals from the six TCs as a function of offset direction step (Table 2), showing the best offset position to be at Step 5 for October 8, 2018 (Cycle 164B).	53
Figure 62. Capsule 2 TC residuals of zero and best-fit offset for October 8, 2018 (Cycle 164B).	54
Figure 63. Temperature (°C) contour plot of the 0.25 in. slice (Level 4) in which the highest temperature occurs for October 8, 2018, the best-fit offset position being 0.004 in. top east and 0.003 in. bottom northwest of Capsule 2 holder (Step 5).	54
Figure 64. Temperature (°C) contours of Capsule 2 fuel with each fuel stack one-quarter slice taken out, including the bottom Grafoil (to help with perspective), for April 20, 2020, with top and bottom offset to the south at 0.0068 in.	55
Figure 65. Temperature (°C) along TC-2-5 on April 20, 2020, with the top and bottom offset to the south and magnitude of 0.0068 in.	56

## TABLES

Table 1. Summary of AGR-5/6/7 capsule properties.	5
Table 2. Sixty-five combinations of the top and bottom offset directions per computer run.	26
Table 3. Depth of TC tip in the holder, type or material, and failure cycle for the 17 TCs in Capsule 1.	26
Table 4. Best-fit options for each of the 16 offset distances, best-fit direction, and minimum RMSE for March 3, 2018 (162B). The best-fit option is shaded orange.	30
Table 5. Best-fit options for each of the 24 offset distances, best-fit direction, and minimum RMSE for July 15, 2018 (164A). The best-fit option is shaded orange.	33
Table 6. Best-fit options for each of the 16 offset distances, best-fit direction, and minimum RMSE for August 12, 2018 (164A). The best-fit option is shaded orange.	36
Table 7. Capsule 1 fuel compact temperatures for various offset options for September 20, 2019 (166A).	41
Table 8. Summary of best-fit options for three dates in 2018.	45
Table 9. Capsule 1 fuel compact temperatures for zero and best-fit offset for four selected dates. Red indicates hottest compacts.	46
Table 10. Depth of TC tip in the holder, type or material, and failure cycle for the eight TCs in Capsule 2.	47
Table 11. Capsule 2 best-fit options for each of the nine offset distances, best-fit direction, and minimum RMSE for March 3, 2018 (162B). The best-fit option is shaded orange.	50

Table 12. Capsule 2 best-fit options for each of the nine offset distances, best-fit direction, and minimum RMSE for October 8, 2018 (164B). The best-fit option is shaded orange.....	52
Table 13. Summary of best-fit options for the first two dates in 2018 for Capsule 2.....	56
Table 14. Capsule 2 fuel compact temperatures for zero and best-fit offset for four selected dates. Red indicates hottest compacts.....	57
Table 15. Capsule 1 compact temperature (minimum, maximum, and average) for zero and best-fit offset, calculated for selected dates during the AGR-5/6/7 irradiation.....	62
Table 16. Capsule 2 compact temperature (minimum, maximum, and average) for zero and best-fit offset, calculated for selected dates during the AGR-5/6/7 irradiation.....	71

## ACRONYMS

AGR	Advanced Gas Reactor
ATR	Advanced Test Reactor
ART	Advanced Reactor Technologies Program
CAD	Computer aided drawing
DNE	Dido nickel equivalent
EFPD	Effective full power days
HGR	Heat generation rate
HTGR	High-temperature gas-cooled reactor
INL	Idaho National Laboratory
MCNP	Monte Carlo N-Particle
NDMAS	Nuclear Data Management and Analysis System
NeF	Neon gas fraction
NEFT	Northeast flux trap
PALM	Powered axial locator mechanism
PIE	Post-irradiation examination
RMSE	Root mean square error
TC	Thermocouple
TRISO	Tristructural isotropic fuel

*Page intentionally left blank*

# **AGR-5/6/7 Thermal Model with Non-uniform Gas Gaps**

## **1. INTRODUCTION**

The daily as-run thermal analysis for the Advanced Gas Reactor (AGR)-5/6/7 experiment was documented in ECAR-5633 (Hawkes 2021). A finite element model was created for the entire test train, which consisted of five capsules. The fuel compacts, graphite holders, stainless-steel capsule walls, and all other major components were individually modeled, including all thermocouples (TCs). Daily heat rates for each compact and component in the model were input from daily as-run physics analyses. Daily gas compositions for each capsule were also input. The thermal conductivity of the compacts and graphite holders varied with fast neutron fluence. Gas mixture thermal conductivity was implemented using experimentally attained values from the literature. Fluence and temperature-dependent thermal conductivity was used for the graphite components and the fuel compacts. Radiation heat transfer was implemented. The model was tuned in an attempt to match the TC readings during the first cycle by adjusting the Neolube (graphite lubricant) thickness.

In the original model, gas gaps between the graphite holder and capsule wall were radially uniform, as well as modeled to change with fast neutron fluence and thermal expansion, since the graphite holders are held off the capsule wall by small nubs of graphite every 45 degrees. However, these nubs were machined shorter for the AGR-5/6/7 capsules, leading to a radial clearance of as much as 0.127 mm (0.005 in.) between the outside of the nubs and the capsule wall (nub-to-shell clearance) in all capsules, potentially allowing the holder to shift inside the capsule shell more than intended. While Capsules 2–5 had the through tubes passing through the graphite holders, which could limit the holder shift, Capsule 1 did not have through tubes. Therefore, a non-uniform gas gap was more likely to occur in Capsule 1, due to shifting of the holder.

Seventeen TCs were installed throughout the Capsule 1 holder and eight TCs were in Capsule 2, and their readings before failures were used as a benchmark to establish the optimal non-uniform gas gap when the root mean square error (RMSE) of TC residuals (measured minus calculated TC temperatures) was minimum among a set of various offsets.

## **2. ADVANCED GAS REACTOR-5/6/7 EXPERIMENT**

AGR-5/6/7 was the last in a series of AGR experiments sponsored by the Advanced Reactor Technologies (ART) program and conducted in the Advanced Test Reactor (ATR) at Idaho National Laboratory (INL). To establish the temperature margin for acceptable performance, the primary experimental objectives were to verify the performance of the reference-design fuel for high-temperature gas-cooled reactor (HTGR) normal operating conditions (AGR-5/6) and to explore fuel performance at temperatures substantially beyond those typical of normal operation (AGR-7) (Mitchell 2022). The AGR-5/6/7 test train was inserted into the northeast flux trap (NEFT) location of the ATR core (see Figure 1) in December 2017.

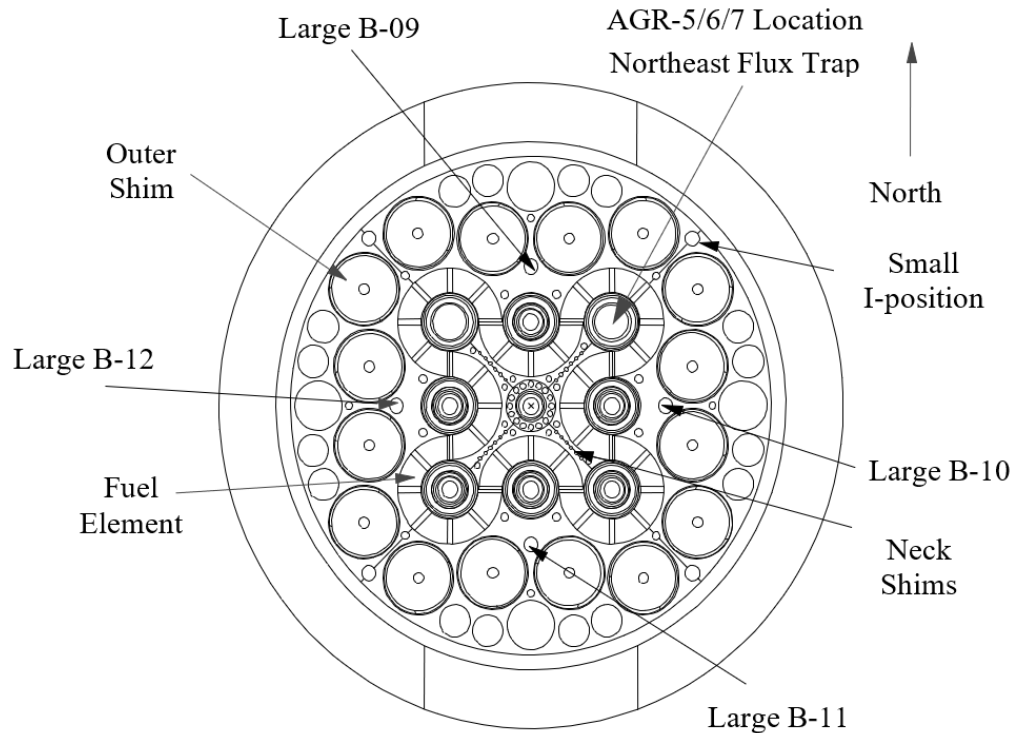


Figure 1. AGR5/6/7 northeast flux trap location in the Advanced Test Reactor core cross section.

AGR-5/6/7 was comprised of five independently controlled and monitored capsules stacked on top of each other to form a test train that used the full 1.22 -m active core height (Figure 2). A stainless-steel lead-out tube held the experiment in position, and both contained and protected the gas lines and TC wiring extending from the test train to the reactor penetration. Capsules 1, 2, 4, and 5 constituted AGR-5/6, while the margin test AGR-7 was associated with Capsule 3. The experiment was instrumented with 54 TCs that terminated in the graphite holders, but 48 had failed by the end of irradiation (Pham et al. 2021). Figure 3 shows the daily average temperatures of all the functioning TCs as a function of effective full power days (EFPDs).

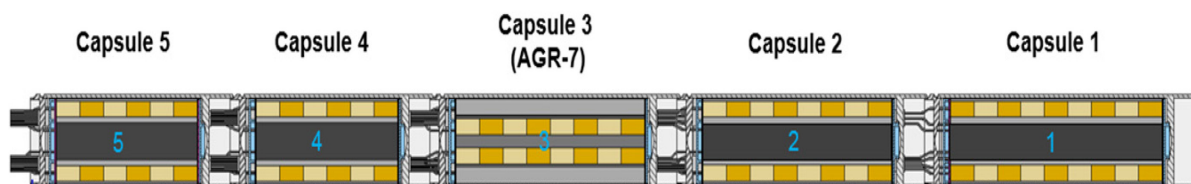


Figure 2. Schematic view of the AGR-5/6/7 test train rotated 90 degrees from actual orientation (Capsule 1 is at the bottom of the test train).



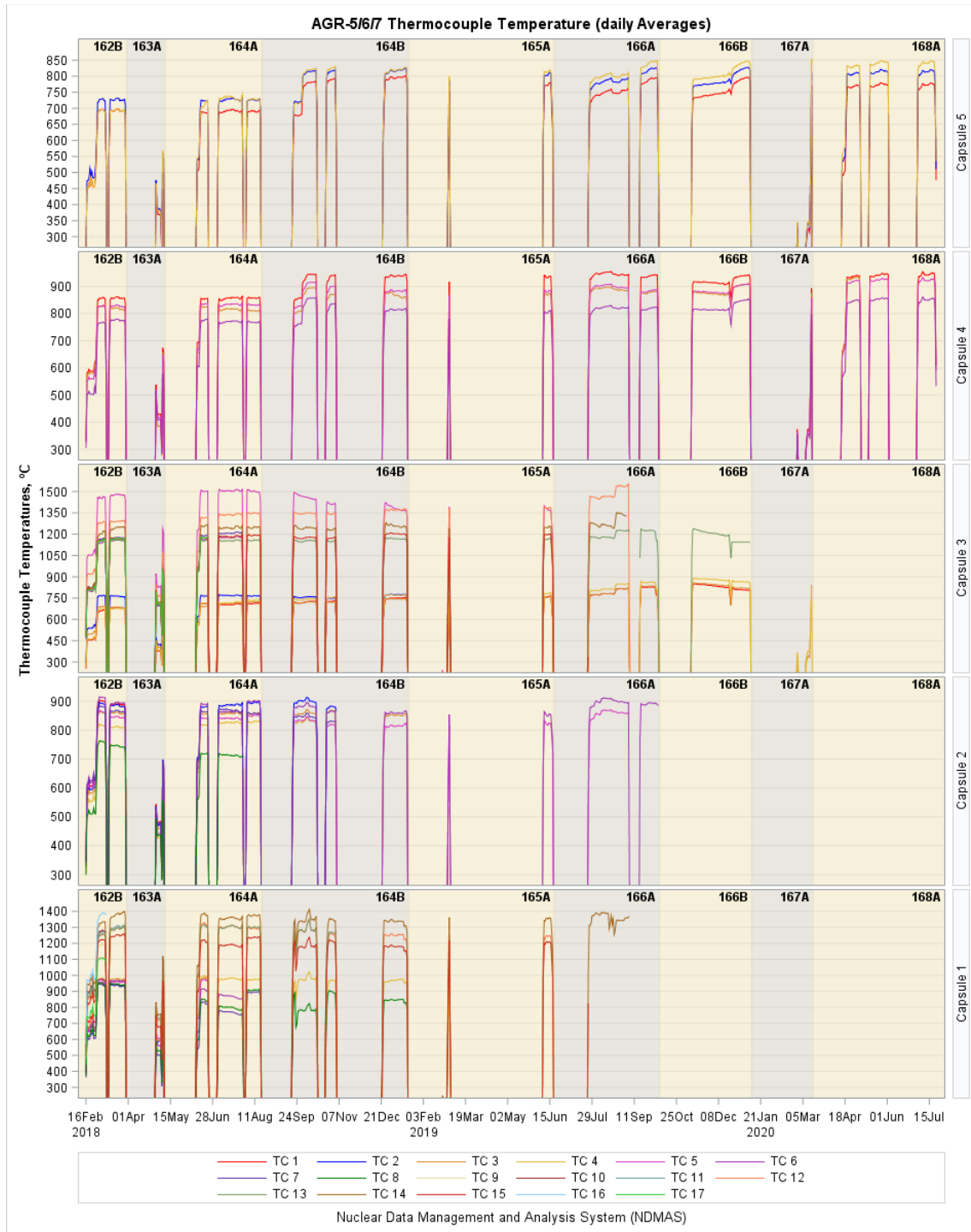


Figure 3. AGR-5/6/7 daily average measured TC temperatures.

### 3. THERMAL MODEL FOR AGR-5/6/7 CAPSULES

#### 3.1 Capsule Configuration

Each capsule contained a number of fuel compacts (Table 1)—each nominally 25.3 mm in length and 12.3 mm in diameter—housed in several stacks within a graphite holder (Figure 4). Capsule 1 had 10 fuel stacks; Capsules 2, 4, and 5 had four stacks located in a hollow-cylinder graphite holder; and Capsule 3 had three stacks arranged in an inner graphite holder to raise the temperature. Through tubes were placed in Capsules 2–5 to hold the TC wires and gas lines. The ATR coolant water flowed downward on the outside of the capsules at approximately 40 ft/s, entering the experiment at 52°C.

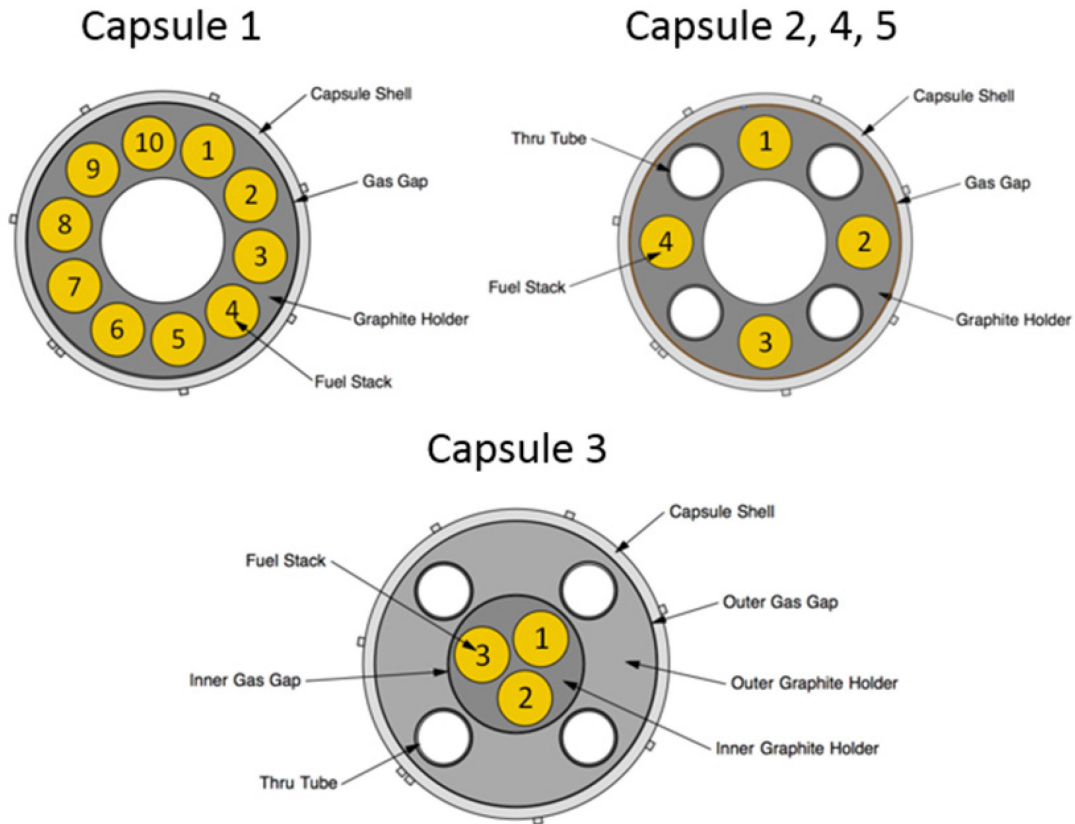


Figure 4. Cross sections of the AGR-5/6/7 capsules, showing the compact stacks and through tubes.

For temperature control, each capsule had an independent gas line to route a helium/neon gas mixture of variable composition. This helium/neon gas mixture flowing through the temperature-control gas gaps between the graphite holder and stainless-steel shell was regulated to maintain target readings for the designated control TC. Periodically, the control TC temperature setpoint was redefined so that the target fuel temperatures remained within the desired range. In addition, fuel temperature control was achieved by adjusting the northeast lobe power and changing the neutron filter on the outside of the experiment for each cycle as the AGR-5/6/7 fuel depleted. The capsule properties are summarized in Table 1. The axially variable temperature-control gas gaps were designed to shape the temperature profile of the compacts. The thermal model exactly matches the drawings with two control gas gap widths (top half and bottom half) for each capsule—except Capsule 3, which had three different gap widths for the control gas gap.

Table 1. Summary of AGR-5/6/7 capsule properties.

	Number of Compacts (levels/stacks)	Number of TCs (installed/failed)	Target Temperature Range (°C)	Avg. Capsule Shell Radii, mm	Avg. Holder Radii, mm
Capsule 5	24 (6/4)	6/3	<900	32.366	32.106
Capsule 4	24 (6/4)	6/3	900–1050	32.373	32.146
Capsule 3	24 (8/3)	17/17	1350–1500	32.365	32.189
Capsule 2	32 (8/4)	8/8	900–1050	32.373	32.188
Capsule 1	90 (9/10)	17/17	900–1350	32.368	32.189

### 3.2 Thermal Model Description

An ABAQUS--based (version 6.14.2) 3-D- finite-element thermal model (Dassault Systèmes, 2014) was created that included each of the five AGR-5/6/7 capsules to predict the daily average temperatures of fuel compacts and TC locations throughout the entire irradiation period during which the ATR core is at power. The ABAQUS thermal model uses a finite element mesh composed of approximately 1,200,000 hexahedral finite-element bricks to estimate temperature profiles for the entire capsule train, as shown in Figure 5. Validation of ABAQUS version 6.14.2 was performed by running a script that modeled 10 different traditional heat transfer textbook problems to validate the different aspects of ABAQUS's heat transfer abilities. The maximum difference between the ABAQUS--calculated values and the exact theoretical values is just under 2.25% (Hawkes 2021).



Figure 5. Cutaway view of finite element mesh of the entire capsule train (Hawkes 2021).

Heat transfer through the gas gaps occurs mainly via conduction (about 80 to 85%) and radiation (about 15 to 20%); the advection is negligible (<0.01%), due to the very low gas flow rate (typically ~50 cm<sup>3</sup>/min). Graphite shrinkage due to the fast neutron fluence and graphite thermal expansion is incorporated into the gas gap model over irradiation time. Thus, gas gap change is a function of fast neutron fluence and thermal expansion. Only conductive heat transfer through the helium-neon gas mixture (used for temperature control), along with surface-to-surface radiation heat transfer, was used in the thermal calculations. The negligible advection heat transfer was omitted.

The governing equation of steady--state conductive heat transfer is expressed as follows (Hawkes et al. 2015):

$$0 = \frac{\partial}{\partial x} \left( k(T) \frac{\partial T}{\partial x} \right) + \frac{\partial}{\partial y} \left( k(T) \frac{\partial T}{\partial y} \right) + \frac{\partial}{\partial z} \left( k(T) \frac{\partial T}{\partial z} \right) + \dot{q} \quad (1)$$

where

$T$  = temperature

$x, y, \text{ and } z$  = directions

$k(T)$  = thermal conductivity, which varies with temperature and neutron fluence

$q$  = heat source.

The governing equation for radiation heat transfer across a gas gap is:

$$q_{net} = \frac{\sigma(T_1^4 - T_2^4)}{\frac{(1-\varepsilon_1)}{\varepsilon_1 A_1} + \frac{1}{A_1 F_{12}} + \frac{(1-\varepsilon_2)}{\varepsilon_2 A_2}} \quad (2)$$

where

- $q_{net}$  = net heat flux
- $\sigma$  = Stephan Boltzmann constant
- $T_1$  and  $T_2$  = surface temperatures
- $\varepsilon_1$  and  $\varepsilon_2$  = emissivities of Surfaces 1 and 2, respectively
- $A_1$  and  $A_2$  = areas of Surfaces 1 and 2, respectively
- $F_{12}$  = view factor from Surface 1 to 2.

The following is a list of assumptions for the original thermal model (Hawkes 2021):

1. Zero graphite holder offset is used given that the actual offset is unknown, due to the 0.127 mm (0.005 in.) clearance between the outside of the nubs and the capsule shell, according to the drawing.
2. All dimensions are based on nominal drawing values, except that the average compact diameter for each fuel stack and the appropriate graphite holder hole were used to calculate the compact-holder gas gap.
3. Gas gaps were modeled as changing linearly with time in response to the IG-430 graphite dimensional change with fast neutron fluence.
4. The thickness of the Neolube (a thin layer of the graphite lubricant coated on the capsule shell surface) was assumed for each capsule during the calibration process. This reduced the gap between the graphite holder and capsule wall by 0.0381 mm in Capsules 1–4, and by 0.0457 mm in Capsule 5.
5. The thermal expansion of the graphite holder (varying with fast neutron fluence and temperature) was calculated using the graphite holder annulus mean radial temperature collected at every 25.4 mm of elevation on the southeast side of the annulus.
6. Compact and various component heat rates were taken from (Sterbentz 2020).
7. Graphite and compact thermal conductivity vary with fluence and temperature, as taken from legacy experiment correlations and scaled for AGR-5/6/7 material density.
8. The gas mixture (helium/neon) thermal conductivity was taken from a report from Brown University (Kestin et al. 1984).
9. Heat transfer through gas occurs via conduction and radiation only; advection is insignificant.
10. Radiation heat transfer occurs across all gas gaps. An emissivity of 0.5 was assumed for stainless steel, 0.90 for the graphite and bottom graphitic material (Grafoil), and 0.52 for the zirconium and zirconia components.
11. The contents of the through tubes were not specifically modeled. A heat flux representing the heat generated from these TCs and gas lines was implemented for each through tube for each capsule.
12. Perfect thermal contact between compacts is assumed.

The following assumptions were adjusted in this revised thermal model, based on observations of AGR-5/6/7 capsule components during post-irradiation examination (PIE) (Stempien and Cai 2023):

1. Find the best-fit offset to minimize the RMSE of TC residuals.
2. The gas gap model changing linearly with fast neutron fluence is based on the PIE graphite holder diameter measurements rather than the shrinkage rate of the AGC graphite specimens.
3. The thickness for the Neolube is zero, as no Neolube was observed on the capsule wall during PIE. It is hypothesized that the volatile components in the Neolube were pyrolyzed during irradiation, and the graphite powder then dropped to the bottom of the capsules soon after the capsule heated up.
4. Thermal expansion of the graphite holder (varying with fast neutron fluence and temperature) was calculated via the graphite holder annulus mean radial temperature. The average of the inner and outer annulus temperatures was used. The outer temperature was available in the subroutine at each finite element node. The inner annual temperature was taken from each directional quadrant (i.e., NE, NW, SW, and SE) at interval heights of 25.4 mm.

### 3.3 Thermal Model Inputs

#### 3.3.1 Fuel Compacts

The fuel compact thermal conductivity was taken from correlations presented by Gontard and Nabielek (Gontard and Nabielek, 1990) for conductivity, considering temperature, temperature of the heat treatment, neutron fluence, and tri-structural isotropic (TRISO)-coated particle packing fraction (with the packing fraction being defined as the total volume of particles divided by the total volume of the compact). The packing fraction for the compacts in Capsules 1 and 5 was measured to be 0.393, while Capsules 2–4 had a value of 0.261.

In this work, the convention used to quantify the neutron damage to a material is neutron fast fluence ( $\text{n/m}^2$ ,  $E_n > 0.18 \text{ MeV}$ , where  $E_n$  is the neutron energy in units of MeV), yet in the work by Gontard and Nabielek, the unit used was the dido nickel equivalent (DNE). To convert from the DNE convention to the fast fluence  $> 0.18 \text{ MeV}$  unit, the following conversion (Konings, 2012) was used:

$$\Gamma_{>0.18\text{MeV}} = 1.52 \Gamma_{\text{DNE}} \quad (3)$$

where  $\Gamma$  is neutron fluence in either the fast fluence  $> 0.18 \text{ MeV}$  unit or DNE. The correlations in the report by Gontard and Nabielek were further adjusted to account for differences in fuel compact density. These correlations were developed for a fuel compact matrix density of  $1750 \text{ kg/m}^3$ , whereas the AGR-5/6/7 compact matrix densities used in the thermal model were  $1728 \text{ kg/m}^3$  for Capsules 1 and 5, and  $1757 \text{ kg/m}^3$  for Capsules 2–4. The thermal conductivities were scaled according to the ratio of densities (0.987 for Capsules 1 and 5, 1.004 for Capsules 2–4) to correct for this difference.

Figure 6 shows a plot of the fuel compact thermal conductivity for Capsules 1 and 5 (varying with fast neutron fluence and temperature), using the Chiew and Gland correlation (Gonzo, 2002), for particles in a matrix described as:

$$\frac{k_e}{k_m} = \frac{1+2\beta\phi + (2\beta^3 - 0.1\beta)\phi^2 + 0.05\phi^3 e^{4.5\beta}}{1-\beta\phi} \quad (4)$$

$$\text{where } \beta = \frac{\kappa - 1}{\kappa + 2} \text{ and } \kappa = \frac{k_p}{k_m}$$

Where

- $k_e$  = effective thermal conductivity
- $k_m$  = matrix thermal conductivity (23.6 W/m-K)
- $k_p$  = particle thermal conductivity (4.13 W/m-K)
- $\phi$  = particle packing fraction.

Capsules 2–4 have a slightly higher thermal conductivity due to the correction factor in Equation 4. For fluences greater than  $1.0 \times 10^{25}$  neutrons/m<sup>2</sup> ( $E_n > 0.18$  MeV), the conductivity increases as fluence increases for  $T \geq 1350^\circ\text{C}$ , because of the annealing of radiation-induced defects in the material at high temperatures. On the other hand, thermal conductivity continually decreases for lower temperatures.

The compacts were assumed to have perfect contact with the Grafoil. The gaps between the compacts and holder were calculated from as-built dimensions. Every compact was measured and compared to each hole in each graphite holder. The exact as-built dimensions were implemented for every stack top half and bottom half. Heat was transferred via gap conductance and gap radiation. Gap radiation between the compacts and graphite holder was implemented, with both surfaces having an emissivity of 0.9.

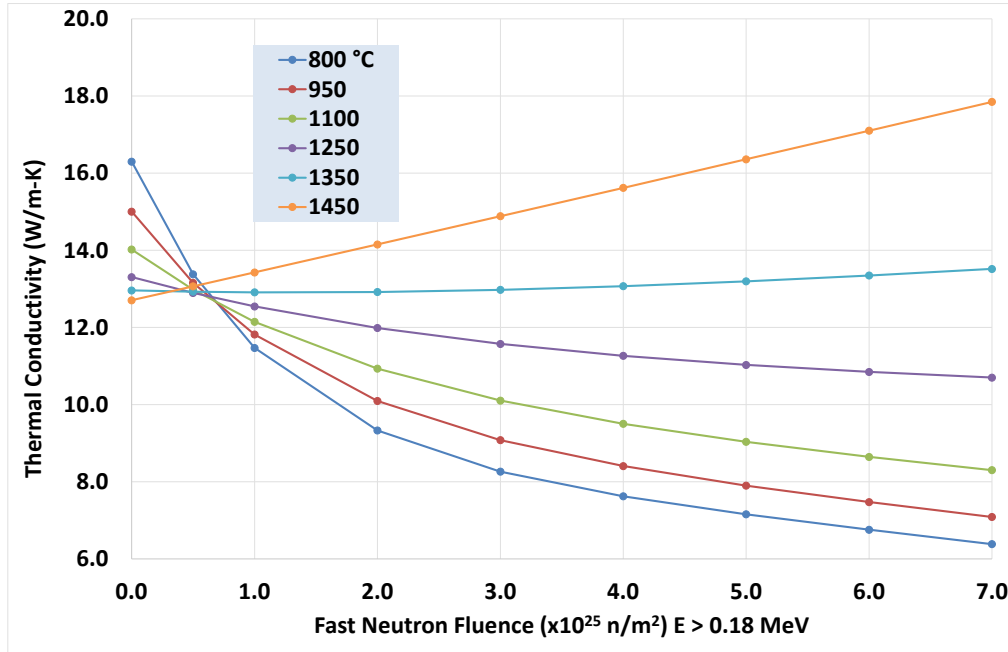


Figure 6. Thermal conductivity varying with fast neutron fluence and temperature for Capsules 1 and 5.

### 3.3.2 Graphite Holders

The AGR-5/6/7 graphite holders were made of IG-430 nuclear-grade graphite. The material properties for unirradiated graphite IG-430 were determined as follows: specific heat values as a function of temperature were taken from the American Society for Testing and Materials (2014); density and expansion coefficients were taken from Windes et al. (2013) and Swank et al. (2010); and unirradiated thermal diffusivities for IG-430 nuclear-grade graphite at a temperature range of 20–1000°C were taken from Windes et al. (2013) and extrapolated to higher temperatures (Figure 7).

The specific heat equation (with temperature in Kelvin) is expressed as:

$$c_p = \frac{1}{11.07 \cdot T^{-1.644} + 0.0003688 \cdot T^{0.02191}} \left( \frac{J}{kg \cdot K} \right) \quad (5)$$

Graphite density equations accounting for thermal expansion at high temperature are as follows:

$$\Delta L = \alpha L(T - T_0), \quad \rho(T) = \rho_0 \frac{V_0}{V(T)}, \quad V_0 = L_0^3, \quad V(T) = (L_0 + \Delta L)^3$$

$$\rho(T) = \frac{\rho_0}{[1 + \alpha(T - T_0)]^3} \quad (6)$$

where

$T_0 = 20^\circ\text{C}$  (room temperature)

$\rho_0 = 1.815 \text{ g/cm}^3$

$\alpha_0 = 5.5\text{e-}6 \text{ (1/}^\circ\text{C)}$  were taken from Windes et al (2017) and Swank et al. (2010), respectively.

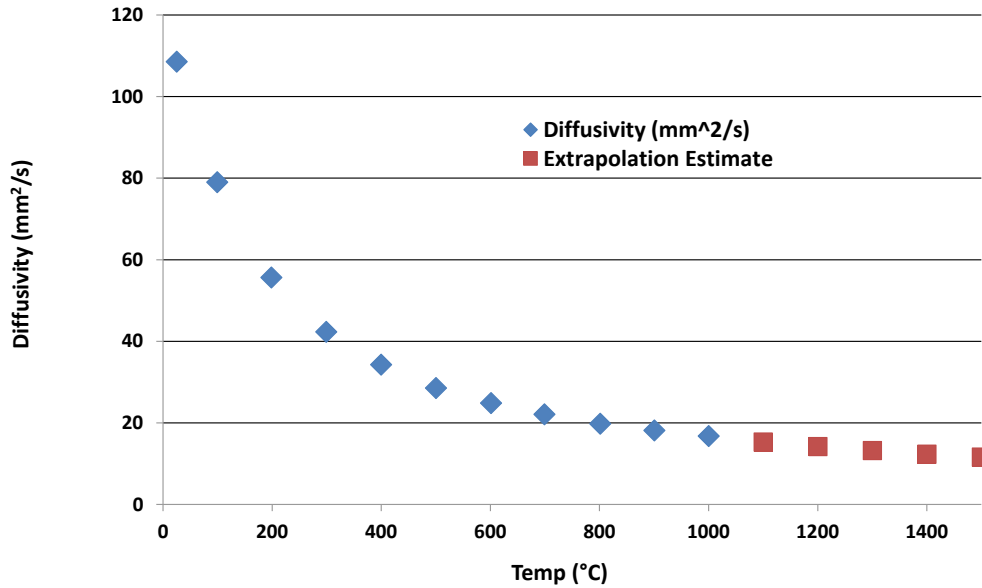


Figure 7. Unirradiated thermal diffusivity of IG-430 nuclear-grade graphite.

Unirradiated thermal conductivity as a function of temperature is calculated as the product of the diffusivity, specific heat (Equation 5), and density (Equation 6). The effect of irradiation on graphite thermal properties was accounted for by incorporating multipliers for thermal conductivity and thermal expansion, expressed as a function of temperature and fast neutron fluence. These multipliers were taken from the Japanese multiplier data (Shibata et al. 2010) and used to adjust the density and thermal conductivity of the graphite holders under actual irradiation conditions. To convert the Japanese multiplier data from dpa to fast neutron fluence, a conversion multiplier of  $0.763 \times \text{fluence} = \text{dpa}$  (fluence units scaled by  $1 \times 10^{25}$ ) was implemented. This multiplier is specific to the NEFT of ATR. The fluence energy band was  $E > 0.18 \text{ MeV}$  and has units of  $1 \times 10^{25} \text{ n/m}^2$ . To convert from the Japanese fast fluence of  $E > 0.10 \text{ MeV}$  to  $E > 0.18 \text{ MeV}$ , a multiplier of 0.9 was used ( $0.9 \times E > 0.10 \text{ MeV} = E > 0.18 \text{ MeV}$ ).

Figure 8 shows a graph of the conductivity multiplier (Shibata et al., 2010) varying with temperature and fast neutron fluence. Equation 7 shows the curve fit developed from these data:

$$\frac{k_{irr}}{k_0} = (p_1 + p_2 \cdot T) + [1 - (p_1 + p_2 \cdot T)] \cdot \exp\left(\frac{-F \cdot T}{p_3 + p_4 \cdot T + p_5 \cdot T^2}\right)$$

$$p_1 = 3.100\text{e-}02, p_2 = 5.613\text{e-}04, p_3 = 1.29077\text{e+}02, p_4 = -9.310\text{e-}01, p_5 = 1.826\text{e-}03 \quad (7)$$

where

$T$  = temperature in °C

$F$  = fast neutron fluence ( $\times 10^{25} \text{ n/m}^2$ ,  $E > 0.18 \text{ MeV}$ ).

Parameters  $p1$  through  $p5$  are listed in the equation.

Figure 9 shows a graph of the coefficient of thermal expansion multiplier (Shibata et al., 2010) varying with temperature and fast neutron fluence. Equation 8 shows the curve fit developed from these data:

$$\frac{\alpha_{irr}}{\alpha_0} = 1 + (p_1 + p_2 \cdot T) \cdot F + p_3 \cdot T \cdot F^2 + (p_4 + p_5 \cdot T) \cdot F^3$$

$$p_1 = 1.050\text{e-}01, p_2 = -2.974\text{e-}05, p_3 = -2.298\text{e-}05, p_4 = -3.007\text{e-}04, p_5 = 1.350\text{e-}06 \quad (8)$$

where

$T$  = temperature in °C

$F$  = fast neutron fluence ( $\times 10^{25} \text{ n/m}^2$ ,  $E > 0.18 \text{ MeV}$ ).

Parameters  $p1$  through  $p5$  are listed in the equation.



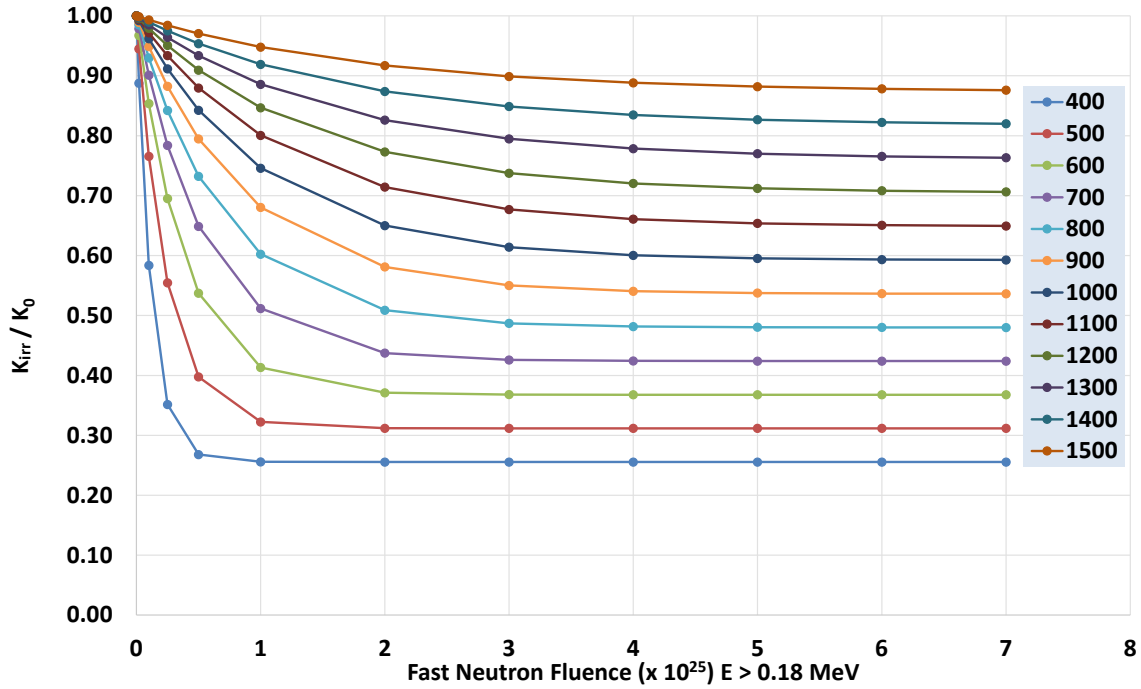


Figure 8. Conductivity multiplier ( $\kappa_{irr}/\kappa_0$ ) varying with temperature ( $^{\circ}\text{C}$ ) and fast neutron fluence (Shibata et al., 2010).

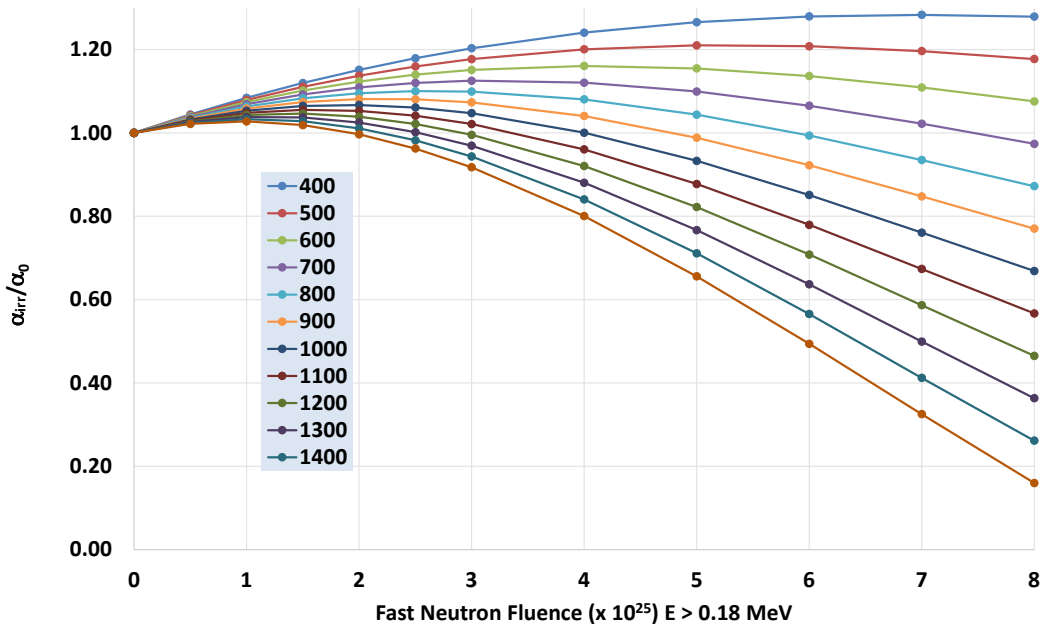


Figure 9. Coefficient of thermal expansion multiplier ( $\alpha_{irr}/\alpha_0$ ) varying with temperature ( $^{\circ}\text{C}$ ) and fast neutron fluence (Shibata et al., 2010).

Figure 10 shows the thermal conductivity of IG-430 varying with temperature and fast neutron fluence, incorporating the thermal expansion multiplier and conductivity multiplier. Note the very fast drop off in conductivity for low temperature and low fast neutron fluence. Almost no change in thermal conductivity for fluence above  $3 \times 10^{25}$  is seen, as the graphite appears to remain stable.

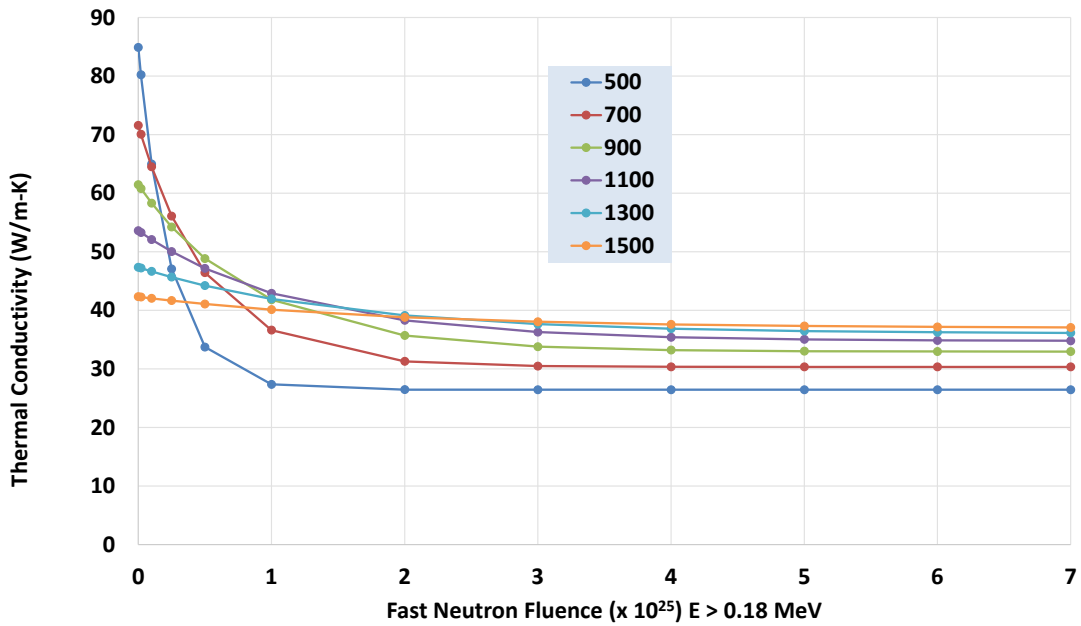


Figure 10. Thermal conductivity of IG-430 varying with temperature (°C) and fast neutron fluence.

### 3.3.3 Outer Gas Gaps and Gas Mixture

The graphite holders undergo neutron damage as irradiation progresses. The graphite also shrinks until a turnaround point, then starts to swell. For the AGR-5/6/7 experiment, this turnaround point was not reached. During PIE, the outer diameter of the graphite holders was measured at three locations that were each exposed to different neutron fast fluence (Stempien and Cai, 2023). As with the previous AGR experiments, the actual rate of diameter change derived from the available PIE dimension measurements [(PIE-Fabrication)/PIE] improved the agreement between the measured and calculated TC temperatures (Hawkes et al., 2012, 2015, 2017). Figure 11 shows diameter changes of the Capsule 1 holder and the IG-430 specimens taken from Windes (2012) as function of fast neutron fluence. The linear equation of fluence from the trend line with zero intercept (green dashed line) was used to calculate the gas gap over the entire irradiation period and includes PIE measurements. The rate of change with fast neutron fluence for the Capsule 1 holder (-0.00120 per unit of fluence) was close to that for the IG-430 specimens (-0.00143 per unit of fluence). These plots also show changes of the inner diameter for IG-430 graphite specimens (blue), which increased with fast fluence increase. Note that only the graphite holder outer diameter was used in the Capsule 1 thermal model.

Figure 12 shows diameter changes of the Capsule 2 holder and the IG-430 specimens taken from Windes (2012) as function of fast neutron fluence. The linear equation of fluence from the trend line with zero intercept (green dashed line) was used to calculate the gas gap over the entire irradiation period and includes PIE measurements. The slope for the Capsule 2 holder was (-0.0005 per unit of fluence) and is about 42% as much as the slope for the Capsule 1 holder.

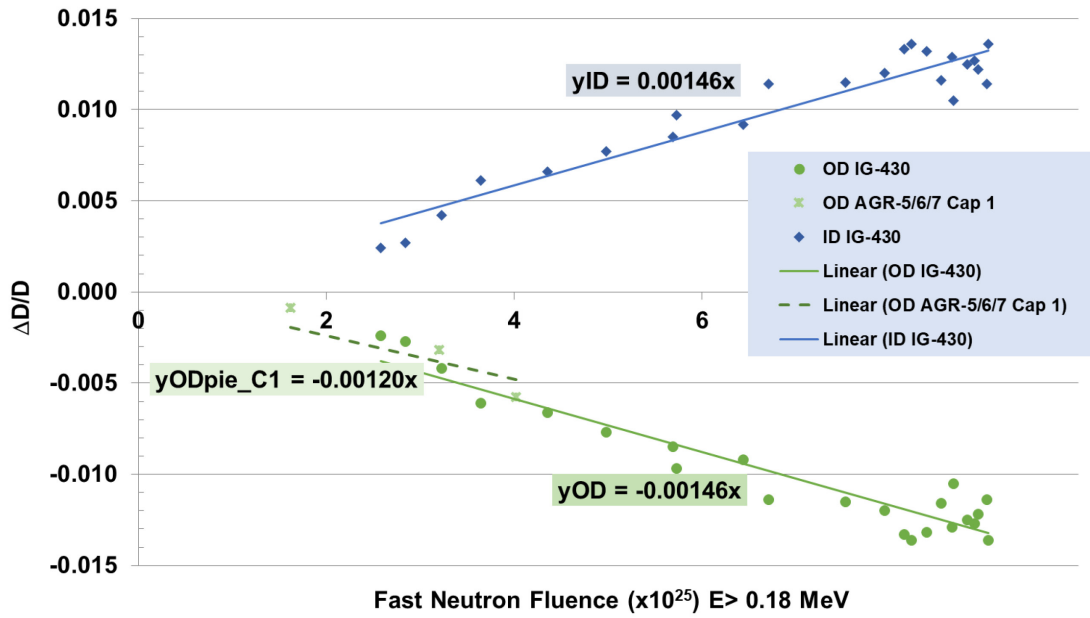


Figure 11. Diametric change of the AGR-5/6/7 Capsule 1 graphite holder, plotted with IG-430 graphite specimens, as a function of fast neutron fluence with PIE measurements.

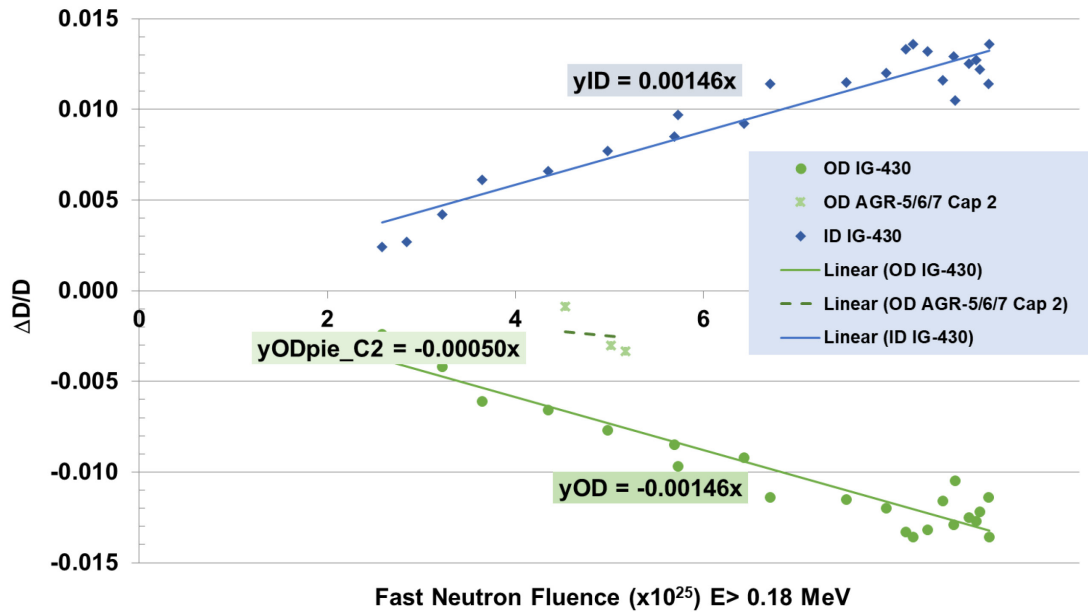


Figure 12. Diametric change of the AGR-5/6/7 Capsule 2 graphite holder, plotted with IG-430 graphite specimens, as a function of fast neutron fluence with PIE measurements.

The capsule neon gas fraction (NeF) for each day was calculated by using daily-average flow rates for the helium and neon passing through each capsule. These daily values are stored in the Nuclear Data Management and Analysis System (NDMAS) database for the AGR-5/6/7 experiment (NDMAS, 2021). As discussed in (Pham et. al., 2021), the Capsule 1 gas mixture for cycle 168A was unknown because of a

leak between Capsule 1 and the lead out. The other capsule gas flows were always known. Therefore, two different bounding gas mixtures for Capsule 1 were used in the model: (1) a NeF of zero to match the gas that was purged through the capsule prior to the start of the cycle, and (2) the same gas mixture as the leadout, to accommodate the possibility that the lead out gas could infiltrate Capsule 1. The helium-neon gas mixture thermal conductivity as a function of NeF and temperature was taken from (Kesten et al., 1984) and is shown in Figure 13.

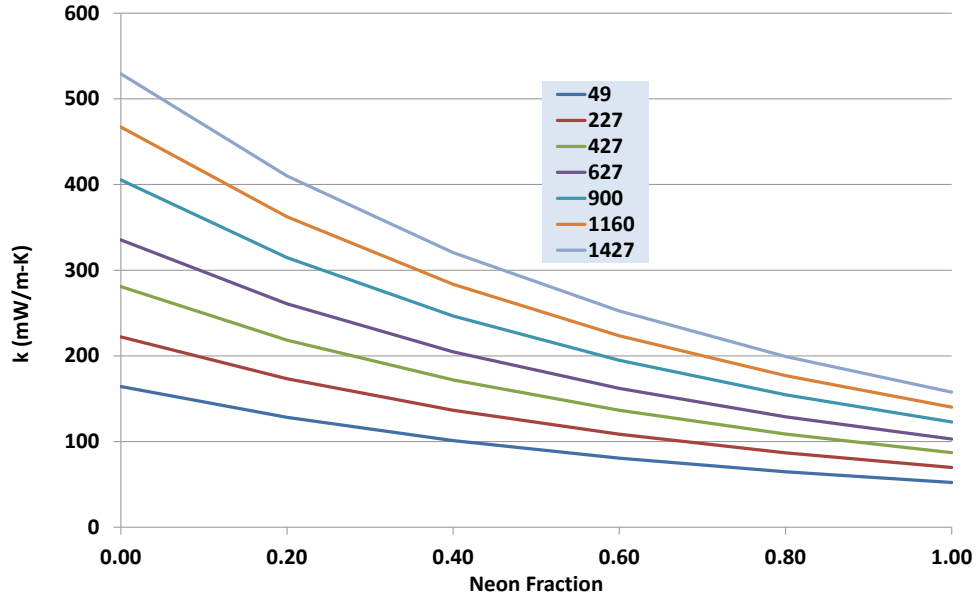


Figure 13. Helium-neon gas mixture thermal conductivity (mW/m-K) varying with neon fraction and temperature (°C).

The gap conductance user subroutine was used to calculate the heat transfer across the gap between the outside of the graphite holders and the stainless-steel capsule wall. The surface temperatures of the holder and capsule are made available to the subroutine. Equation 9 shows how to calculate the gap conductance across this gap:

$$gap = \{r_o[\alpha(T_i - T_o) + 1]\}, ss - \left\{r_o \left[1 + \frac{\Delta r}{r} F + \alpha(F, T)(T_i - T_o)\right]\right\}, holder$$

$$gap \text{ conductance} = \frac{k_{gas}(NeF, T)}{gap}, \text{ where } T = \frac{T_{i,ss} + T_{i,holder}}{2}$$

$$\text{where } T_{i,holder} = \frac{T_{inside,holder} + T_{outside,holder}}{2} \quad (9)$$

where the subscript  $i$  is for instantaneous, and the subscript  $o$  is for room temperature,  $\Delta r/r$  is the slope from Figure 11 and Figure 12,  $k_{gas}(T)$  is the gas mixture thermal conductivity, and  $\alpha(F, T)$  is described in Section 3.3.2. The average temperature between the inner and outer surface of the graphite holder is used. Since the inside surface temperature is not available in the subroutine, a vector of the inside surface temperature (inside of annulus) for each directional quadrant (NE, NW, SW, SE) taken at 25.4 mm elevations (i.e., nine total for Capsule 1, and eight for Capsule 2) was obtained from the volumetric heat subroutine and passed into the gap conductance subroutine. Only the gap between the outside of the graphite holder and the capsule wall is discussed here. Note that there is an additional gap between the inner and outer holders in Capsule 3 and the gap conductance is calculated in the same manner.

### 3.3.4 Heat Rates

Heat rates specific to the AGR-5/6/7 experiment were taken from results generated using the Monte Carlo N-Particle (MCNP) code (MCNP, 2017) and are given in (Sterbentz, 2020). The heat rates were imported into the ABAQUS input file for each ¼ inch axial segment of a compact (heat generated from fission) and for each 1.0 in. of height of the graphite holders (gamma heating) for every day during irradiation. Gamma heat rates were also imported for the water, stainless-steel capsules, through tubes, TCs, and all the various components on the top and bottom of each capsule. Figure 14 shows volumetric heat generation rates (HGRs) for all the compacts, imported from the physics calculations during the first ATR cycle (162B) on the 20<sup>th</sup> day of irradiation. The fuel heat rates ranged from the highest heat rate (166 W/cm<sup>3</sup>) at the top of Capsule 1 to the lowest heat rate (61 W/cm<sup>3</sup>) at the bottom of Capsule 1. The gamma heat rates for the graphite holders exhibit a typical chopped cosine profile, and they are displayed (for the same day) in Figure 15 with the peak being 7.02 W/cm<sup>3</sup> and the minimum being 2.29 W/cm<sup>3</sup>. Component heat rates for all other components in the model are shown in Figure 16. In this figure, the contour color scale was adjusted to create a more even color spread, since the components in Capsule 3 generate considerable heat compared to the rest of the components.

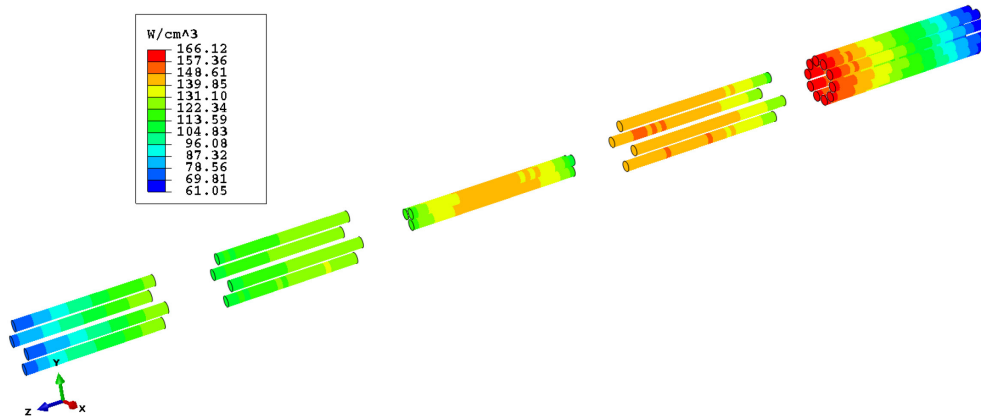


Figure 14. Compact heat rates (W/cm<sup>3</sup>) for cycle 162B, day 20.

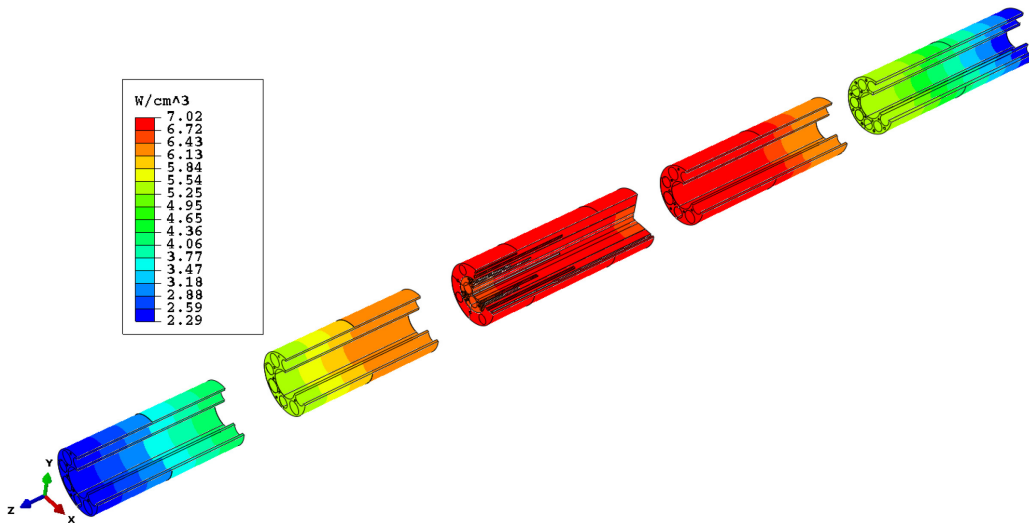


Figure 15. Graphite holders heat rates (W/cm<sup>3</sup>) for cycle 162B, day 20.

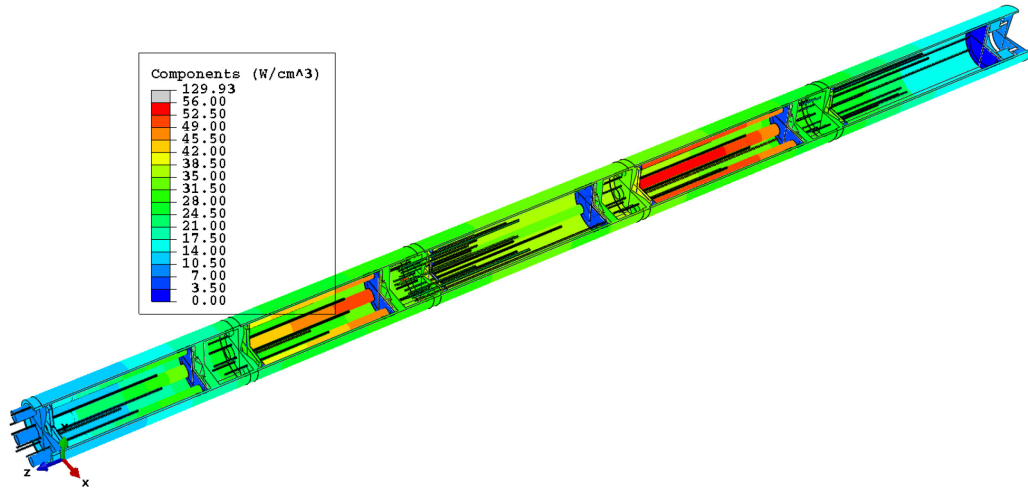


Figure 16. Component heat rates ( $\text{W}/\text{cm}^3$ ) for cycle 162B, day 20.

### 3.3.5 Fast Neutron Fluence

Fast neutron fluence ( $E > 0.18 \text{ MeV}$ ) was imported from the physics calculations for each 1/4 of a compact and each 1.0 in. of height of graphite holders for each day of irradiation. The thermal conductivities of the compact and graphite holder depend on fast neutron fluence, via the coefficient of thermal expansion multiplier and conductivity multiplier, as functions of temperature and fast neutron fluence.

### 3.3.6 Thermocouples and Thermocouple Protective Sleeve

Each TC and TC sleeve were individually modeled and placed in the correct location according to the capsule drawings. Perfect contact was assumed where the TCs were brazed to the top cap. An appropriate gap conductance was applied between each TC and its protective sleeve, and between each protective sleeve and the graphite holder. The TC temperature was taken as the average of the finite element temperatures at the tip of each TC. An adiabatic boundary condition was assumed between the tip of the TC and the graphite holder, because there was a small gap between the end of the TC and the graphite. All heat transfer was assumed to be radial. A daily individual heat generation rate for each 1.0 in. of each TC and TC protective sleeve was implemented from the neutronics calculations. Figure 17, Figure 18, and Figure 19 show the finite element mesh of TC-1-8 and its protective sleeve, with color contours for HGRs, each of which pertain to the same day.

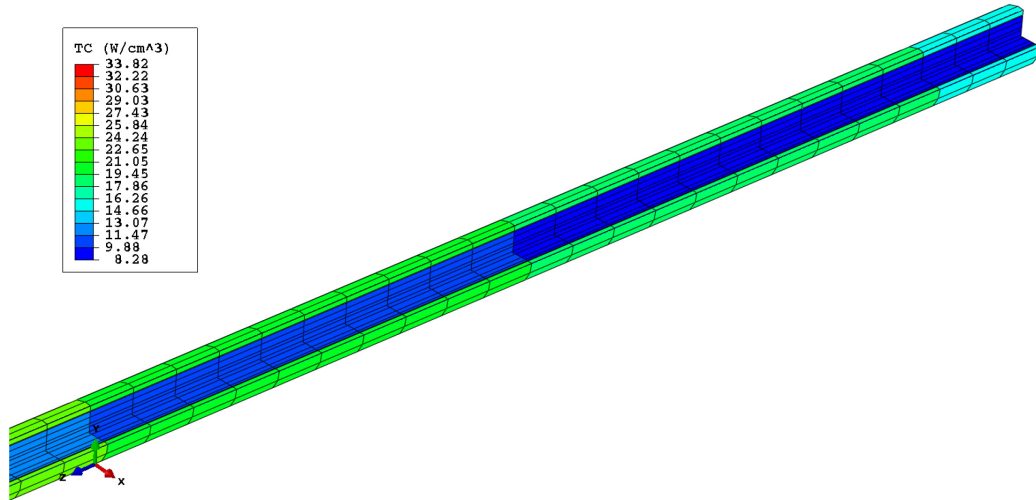


Figure 17. Finite element mesh cut-away view of the HGR ( $\text{W}/\text{cm}^3$ ) for TC-1-8 cycle 162B, day 20.

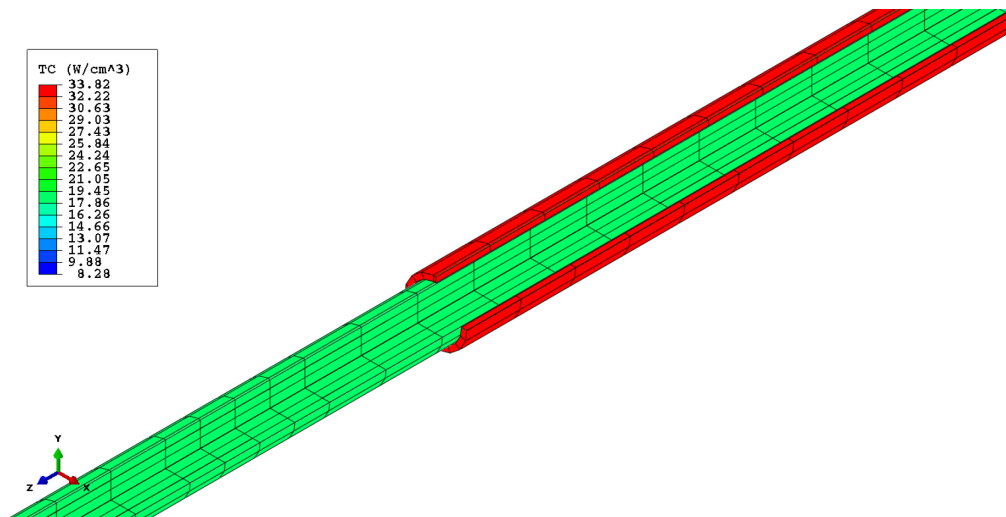


Figure 18. TC-1-8 cut-away view of the top of the protective sleeve, with HGR ( $\text{W}/\text{cm}^3$ ) contours for cycle 162B, day 20.

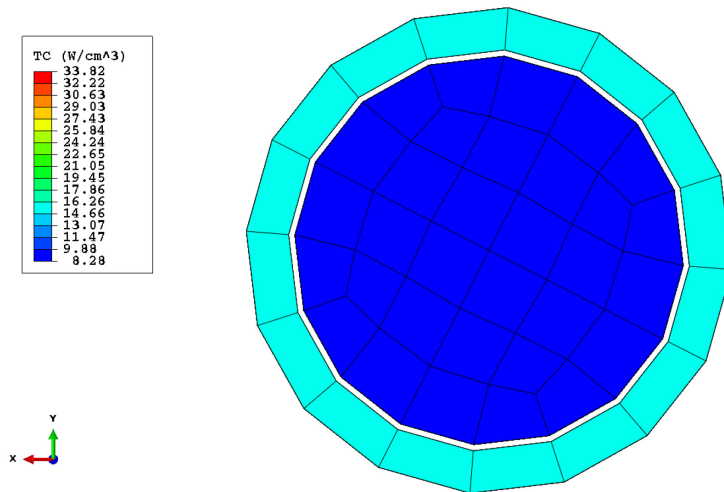


Figure 19. TC-1-8 and its protective sleeve (bottom end view), with HGR ( $\text{W}/\text{cm}^3$ ) contours for cycle 162B, day 20.

### 3.3.7 Capsule 1 Spring Thermal Conductivity

An effective thermal conductivity of the spring located at the bottom of Capsule 1 (only capsule with a spring) was calculated with consideration of the gas composition and radiation heat transfer. Furthermore, a finite element model of the spring by itself was created. This effective thermal conductivity method was used so that a simple mesh could be placed where the spring exists, without incorporating the complex geometry of the spring into the full model of the test train. A temperature boundary condition was placed on the bottom, while a heat flux was placed on the top. A series of runs was performed using various temperature boundary conditions for the relevant gas mixtures. Figure 20 shows a computer-aided drawing (CAD) model of the spring, which was made from the nickel alloy X750. Figure 21 shows the finite element mesh and temperature contour plot of the spring for a boundary condition of  $800^\circ\text{F}$  and a NeF of 0.75. The average temperature between the minimum and maximum was used as the data point for this configuration. Figure 22 shows the effective thermal conductivity plot varying with NeF and temperature for the spring. Data for X-750 is also plotted on the graph.

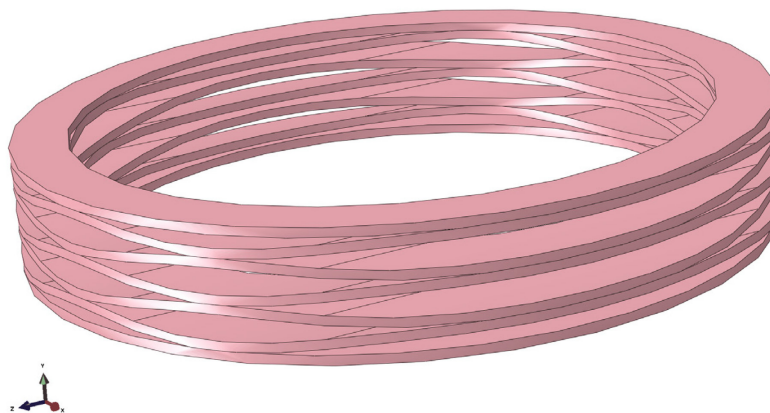


Figure 20. CAD model of the Capsule 1 spring.



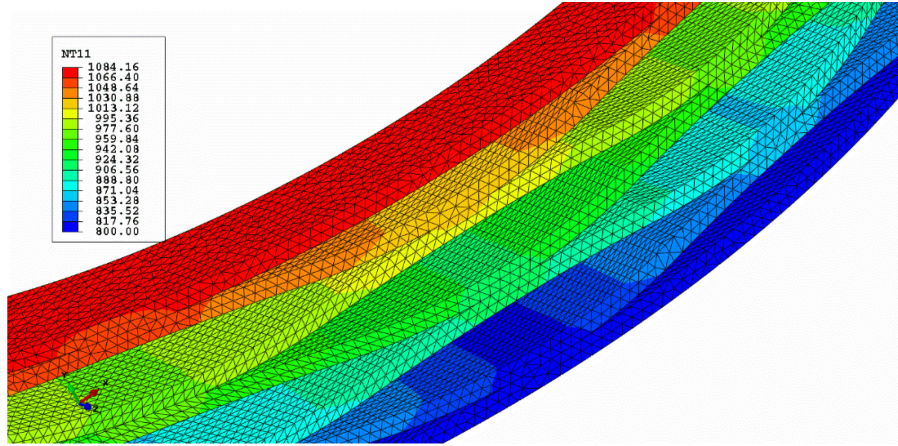


Figure 21. Temperature contour plot of the spring, with an 800°F boundary temperature and NeF = 0.75.

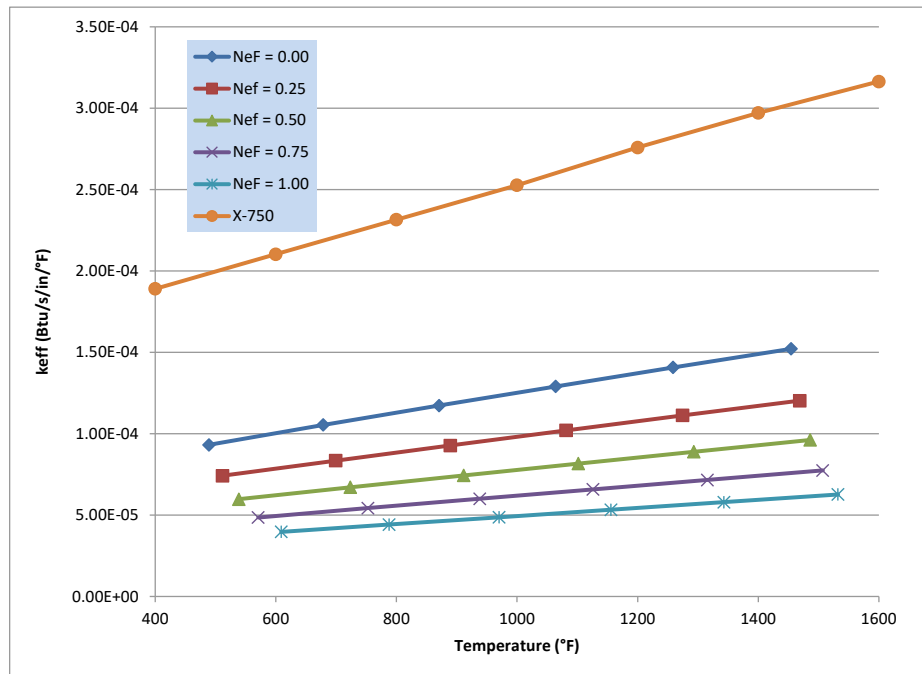


Figure 22. Effective thermal conductivity of Capsule 1 spring varying with NeF and temperature.

### 3.3.8 Neolube Thickness

The graphite lubricant Neolube was brushed on the inside of the stainless-steel capsule wall to reduce friction during assembly of the capsule and to increase the emissivity of the capsule. The thermal model incorporated this lubricant and reduced the size of the gas gap between the outside of the graphite holder and the capsule wall. Various runs were made after Cycle 162B, and different thicknesses were applied to reduce the measured-minus-calculated temperature differences. Originally, the following Neolube thicknesses were used in the thermal model for all cycles: 0.0015 in. for Capsules 1–4, and 0.0018 in for Capsule 5. However, PIE observations of the capsule holder and shell revealed no Neolube present, and it was believed that the volatile components of the Neolube were pyrolyzed when the capsules were operating and the remaining powder dropped to the bottom of the capsules. For this reason, the Neolube thickness is zero in all capsules for this thermal model revision.

### 3.4 Thermal Analysis Results

The main time-series inputs to the model are daily-component-specific (fuel compacts, graphite holders, and other components) heat rates and fast neutron fluences calculated from the as-run depletion analysis (Sterbentz 2020), as well as the daily gas composition of the helium/neon mixture (neon fraction). For example, Figure 23 presents, in a cutaway view, an example of the temperature distribution in Capsule 1 compacts (Hawkes 2021). The fuel temperatures in Capsule 1 varied over a wide range in the original model calculations [683 to 1325°C] because of non-uniform heating across its tall stacks of fuel (nine compacts each). The calculated daily average fuel compact maximum, average, and minimum temperatures as a function of irradiation day (Figure 24) indicated that the fuel temperatures for all the capsules were stable throughout the irradiation, except during a few short periods when the test trains were forced to run on pure helium (i.e., powered axial locator mechanism [PALM] Cycles 163A and 167A, or Cycle 168A for Capsule 1 when its gas line was isolated).

The model-calculated daily temperature for each TC, along with the TC readings during the first cycle (162B), were used for this model calibration, adjusting input parameters within their expected ranges to achieve the best match between the measured and the calculated TC temperatures. Figure 25 shows a history plot of the TC residual temperatures (measured minus calculated) for all EFPDs for all cycles. A modest match between the calculated and the measured TC temperatures during the first cycle was achieved, and similar results are seen for Cycles 163A–168A.

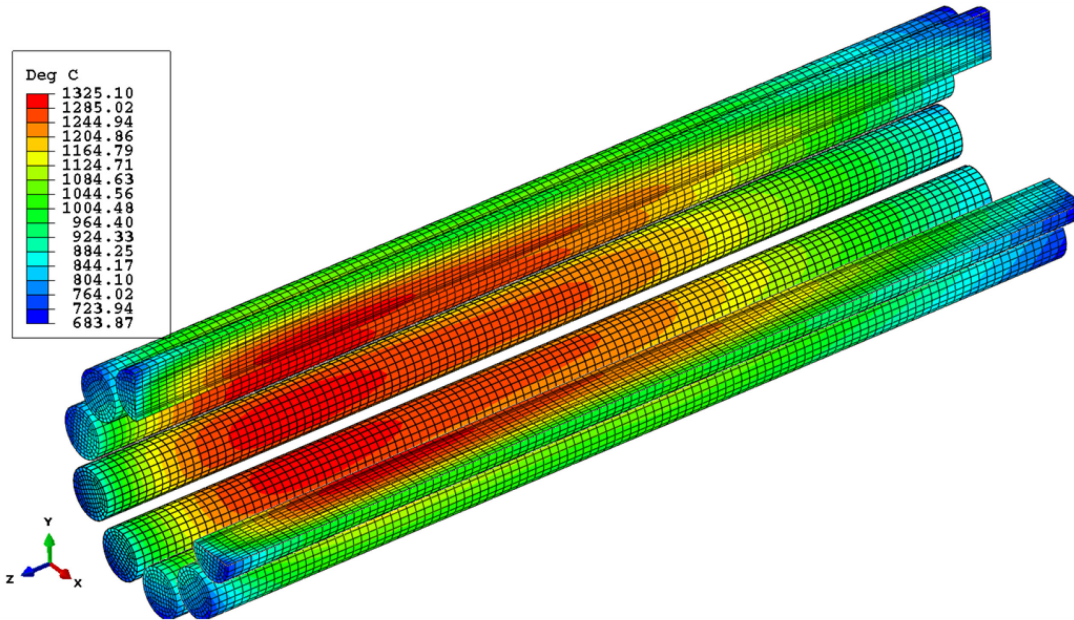


Figure 23. Temperature contour plot cutaway view of Capsule 1 fuel during Cycle 162B, day 20.

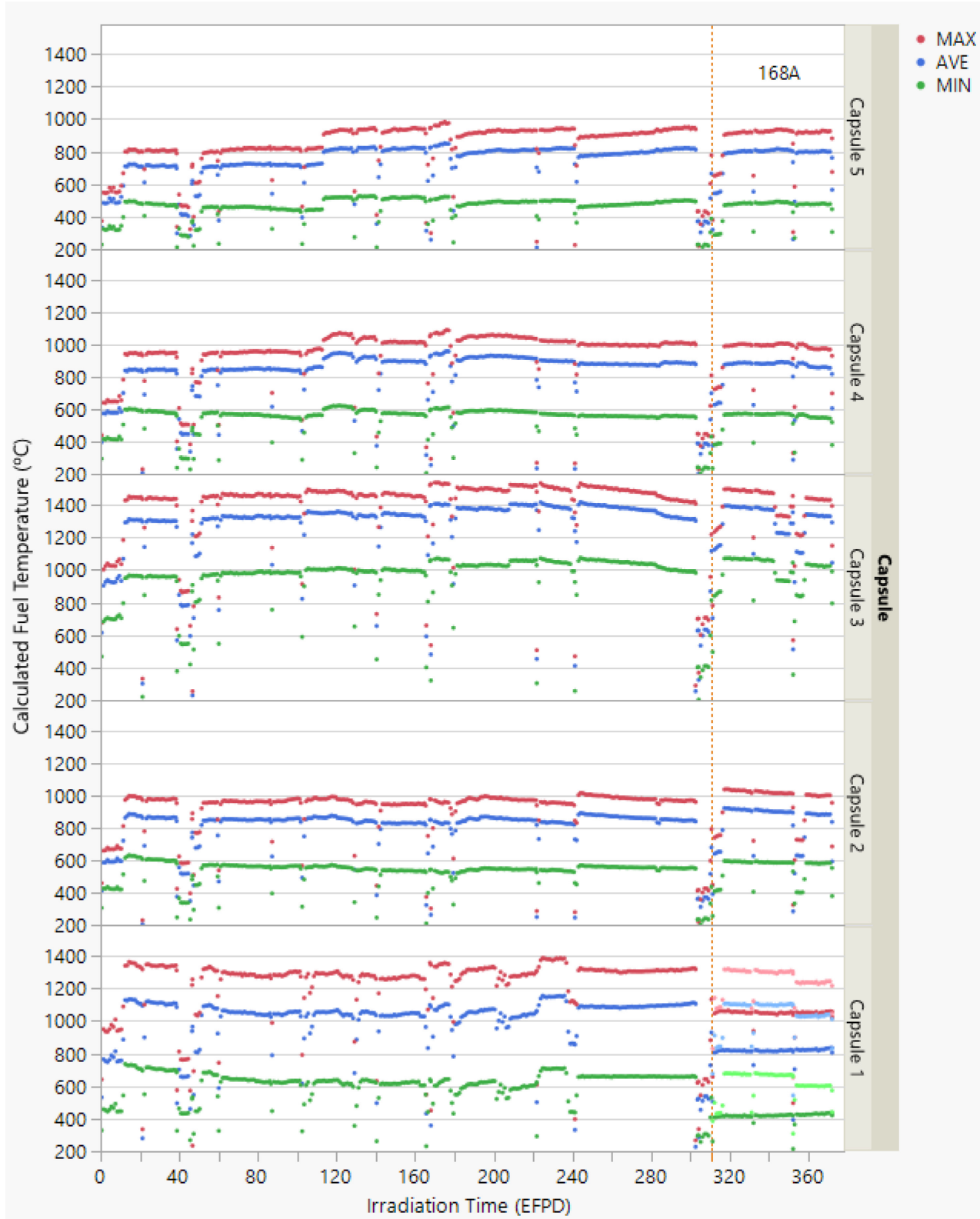


Figure 24. Daily minimum, maximum, and volume-averaged fuel temperatures (the light-colored dots for Capsule 1 are for the assumed leadout neon fraction [instead of zero]).

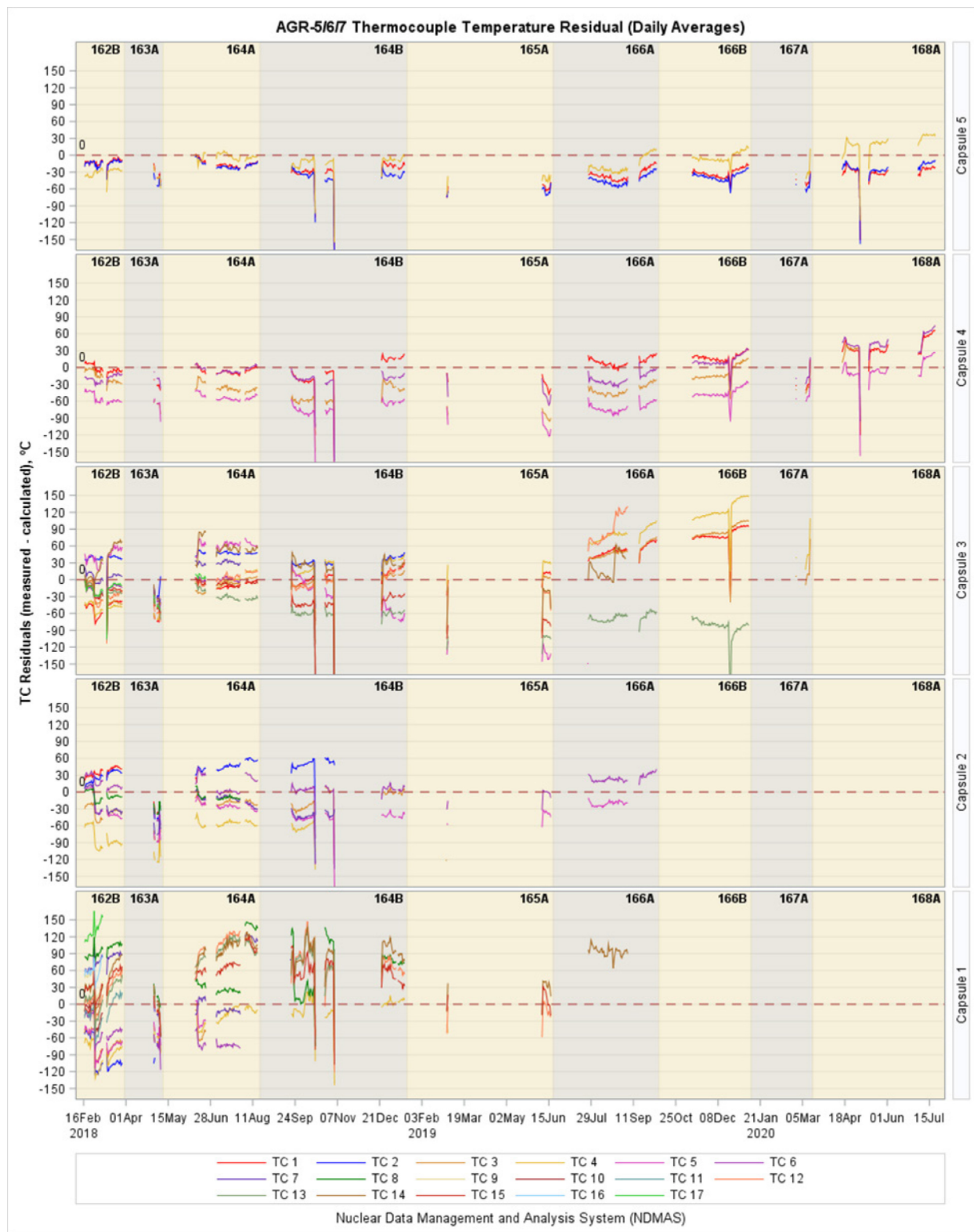


Figure 25. Difference between the measured and the calculated thermocouple temperatures for each capsule.

## 4. CAPSULE OFFSET EXAMINATION

The original model assumed that the gas gaps between the graphite holder and capsule wall were radially uniform, but the shorter nubs of AGR-5/6/7 holders led to a radial clearance of as much as 0.127 mm (or 0.005 in.) between the outside of the nubs and the capsule wall (nub-to-shell clearance) in all capsules. This clearance left the holder with room to shift inside the capsule shell, resulting in a non-uniform gas gap. This occurrence seemed to be more likely for Capsule 1, as the absence of through tubes in graphite holder would have allowed shifting of the Capsule 1 holder. However, the clearances of through tubes in the remaining four capsules are larger than the nub-to-shell clearance, which does not completely prevent them from shifting.

The basis of this analysis is that the most likely holder shift should lead to the best match between the measured and calculated temperatures from all operating TC locations in a capsule (with minimum temperature residuals from all TC locations). The steps in examining the offset are as follows:

1. Select possible options of the offset as combinations of the distances of both the top and /bottom of the holder center from the capsule centerline (e. g., 0.001, 0.002, 0.003, 0.0035, 0.004, 0.006, 0.0068 in.) and the top and bottom offset directions (i.e., E, NE, N, NW, W, SW, S, SE).
2. Find the best-fit offset combination, when the RMSE of the TC residuals (measured minus thermal simulated TC temperatures) from all the TCs in a capsule is smallest.
3. Investigate whether this best-fit offset option is constant over time by repeating Step 1 and Step 2 for several time steps over the AGR-5/6/7 irradiation.
4. Estimate capsule ultimate peak fuel temperature assuming maximum holder offset, when all TCs in a capsule failed during later cycles.

### 4.1 Thermal Model with Offset Holder

#### 4.1.1 Offset Model Description

This section describes an offset calculation in which the gas gap varies both in distance and direction. With the ABAQUS CAE model, it is possible to move the holder and contents inside the capsule; although, doing so is not prudent because it would require creating dozens of CAE models, which would be excessively time consuming. Therefore, this offset model is included in the gap conductance subroutine. For each offset geometry evaluated in the model, an offset in the +/-x and +/-y directions is determined for the top and bottom elevation of the holder. Figure 26 shows a diagram of the outside (capsule) offset  $h$  units in the  $x$  direction (east-west) and  $k$  units in the  $y$  direction (north-south) from the graphite holder. For a given  $x_i$  and  $y_i$  location of the holder surface (given in the gap conductance subroutine), the  $x_o$  and  $y_o$  coordinates of the corresponding capsule shell location are calculated, enabling the actual gap distance of the shifted capsule to be determined via Equation 10. Even though the finite element mesh model shows the capsule perfectly centered, this new gap is used for the gap conduction equations to account for the actual holder shift. The gap distances along the length of the holder are linearly interpolated along the axis between the calculated top and bottom elevation gap distances.

$$\begin{aligned}
 &\text{start with } y = \left(\frac{y_i}{x_i}\right) \cdot x_o, \text{ and } (x_o - h)^2 + (y_o - k)^2 = r_o^2, \text{ solve for } x_o \\
 &a = \left(\frac{y_i}{x_i}\right)^2 + 1, \quad b = -2 \left[\left(\frac{y_i}{x_i}\right) \cdot k + h\right], \quad c = k^2 + h^2 - r_o^2 \\
 &x_o = \frac{-b \pm \sqrt{b^2 - 4ac}}{2a}, \quad y_o = \pm \sqrt{r_o^2 - (x_o - h)^2} + k \\
 &\text{gap} = \sqrt{(x_o - x_i)^2 + (y_o - y_i)^2}
 \end{aligned} \tag{10}$$



Equation 11 shows the formula for determining the RMSE of TC residuals (measured-minus-calculated TC temperatures) from all operational TCs in each capsule. This RMSE was calculated for each offset option and was used to assess the goodness of fit between the measured and predicted TC temperatures for each offset option. The offset is considered most favorable when the RMSE is lowest.

$$RMSE = \sqrt{\frac{\sum_{i=1}^n (T_{measured} - T_{calculated})^2}{n}} \quad (11)$$

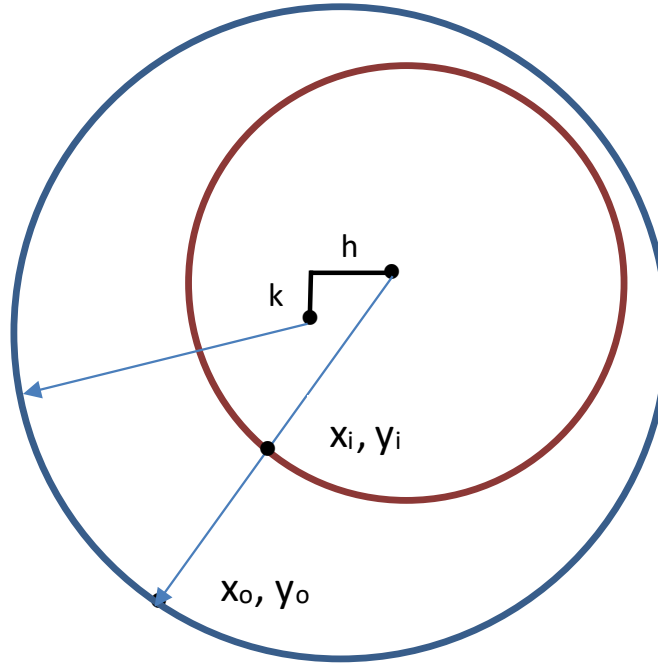


Figure 26. Gap calculation diagram, with capsule wall (blue circle) offset  $h$  units ( $x$  direction) and  $k$  units ( $y$  direction).

Figure 27 shows temperature contour plots from the original thermal analysis report at Day 41 (of 42) of Cycle 162B, with a cross-section view of Capsule 1 1.5 in. below the top of the graphite holder. The base case that has the graphite holder perfectly centered is shown in the center of the figure. The gas gap for this centered case at this elevation is 0.006 in. The temperatures are slightly hotter on the southwest side since it is closest to the ATR core center (see Figure 1) and experiences a slightly higher neutrons flux. The top figure (north) has had the gap increased by 0.001 in. on the north side and thus shows hotter temperatures because the gas gap is larger and exhibits less heat transport. All calculations were performed with a 0.001 in. vertically uniform offset. Rotating around the figure shows that the hottest temperatures are on the side where the gas gap is largest.

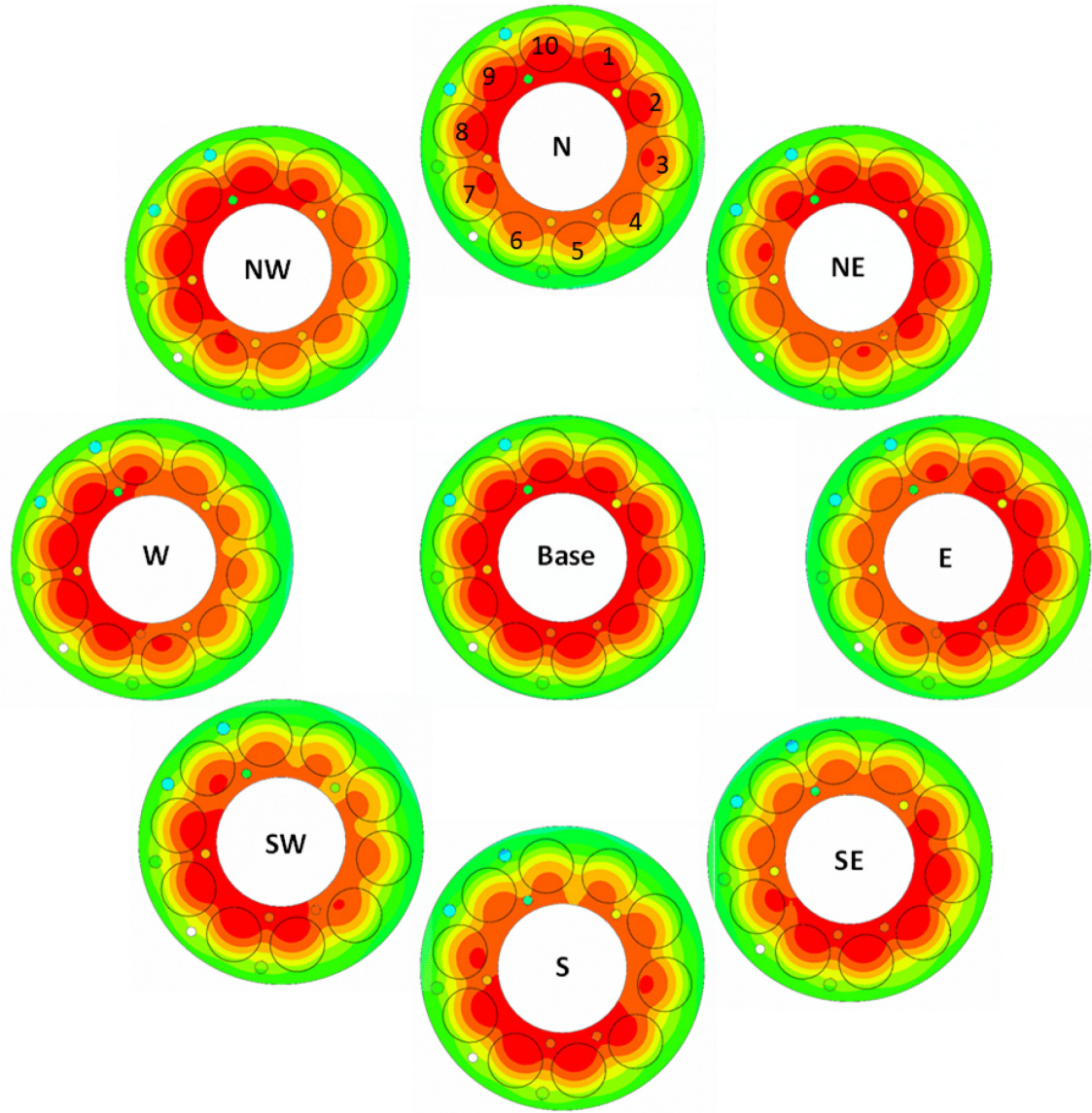


Figure 27. Temperature contour plots showing a cut section in Capsule 1 at 1.5 in. from the top of graphite holder varying by offset in eight directions, as taken on the second-to-last day of the first ATR irradiation cycle, Cycle 162B (Hawkes 2021). The circles with numbers are the 10 fuel stacks.

#### 4.1.2 Runs for Offset Examination

An offset position is represented by four parameters: the distance and direction of the offset at the top and bottom of the holder. There are 64 combinations of directions when using the selected eight directions of the top and bottom offset (E, NE, N, NW, W, SW, S, and SE) and a zero shift (center), as shown in Table 2. A  $4 \times 4$  matrix of computer runs comprising four top distances, and four bottom distances, for a total of 16 distance combination runs were performed. Within each computer run of this  $4 \times 4$  matrix, 64 different combinations of directions were simulated. The offset is defined as the holder remaining centered and the capsule wall moving in a distance and direction at the top and bottom of the holder. Due to graphite shrinkage over the course of irradiation, the holder clearance increased, making the available offset distances larger for the later dates.

Table 2. Sixty-five combinations of the top and bottom offset directions per computer run.

Step	Top Direction	Bottom Direction
1	Center	Center
2–9	E	E, NE, N, NW, W, SW, S, SE
10–17	NE	E, NE, N, NW, W, SW, S, SE
18–25	N	E, NE, N, NW, W, SW, S, SE
26–33	NW	E, NE, N, NW, W, SW, S, SE
34–41	W	E, NE, N, NW, W, SW, S, SE
42–49	SW	E, NE, N, NW, W, SW, S, SE
50–57	S	E, NE, N, NW, W, SW, S, SE
58–65	SE	E, NE, N, NW, W, SW, S, SE

For a selected time-step, the thermal model was executed for a total of 1,040 ( $65 \times 16$ ) offset positions. For each thermal model run, TC residuals (measured-minus-calculated TC temperature, as shown in Figure 32) and summary statistics (average and RMSE, as shown in Figure 33) were calculated from all operational TCs. The best-fit offset position corresponds to the smallest TC residual RMSE (representing both model bias and the standard deviation of the TC residuals). For example, Table 4 shows the best-fit offset option of the Capsule 1 holder calculated for March 3, 2018 (162B). The distance t1b1 in the first cell represents that the capsule top shifted by 0.001 in. from the top center and that the capsule bottom shifted 0.001 in. from the bottom center (referred to as “offset” for the rest of this report). For each distance offset, the combination of directions (i.e., tNWbNW means the offset at the top of the holder was in the northwest direction and the offset at the bottom of the holder was in the northwest direction) represents the best-fit direction offset per each distance offset, which resulted in the minimum TC RMSE (last number in each cell in Table 4, for example).

For detailed temperature results for each compact for each date, see Table 15 in Appendix A, “Capsule 1 Compact Temperature for Zero and Best-fit Offset Calculated for Selected Dates” and Table 16 in Appendix B, “Capsule 2 Compact Temperature for Zero and Best-fit Offset Calculated for Selected Dates.”

## 4.2 Capsule 1 Offset Holder Analysis

Capsule 1 was at the bottom of the AGR-5/6/7 test train. Figure 28 shows the 17 TCs located throughout the Capsule 1 graphite holder. These terminate at different depths, as shown in Table 3. All of them were operational during the first ATR cycle (i.e., Cycle 162B). However, only seven TCs survived to the end of the third ATR Cycle 164A, and the last TC failed in the middle of Cycle 166A (Pham 2021). Table 3 also shows the type of each TC, along with the cycle during which each TC failed (see Pham et al. 2021 for further information on TC types).

Table 3. Depth of TC tip in the holder, type or material, and failure cycle for the 17 TCs in Capsule 1.

TC Number	Penetration, in.	Type or material	Failure during cycle
TC-1-1	2.4	CAMB-N	162B
TC-1-2	2.4	SPINEL-N	163A
TC-1-3	2.4	CAMB-N	164A
TC-1-4	2.4	CAMB-N	165A
TC-1-5	4.4	CAMB-N	164A
TC-1-6	6.4	CAMB-N	164A



TC Number	Penetration, in.	Type or material	Failure during cycle
TC-1-7	8.4	CAMB-N	164B
TC-1-8	8.4	CAMB-N	164B
TC-1-9	6.4	HTIR-TC	162B
TC-1-10	2.4	HTIR-TC	162B
TC-1-11	2.4	HTIR-TC	162B
TC-1-12	4.4	HTIR-TC	165A
TC-1-13	4.4	HTIR-TC	164B
TC-1-14 – last to fail	2.4	HTIR-TC	166A (middle)
TC-1-15	6.4	HTIR-TC	166A
TC-1-16	2.4	HTIR-TC	162B
TC-1-17	8.4	HTIR-TC	162B

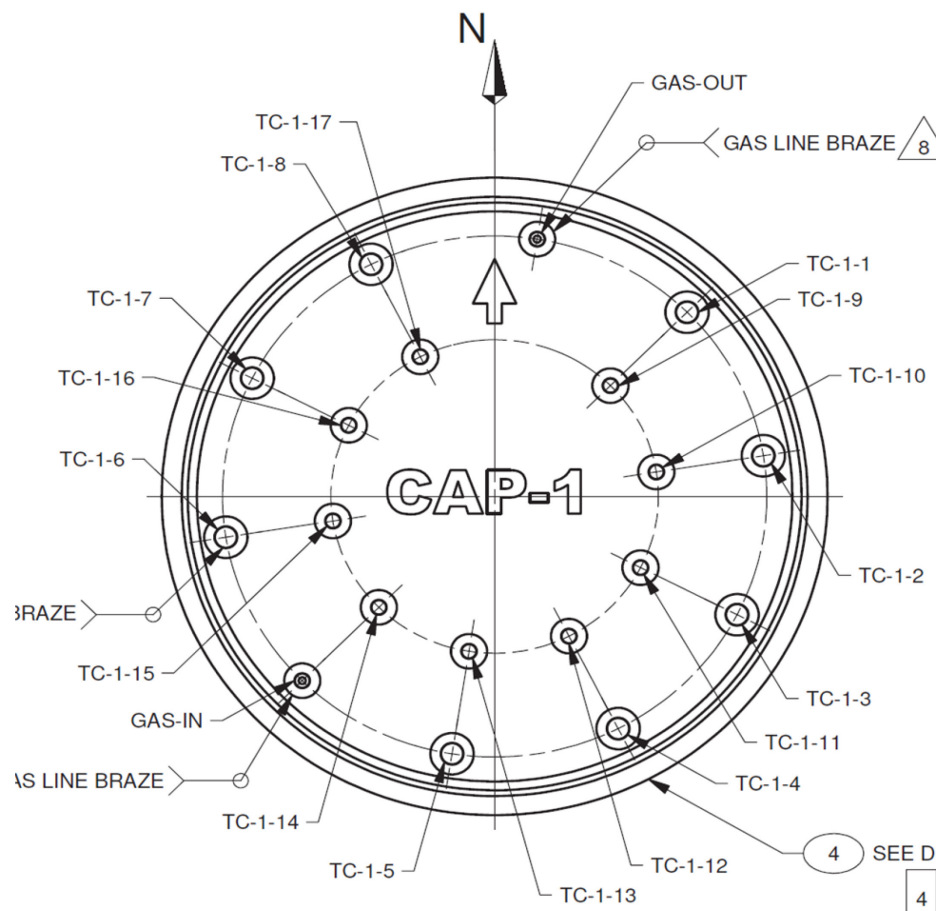


Figure 28. Cross section showing the 17 thermocouples embedded throughout the Capsule 1 graphite holder.

For Capsule 1, four time-steps over the AGR-5/6/7 irradiation were selected: March 3, 2018 (Cycle-1 162B); July 15, 2018 (Cycle 3 164A); August 12, 2008 (Cycle 3 164A); September 20, 2019 (Cycle 6 166A). The reasoning behind these selected dates are as follows:

- March 3, 2018 (162B): This was near the beginning of irradiation and the temperatures had been raised to the target range. All 17 TCs were still fresh (with minimal drift) and operational, allowing for the best offset optimization.
- July 15, 2018 (164A): This date was selected in order to investigate whether the offset was stable over time, even though only eight of the 17 TCs were still operational (Figure 29).
- August 12, 2018 (164A): This date was selected in order to investigate whether the offset caused a significant increase in TC residuals for several TCs, as shown in Figure 29. For example, the residual for TC-7 jumped from  $\sim -10^{\circ}\text{C}$  to  $120^{\circ}\text{C}$  and residual for TC-8 jumped from  $\sim 30^{\circ}\text{C}$  to  $\sim 140^{\circ}\text{C}$  (an increase of more than  $100^{\circ}\text{C}$ ).
- September 20, 2019 (166A): All TCs in Capsule 1 failed, so the offset was chosen based on the results from the above three dates in order to investigate the peak capsule temperatures at this time that immediately preceded the start of massive particle failures near the end of this cycle (Pham et al, 2021).

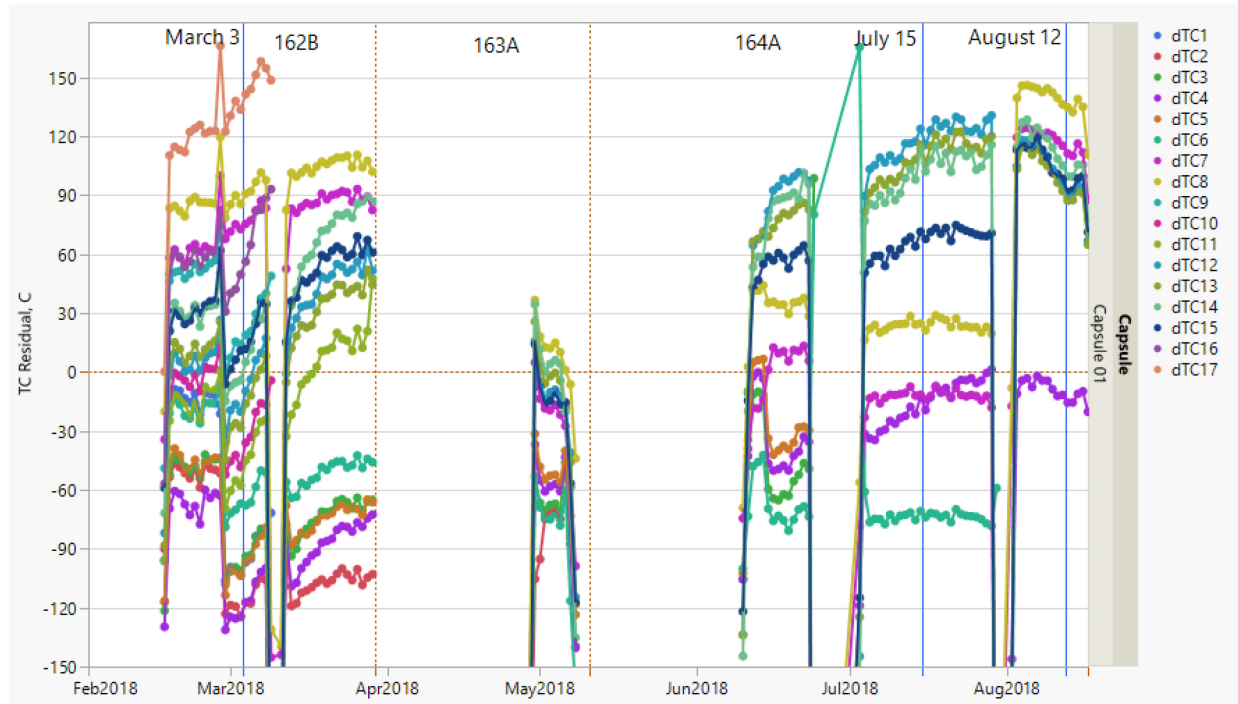


Figure 29. Capsule 1 thermocouple residuals during the first three cycles, showing the first three selected dates (blue vertical lines).

Figure 30 shows a cut-away view of the HGRs for the fuel compacts in Capsule 1 for the four dates mentioned above. These values were imported from the neutronics analysis (Sterbentz 2020). Note that the HGRs for Sep 20, 2019, are lower, as the fuel had been partially depleted. Figure 31 shows the cumulative fast neutron fluence for the four dates chosen. This has a direct impact on the thermal conductivity of the graphite holder and gap width, due to the holder shrinkage. Thus, the HGR and fast neutron fluence are important inputs that affect the calculated temperatures.

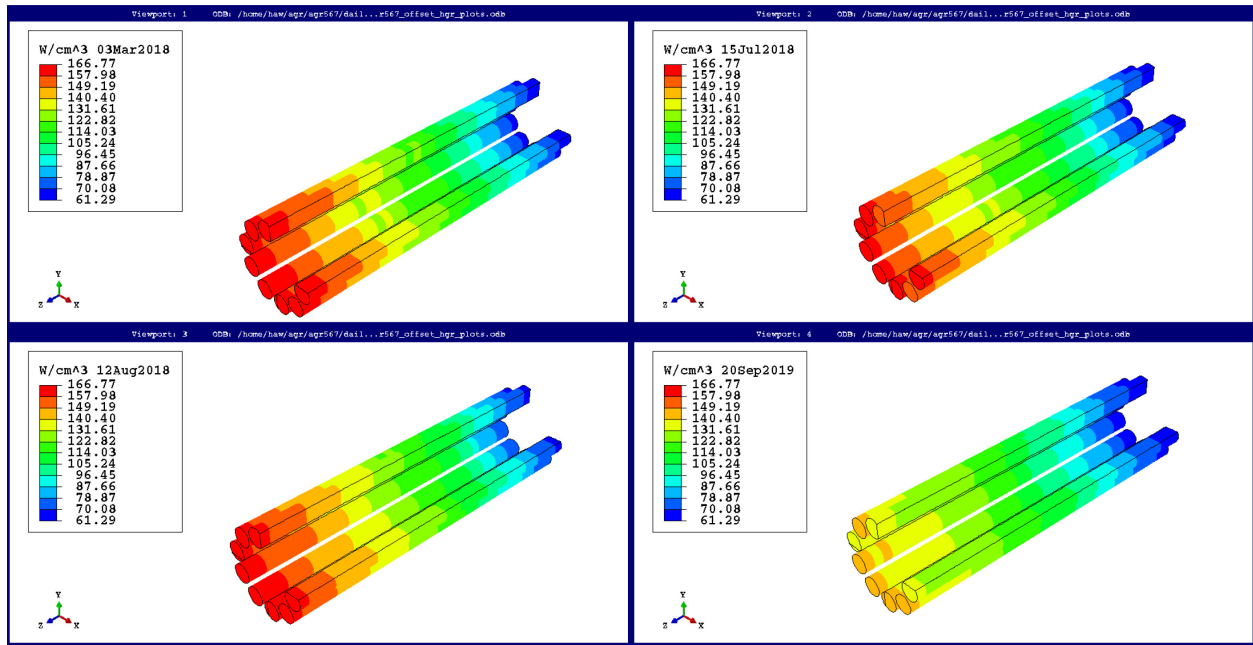


Figure 30. Cutaway view of heat generation rate ( $W/cm^3$ ) for the Capsule 1 fuel for March 3, 2018 (top left); July 15, 2018 (top right); August 12, 2018 (bottom left); and September 20, 2019 (bottom right).

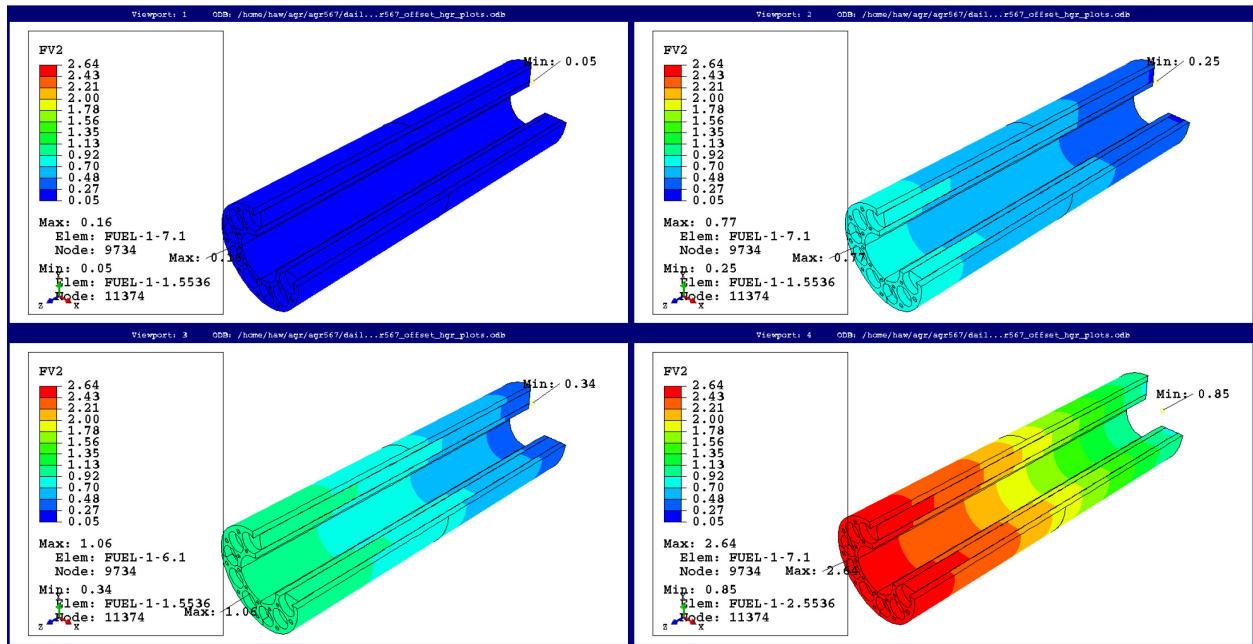


Figure 31. Fast neutron fluence ( $1.0 \times 10^{25}$  neutrons/ $m^2$  ( $E_n > 0.18$  MeV)) for the Capsule 1 holder for March 3, 2018 (top left); July 15, 2018 (top right); August 12, 2018 (bottom left); and September 20, 2019 (bottom right).

#### 4.2.1 March 3, 2018, ATR Cycle 162B

Table 4 shows the best-fit directions that resulted in the minimum RMSE for each pair of 16 offset distances calculated for March 3, 2018 (162B). For each cell in Table 4, the distance t1b1 represents that the capsule top shifted by 0.001 in. from the top center and that the capsule bottom shifted 0.001 in. from

the bottom center (referred to as “offset” for the rest of this report). For each distance offset, the combination of directions in Table 4 represents the best direction offset, which resulted in the minimum RMSE (last number in each cell in Table 4) for each distance offset.

The top offset of 0.002 in. to the west and the bottom offset of 0.0035 in. to the north (orange cell) resulted in the minimum residual RMSE from 17 operational TCs (minimum RMSE value of 44.4 °C versus 77.9°C for centered (zero offset) holder). Other offset options also yielded very close TC residual RMSEs to the best fit.

The TC residuals (Figure 32) and the average and RMSE values (Figure 33) as a function of the 65 azimuthal positions, clearly indicate that the best-fit offset position (t2b35) resulted in the smallest spread of TC residuals, as they are scattered tightly around the zero horizontal line (only ~3°C average). This indicates a well-balanced thermal model with minimal bias. The TC residual plots for the zero and best-fit offsets (Figure 34) also show a significant reduction in residuals for most of the 17 operational TCs in Capsule 1. Figure 35 shows a temperature contour plot for a 0.25 in. axial slice in which the highest temperature occurs for the best-fit offset. The maximum temperature of 1416°C occurs in stack 9, compact level 7 in the northwest direction.

Table 4. Best-fit options for each of the 16 offset distances, best-fit direction, and minimum RMSE for March 3, 2018 (162B). The best-fit option is shaded orange.

March 3, 2018 (162B)—all 17 TCs remained: Distances / Directions / Minimum RMSE (°C)			
t1b1 / tNWbNW / 59.0	t1b2 / tWbNW / 54.1	t1b3 / tWbNW / 50.8	t1b35 / tWbNW / 50.1
t2b1 / tNWbNW / 53.6	t2b2 / tWbN / 47.9	t2b3 / tWbN / 44.7	t2b35 / tWbN / 44.4
t3b1 / tWbN / 55.3	t3b2 / tWbN / 49.9	t3b3 / tWbN / 47.1	t3b35 / tWbN / 46.8
t35b1 / tNWbN / 59.0	t35b2 / tWbN / 54.4	t35b3 / tWbN / 52.0	t35b35 / tWbN / 51.8

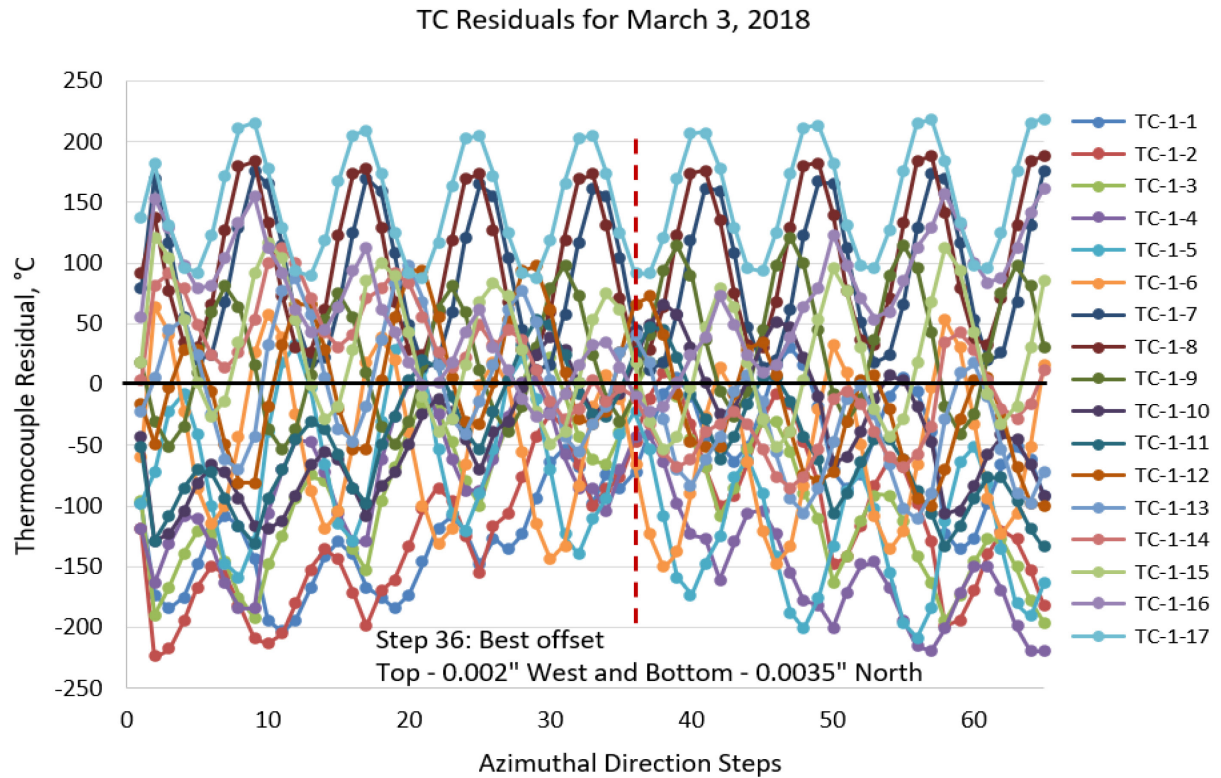


Figure 32. Residuals of 17 TCs as a function of offset direction (Table 2) for the best-fit offset, showing the smallest variation of TC residuals to be at Step 36 for March 3, 2018 (Cycle 162B).

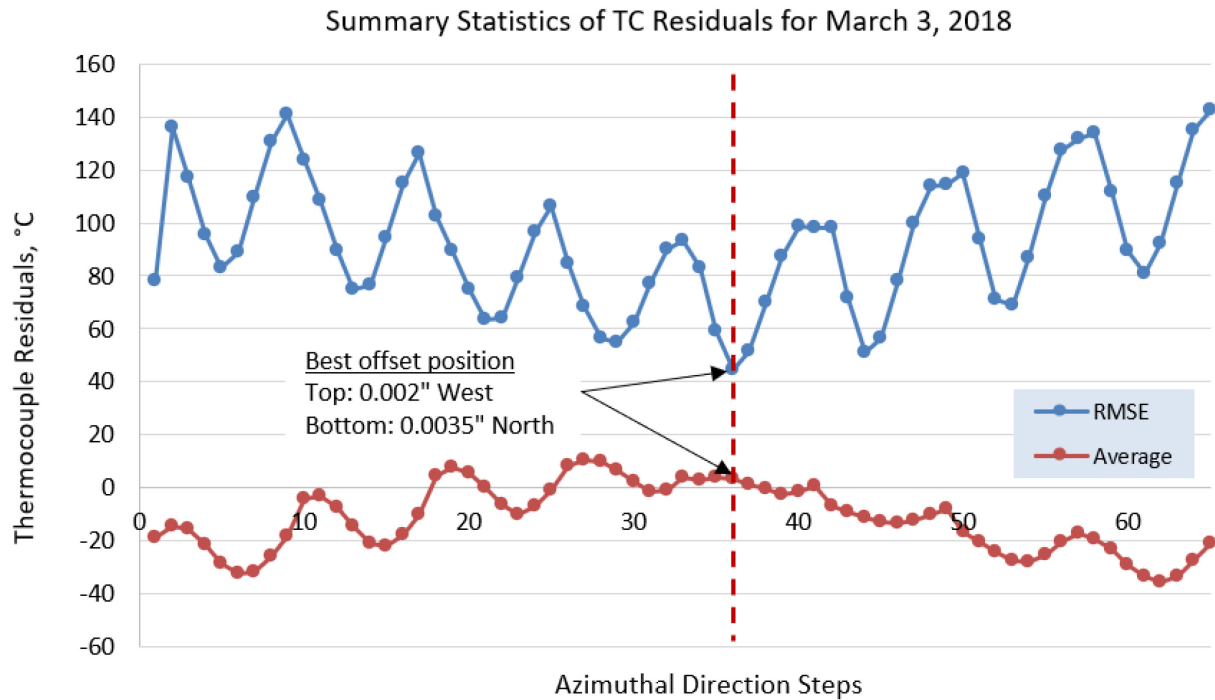


Figure 33. Average and RMSE residuals from the 17 TCs as a function of offset direction step (Table 2), showing the best offset position to be at Step 36 for March 3, 2018 (Cycle 162B).



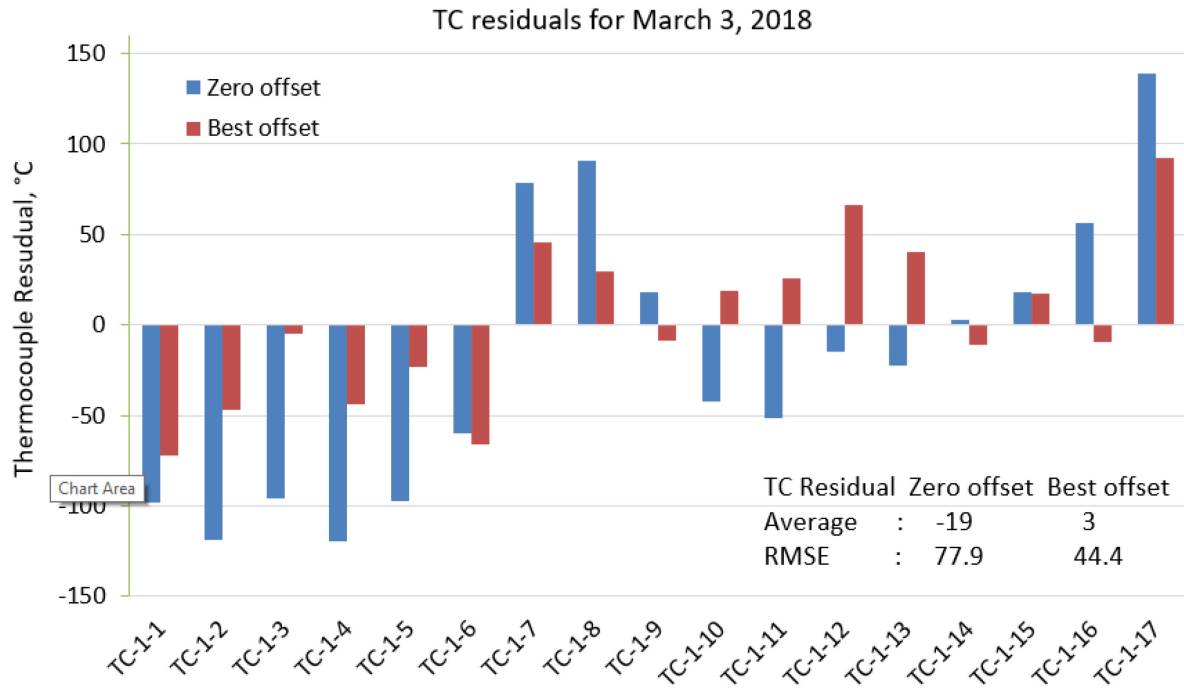


Figure 34. TC residuals of zero and best-fit offset for March 3, 2018 (Cycle 162B).

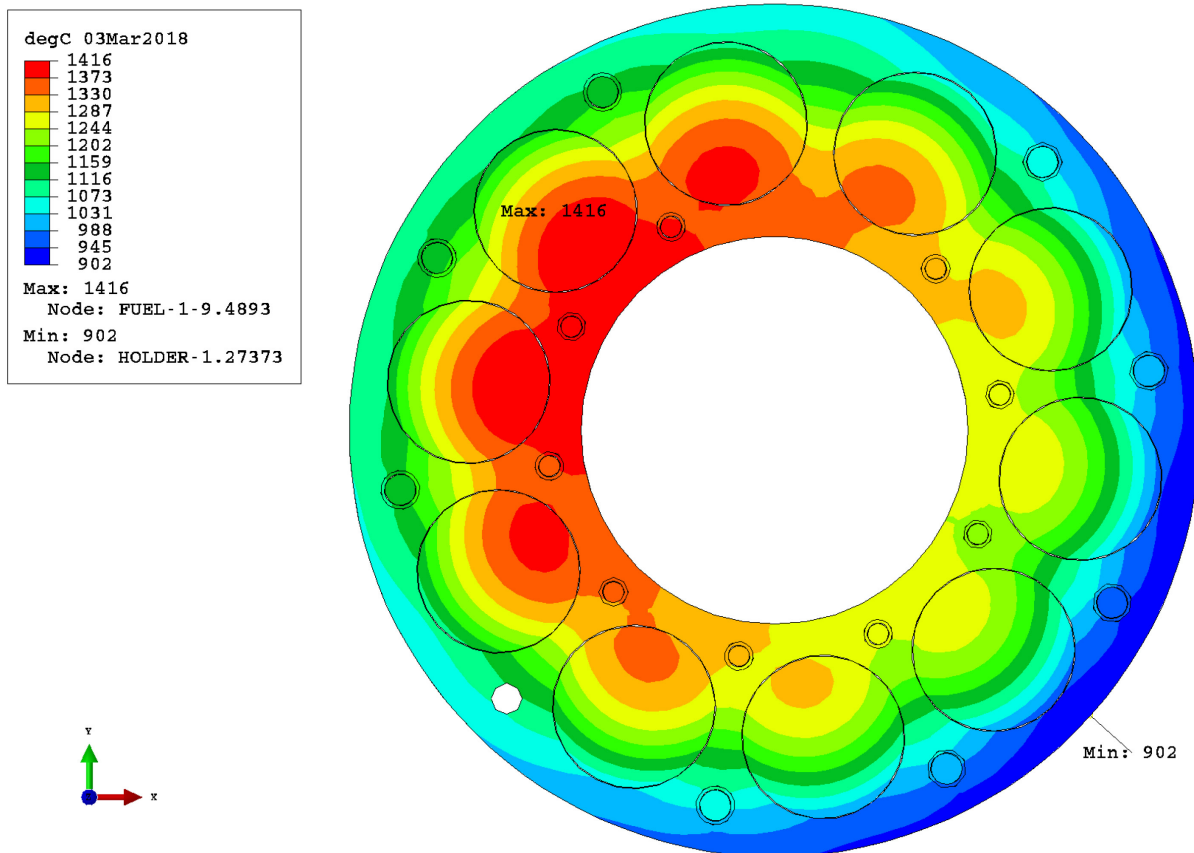


Figure 35. Temperature ( $^{\circ}\text{C}$ ) contour plot of the 0.25 in. slice (level 7) in which the highest temperature occurs for March 3, 2018, the best-fit offset position being 0.002 in. top west and 0.0035 in. bottom north.

#### 4.2.2 July 15, 2018, ATR Cycle 164A

Table 5 shows the best-fit directions that resulted in the minimum RMSE for each pair of offset distances calculated for July 15, 2018 (162B). As the irradiation progressed, the hot gap distance grew larger, which led to more offset distance options, relative to the original 4x4 matrix of offset distances examined for March 3. The additional eight runs were computed with finer resolution around the best-fit option to refine the best fit. The top offset of 0.003 in. to the west and the bottom of 0.003 in. to the southeast (orange cell) resulted in the minimum residual RMSE from the eight-remaining operational TCs. But other offsets also yielded a TC residual RMSE that was very close to the best-fit option.

The TC residuals (Figure 36) and the average and RMSE values (Figure 37) as a function of the 65 azimuthal positions clearly indicate that the best-fit offset position (t3b3) resulted in the smallest spread of TC residuals, but they are mostly positive (15.3°C average). The TC residual plots for the zero and best-fit offsets (Figure 38) also show less reduction in residuals for the eight operational TCs than the March 3 case. Figure 39 shows a temperature contour plot of a 0.25 in. axial slice in which the highest temperature occurs for the best-fit offset. The maximum temperature of 1376°C occurs in stack 7, compact level 8, toward the southwest section.

Table 5. Best-fit options for each of the 24 offset distances, best-fit direction, and minimum RMSE for July 15, 2018 (164A). The best-fit option is shaded orange.

July 15, 2018 (164A)—8 TCs remained: Distances / Directions / Minimum RMSE					
t15b15 tSWbSE/56.4	—	t15b3 tWbSE/56.0	—	t15b45 tNWbS/63.8	t15b55 t0b0/65.0
—	t2b2 tWbSE/54.8	t2b3 tWbSE/54.8	t2b35 tWbSE/56.5	—	—
t3b15 tSWbE/55.7	t3b2 tSWbE/54.7	t3b3 tWbSE/53.8	t3b35 tWbSE/54.9	t3b45 tWbSE/60.4	t3b55 t0b0/65.0
—	t35b2 tSWbE/55.1	t35b3 tWbSE/54.0	t35b35 tWbSE/54.6	—	—
t45b15 tSWbE/58.8	—	t45b3 tWbSE/55.5	—	t45b45 tWbE/58.0	t45b55 tSWbNE/61.2
t55b15 tSWbE/62.2	—	t55b3 tWbSE/58.5	—	t55b45 tSWbNE/57.9	t55b55 tSWbNE/59.5

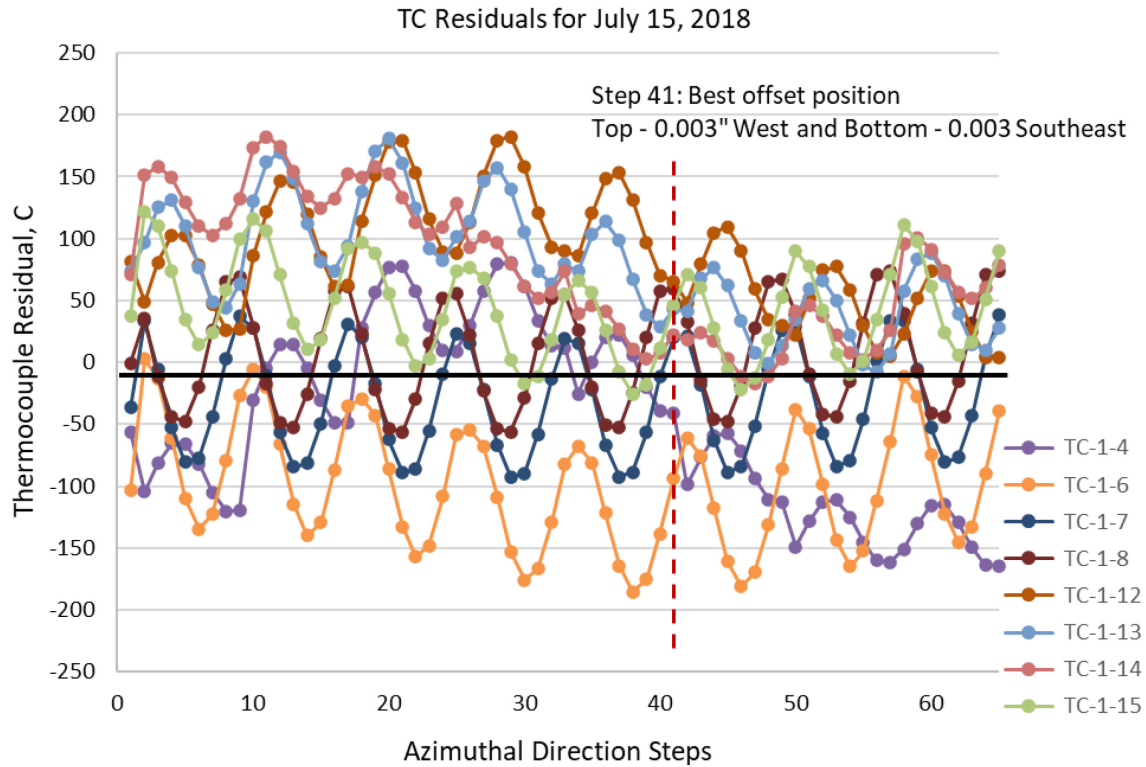


Figure 36. Residuals of the eight operational TCs as a function of offset direction (Table 2) for the best-fit offset, showing the smallest variation of TC residuals to be at Step 41 for July 15, 2018 (Cycle 164A).

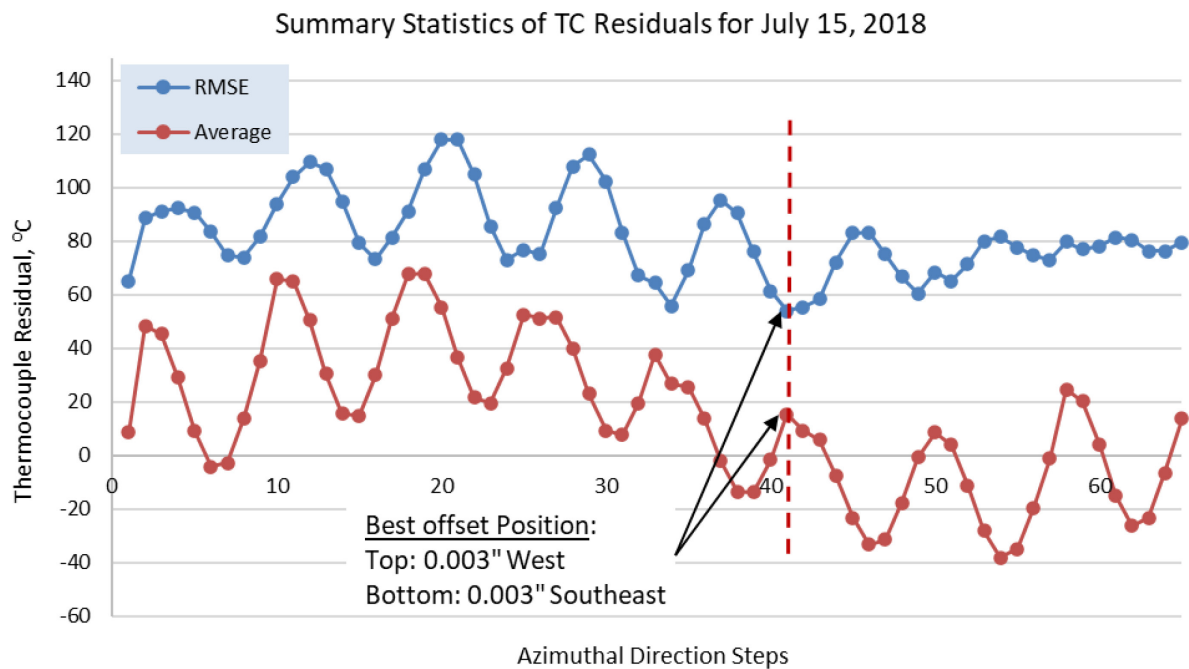


Figure 37. Average, RMSE, and standard deviation of TC residuals as a function of offset direction step (Table 2), showing the best offset position to be at Step 41 for July 15, 2018 (Cycle 164A).



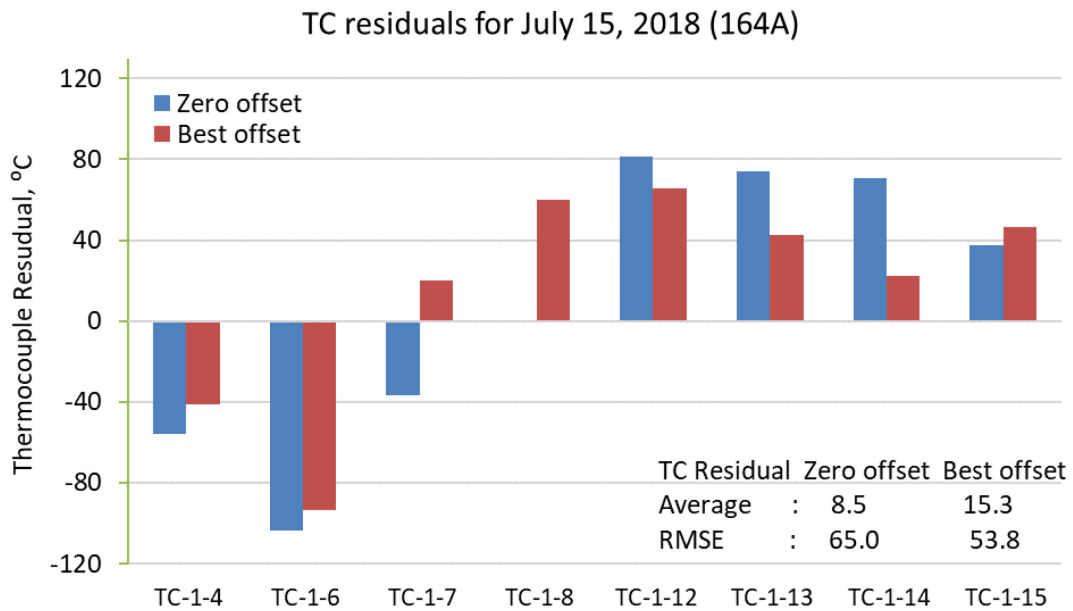


Figure 38. TC residuals of zero and best-fit offset for July 15, 2018 (Cycle 164A).

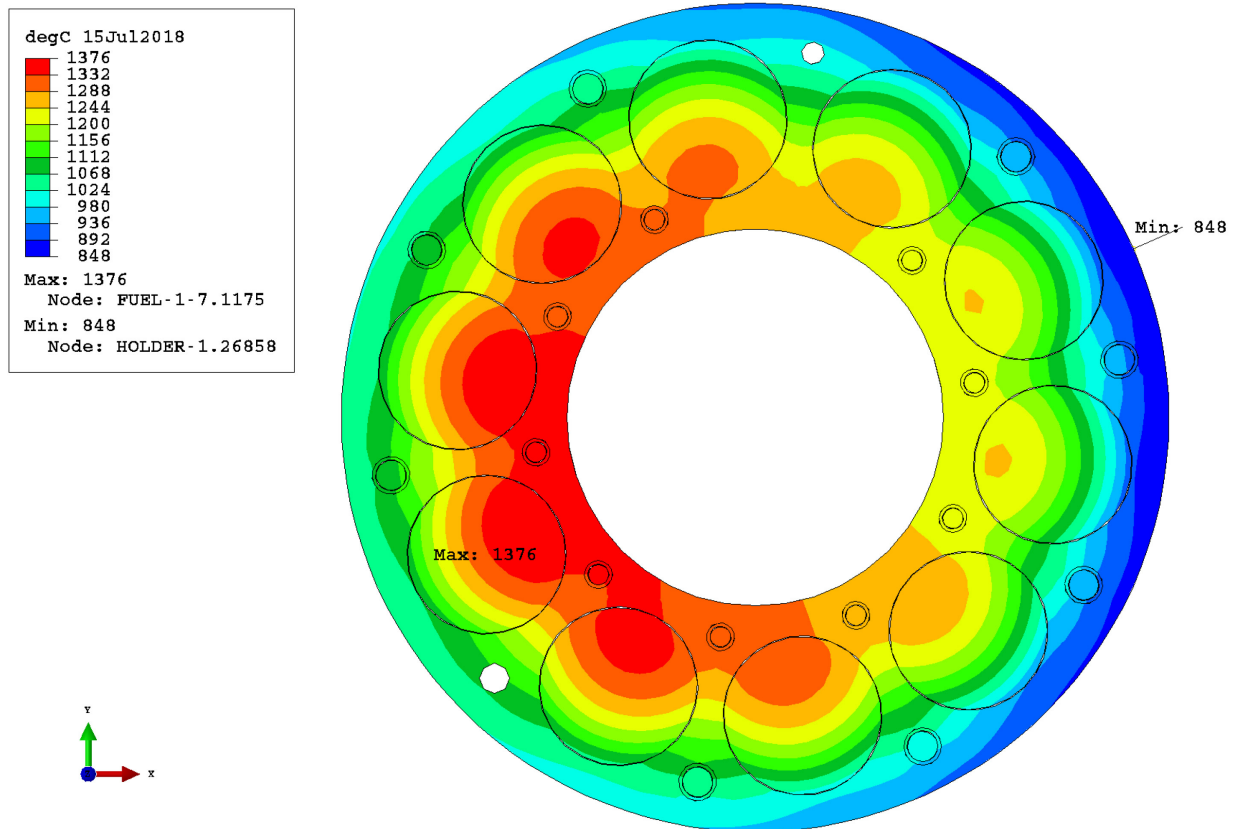


Figure 39. Temperature ( $^{\circ}\text{C}$ ) contour plot of the 0.25 in. slice (level 8) in which the highest temperature occurs for July 15, 2018, the best-fit offset position being 0.003 in. top west and 0.003 in. bottom southeast (Step 41).

### 4.2.3 August 12, 2018, ATR Cycle 164A

Table 6 shows the best-fit directions that resulted in the minimum RMSE for each pair of offset distances calculated for August 12, 2018 (162B). The top offset of 0.0035 in. to the southwest and the bottom offset of 0.0035 in. to the northwest (orange cell) resulted in the minimum residual RMSE from the seven remaining TCs. However, other offset options also yielded a TC residual RMSE that was very close.

The TC residuals (Figure 40) and the average and RMSE values (Figure 41) as a function of the 65 azimuthal positions, clearly indicated that the best-fit offset position (t35b35) resulted in the smallest spread of TC residuals, which were mostly positive (22.6°C average). The TC residual plots for the zero and best-fit offsets (Figure 42) also show substantial reduction in residuals for four out of the seven remaining TCs.

Table 6. Best-fit options for each of the 16 offset distances, best-fit direction, and minimum RMSE for August 12, 2018 (164A). The best-fit option is shaded orange.

August 12, 2018 (164A)—7 TCs remained: Distances / Directions / Minimum RMSE			
t2b2 / tSWbNW / 54.0	t2b3 / tSWbW / 51.3	t2b35 / tSWbW / 49.9	t2b45 / tSWbW / 48.6
t3b2 / tSWbNW / 52.5	t3b3 / tSWbNW / 49.0	t3b35 / tSWbNW / 48.4	t3b45 / tSWbNW / 49.6
t35b2 / tSWbNW / 52.4	t35b3 / tSWbNW / 48.7	<b>t35b35 / tSWbNW / 47.9</b>	t35b45 / tSWbNW / 48.7
t45b2 / tSWbNW / 53.7	T45b3 / tSWbNW / 49.3	t45b35 / tSWbNW / 48.3	t45b45 / tSWbNW / 48.4

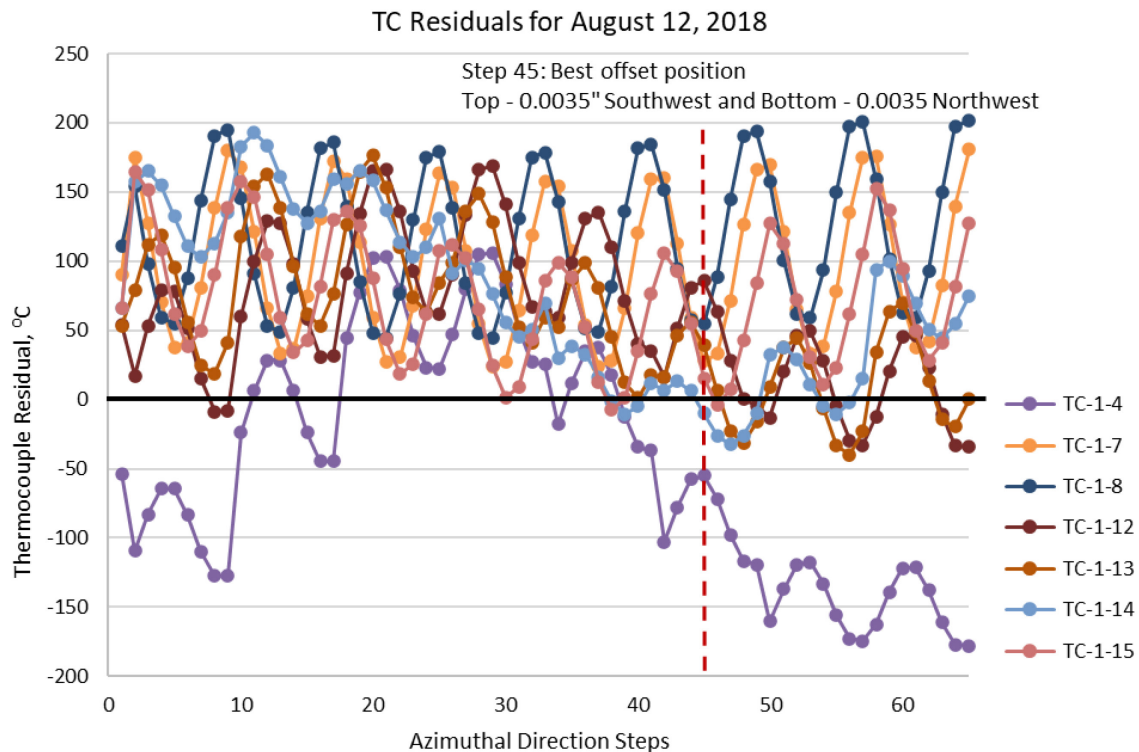


Figure 40. Residuals of the seven operational TCs as a function of offset direction (Table 2) for the best distances, showing the smallest variation of TC residuals to be at Step 45 for August 12, 2018 (Cycle 162B).

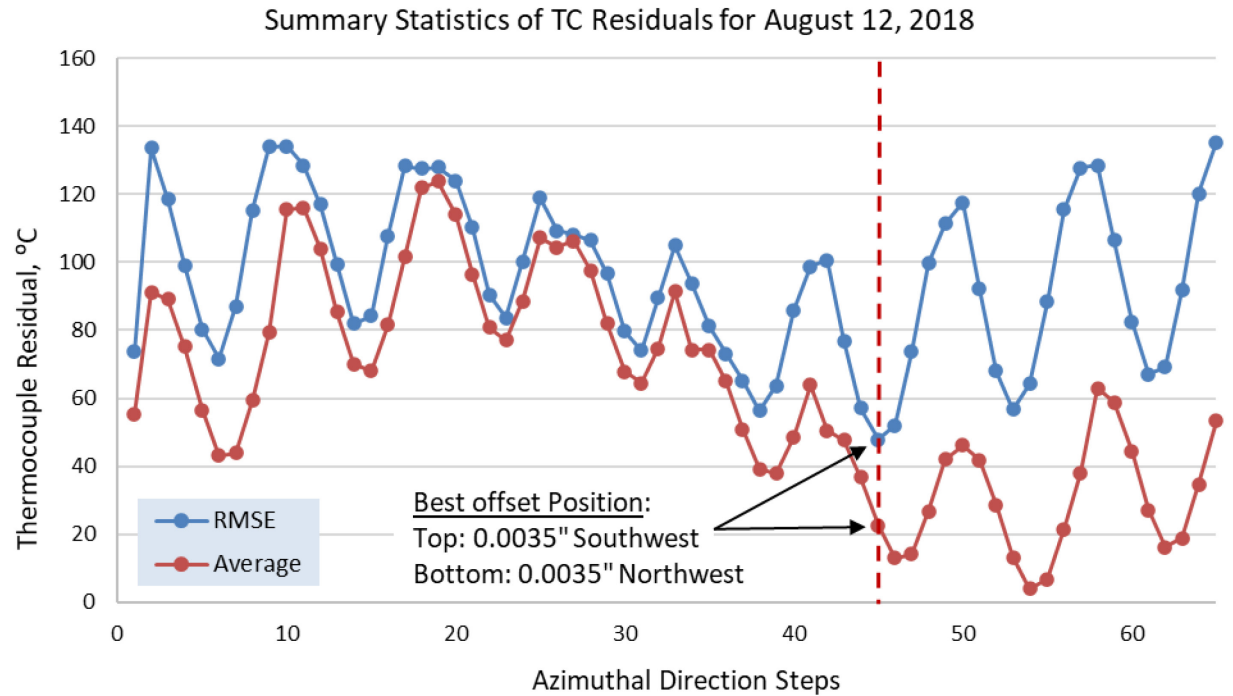


Figure 41. Average, RMSE, and standard deviation of the TC residuals as a function of offset direction step (Table 2), showing the best offset position to be at Step 45 for August 12, 2018 (Cycle 164A).

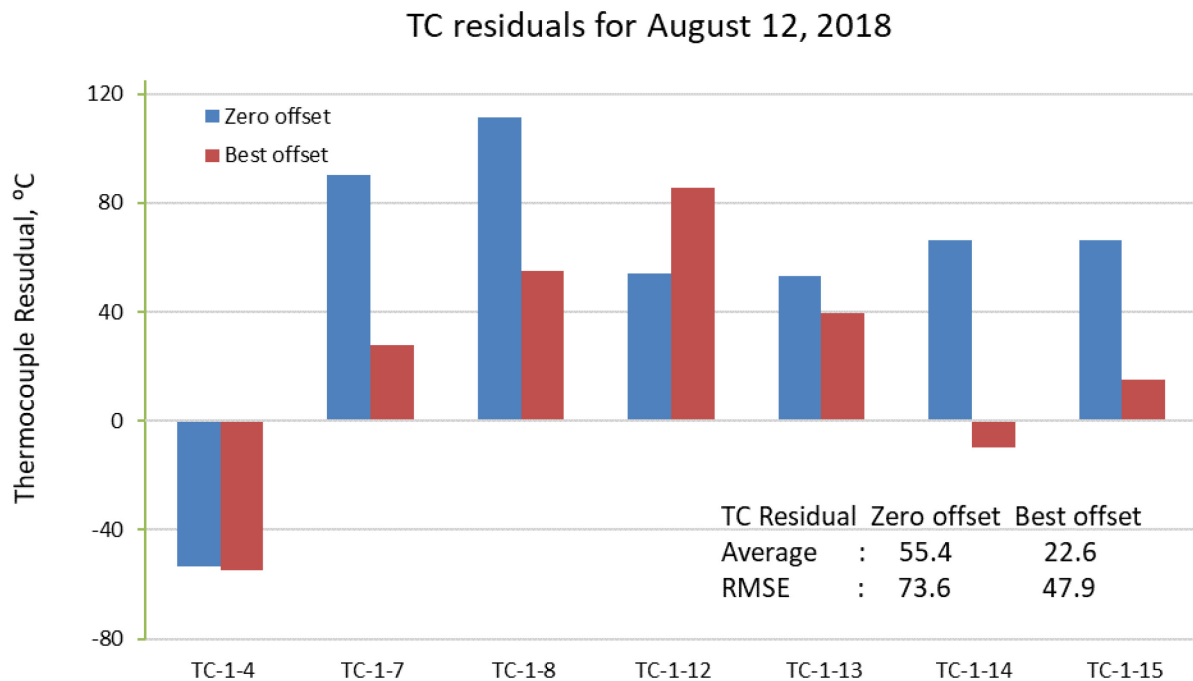


Figure 42. TC residuals of zero and best-fit offset for August 12, 2018 (Cycle 164A).

Figure 43 shows a temperature contour plot of a 0.25 in. axial slice in which the highest temperature occurring for the best-fit offset for Step 45 for August 12, 2018. The maximum temperature of 1420°C occurs in stack 7, compact level 8, toward the southwest section.

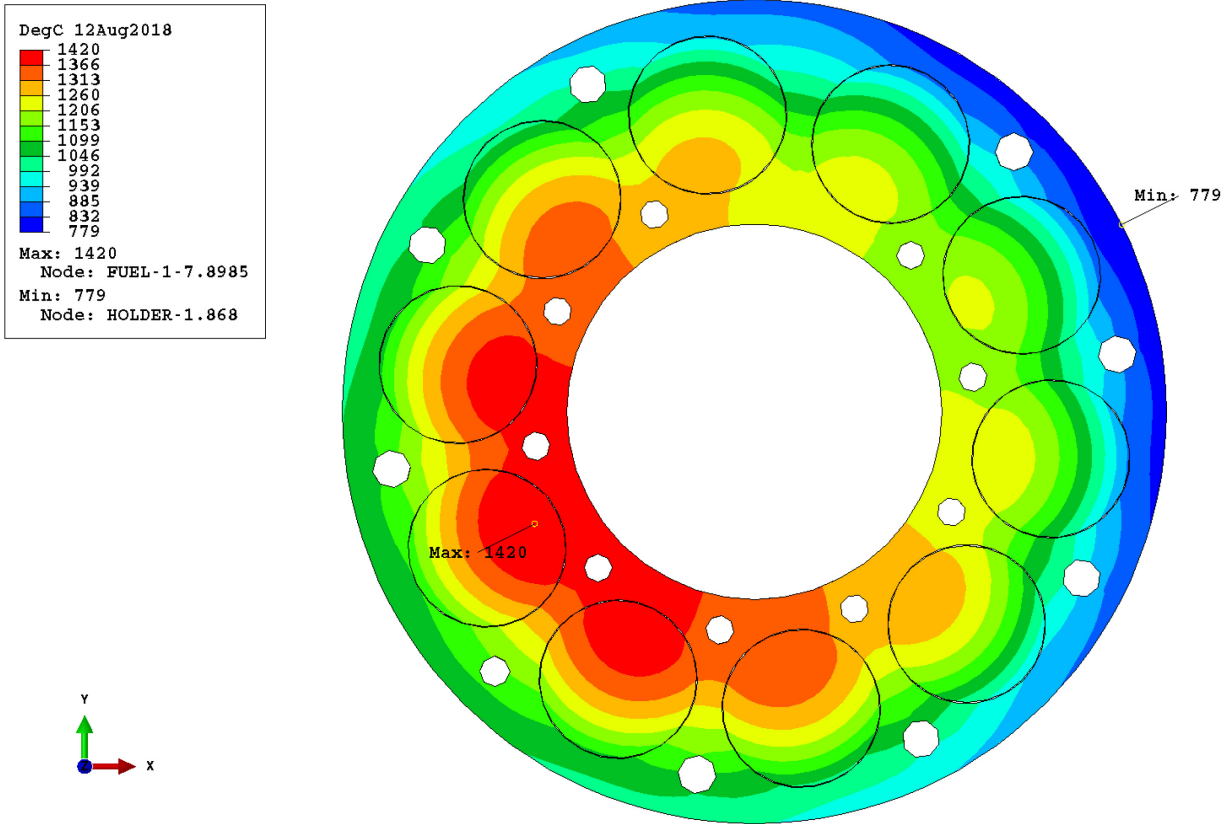


Figure 43. Temperature (°C) contour plot of the 0.25 in. slice (level 8) in which the highest temperature occurred for August 12, 2018, the best-fit offset position being 0.0035 in. top southwest and 0.0035 in. bottom northwest Step 45.

The behavior of the TC-1-4 residuals (purple line in Figure 40) is inconsistent with the other six remaining TCs, as it varied within a much wider range (-180 to 110 °C) and displayed a different pattern than did the other five TCs. As expected, the offset optimization excluding TC-1-4 yielded a minor different best-fit offset option, as the top offset moved from 0.0035 in. southwest to 0.0035 in. south and the bottom offset stayed at 0.0035 in. northwest (Figure 44 and Figure 45). However, TC-1-4 was determined to be functioning normally during this time (Pham 2021) despite the somewhat erratic behavior. Wider variation of TC-1-4 residuals could be contributed to its specific location, near the top and right next to the gap that make it more sensitive to the offset variation. Thus, TC-1-4 has been included in the final results.

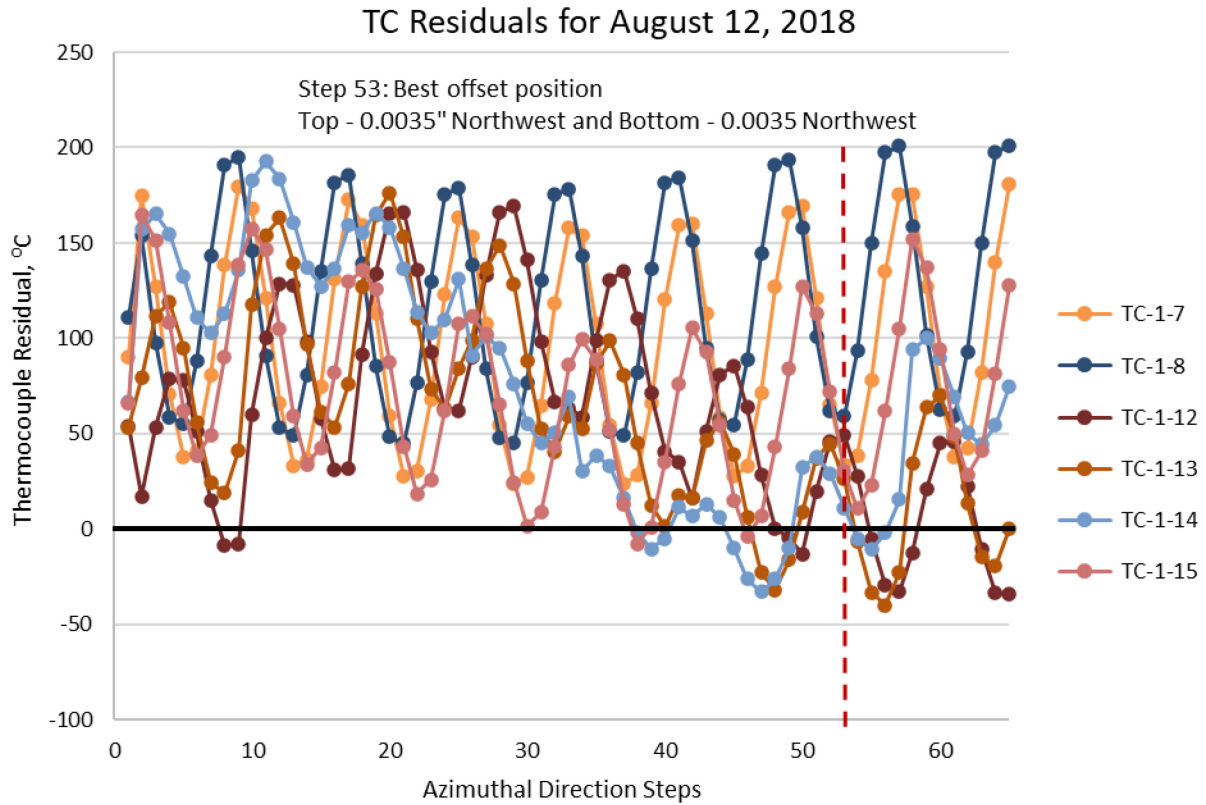


Figure 44. Residuals of the six operational TCs (TC-1-4 was excluded) as a function of offset direction (Table 2) for the best distances, showing the smallest variation of TC residuals at Step 53 for August 12, 2018 (Cycle 162B).

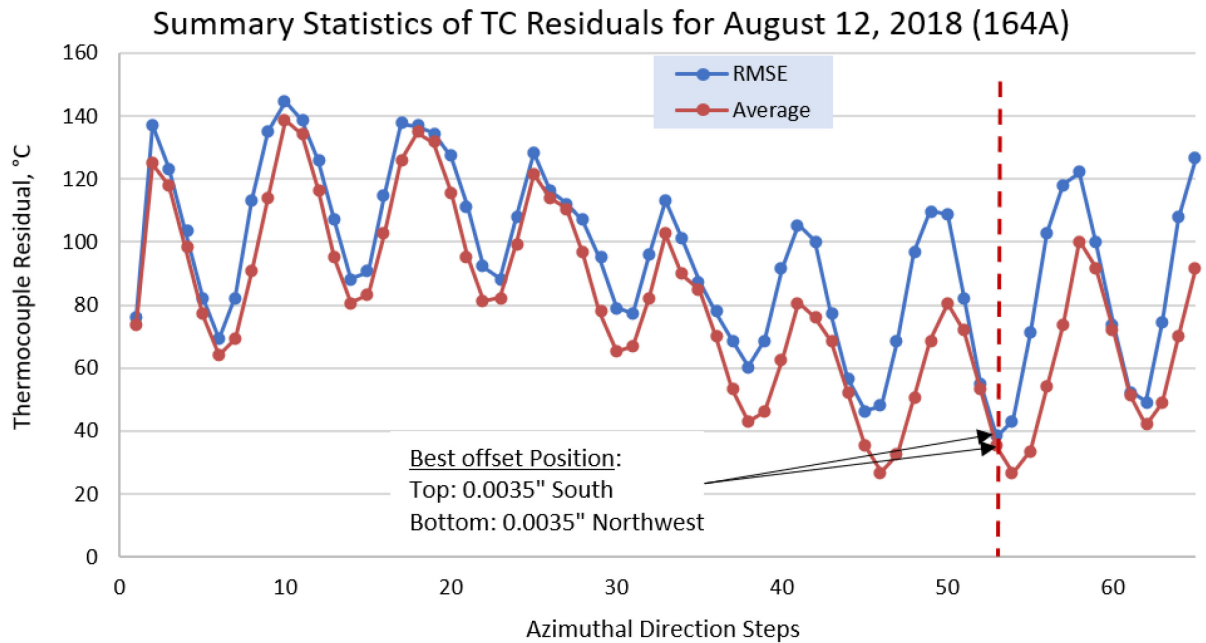


Figure 45. Average, RMSE, and standard deviation of the TC residuals (excluding TC-1-4) as a function of offset direction step (Table 2), showing the best offset position to be at Step 53 for August 12, 2018.

Figure 46 shows a temperature contour plot for a 0.25 in. axial slice in which the highest temperature occurs for the best-fit offset with TC-1-4 excluded. The maximum temperature of 1402°C occurs in stack 6, compact level 8, in the south-southwest section.

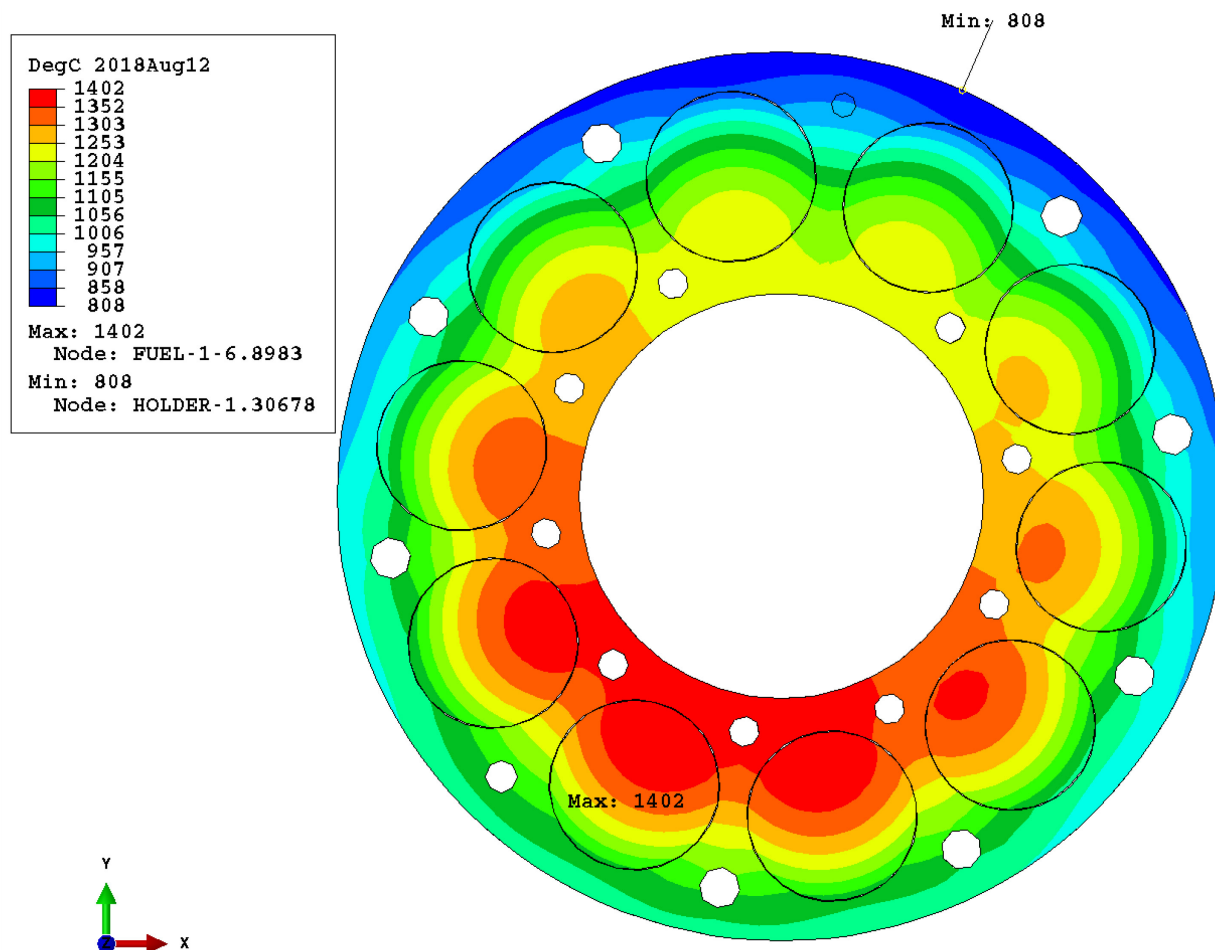


Figure 46. Temperature (°C) contour plot of the 0.25 in. slice (level 8) in which the highest temperature occurs for August 12, 2018, the best-fit offset position being 0.0035 in. top south and 0.0035 in. bottom northwest Step 53 (excludes TC-1-4).

#### 4.2.4 September 20, 2019, ATR Cycle 166A

No TCs remained in Capsule 1 on September 20, 2019, so the best-fit offset directions from the two analyses (with and without TC-1-4) of the third date (August 12, 2018) were used (top: south or northwest; bottom: northwest) to investigate the impact of offset on capsule temperatures. Besides these best-fit offset directions, several offset distances (0.002, 0.004, and 0.006 in.) were considered in order to find the maximum possible temperature. Distances greater than 0.006 in. were not considered, as doing so would result in an unrealistic negative gas gap. Table 7 shows the highest peak fuel temperature reached (1557°C) for Compact 1-7-9 (near the top of the capsule's northwest location) when the offset was 0.006 in. northwest top and 0.006 in. northwest bottom. Thus, the highest possible fuel temperature is 135°C hotter than the peak fuel temperature of the holder with zero offset. These temperatures were computed using the finite element centroid temperatures of the finite element volumes.



Figure 47 shows, from four different perspective views, a temperature (°C) contour plot of the outer surface of the holder for Capsule 1 for September 20, 2019, with an offset of 0.006 in. for both the top and bottom in the northwest direction. The peak temperature of 1265°C occurred on the upper northwest section of the holder. The black line around the holder surface is a step change in outer dimension with a larger gas gap having been designed for the lower portion of the capsule. Figure 48 shows a cutaway temperature (°C) contour plot from four different perspective angles—slicing through the center of all the compacts in a radial fashion—for the same date, offset distance, and direction as just discussed. The peak fuel temperature of 1558°C occurred in stack 9, compact level 7. Figure 48 and Figure 49 display the finite element nodal temperatures, while Table 7 reports finite element centroidal temperatures (used in volume weighting the compact temperatures), a very slight difference.

Table 7. Capsule 1 fuel compact temperatures for various offset options for September 20, 2019 (166A).

Offset Option	Minimum Temperature °C	Average Temperature °C	Maximum Temperature °C	Maximum Temperature Compact
Zero	731	1184	1422	1-8-6
Top: 0.002 in. Southwest; Bottom: 0.002 in. Northwest	680	1181	1469	1-8-7
Top: 0.004 in. Southwest; Bottom: 0.004 in. Northwest	614	1173	1512	1-8-7
Top: 0.006 in. Southwest; Bottom: 0.006 in. Northwest	533	1159	1550	1-8-7
Top: 0.002 in. Northwest; Bottom: 0.002 in. Northwest	683	1180	1465	1-7-9
Top: 0.004 in. Northwest; Bottom: 0.004 in. Northwest	609	1166	1516	1-7-9
Top: 0.006 in. Northwest; Bottom: 0.006 in. Northwest	518	1143	<b>1557</b>	1-7-9

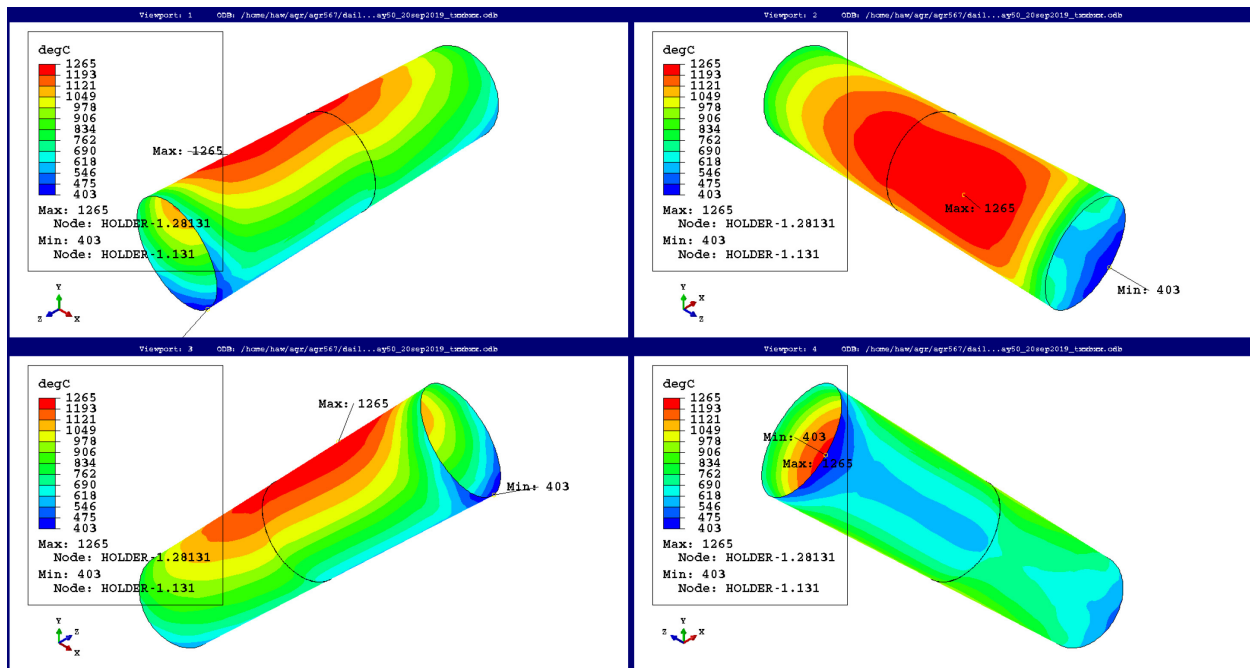


Figure 47. Surface temperature (°C) of the Capsule 1 holder for September 20, 2019—offset 0.006 in. to NW from four different perspective angles.

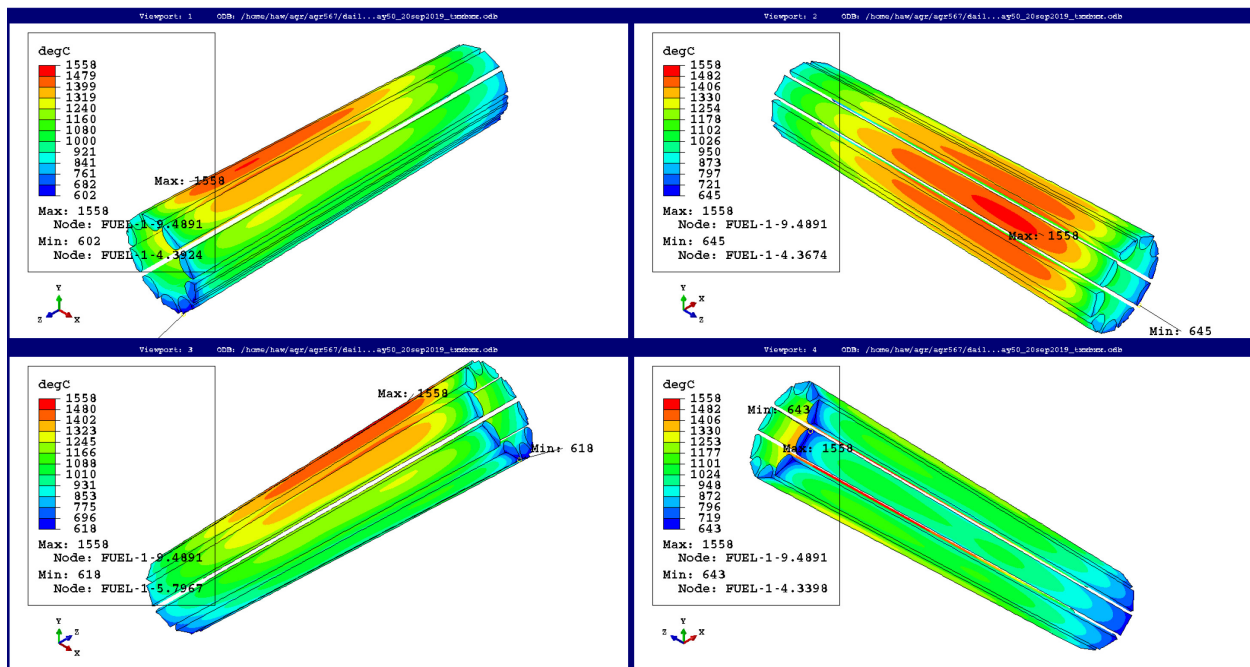


Figure 48. Cutaway view of the Capsule 1 fuel temperature (°C) for Sep 20, 2019—offset 0.006 in. to NW from four different perspective angles.

Figure 49 shows a temperature (°C) contour plot for a 0.25 in. axial slice in which the highest temperature of 1558°C occurs (stack 9, compact level 7) for September 20, 2019, with an offset configuration of 0.006 in. for the top and bottom in the northwest direction. Note that the orange temperature contour band between 1315°C and 1396°C encompasses TC-1-7 and TC-1-8.



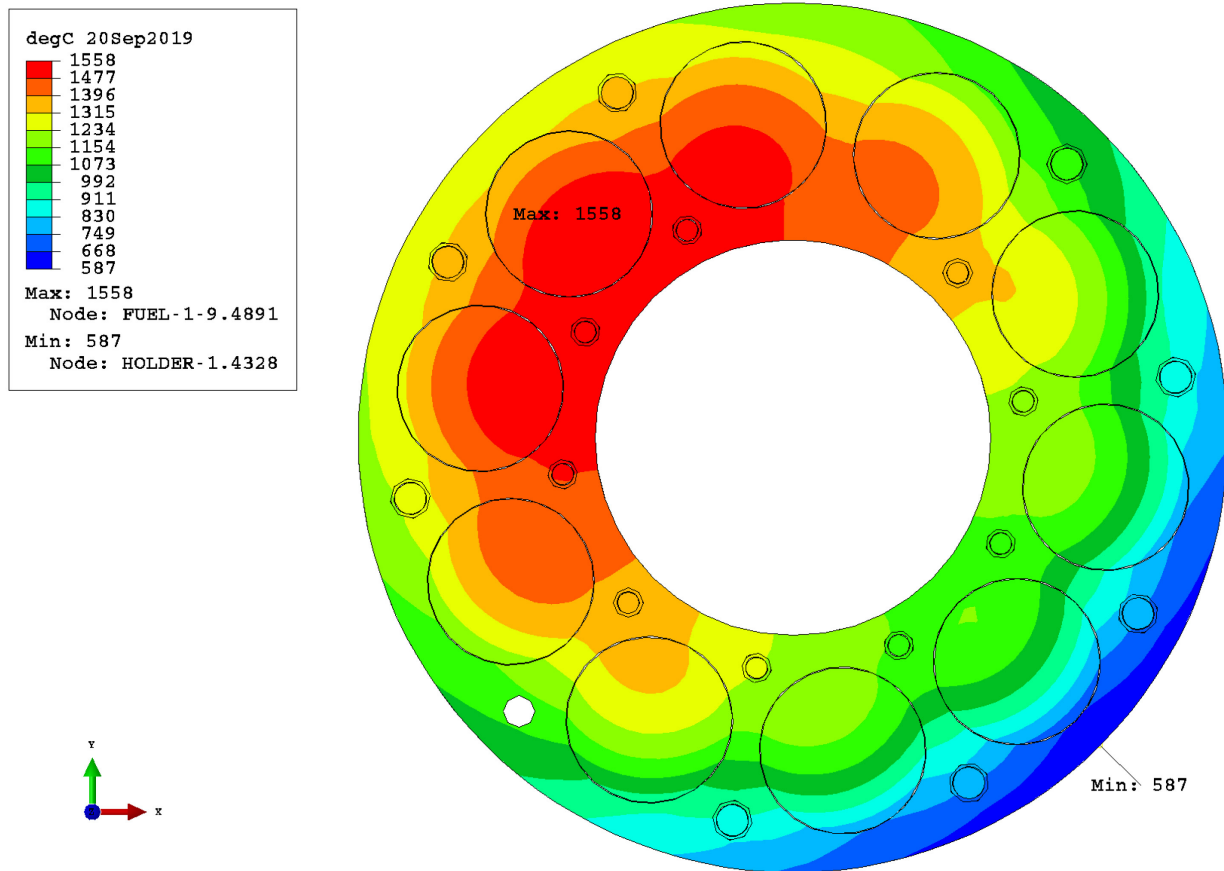


Figure 49. Temperature ( $^{\circ}\text{C}$ ) contour plot of the 0.25 in. slice (level 7) in which the highest temperature occurs for September 20, 2019, with the offset position being 0.006 in. top northwest and 0.006 in. bottom northwest.

The primary postulated reason for the massive particle failures near the end of Cycle 166A is that nickel from several Type-N TCs (e.g., TC-1-7 CAMB-N as shown in Table 3) that experienced temperatures well beyond the design limits migrated to the fuel compact and interacted with fuel particles, causing them to fail. These TCs consisted of a Ni sheath encased in a Nb sleeve. The presence of a eutectic melting point in the Nb-Ni system suggests that temperatures greater than  $1200^{\circ}\text{C}$  would result in severe degradation of the TC sheath. Therefore, temperatures along TC-1-7 (which was inserted to a depth of 8.4 in. from the top of the holder), which passed in close proximity to Compact 1-7-9, were calculated for three possible offset options for September 20, 2019 (near the end of Cycle 166A), and these are presented in Figure 50. Even though the highest temperature at the TC-1-7 tip reached a little higher than  $1000^{\circ}\text{C}$ , the peak temperature along TC-1-7 wire is  $>1200^{\circ}\text{C}$  for all offset distances and reached as high as  $1335^{\circ}\text{C}$  when the offset is 0.006 in. to the northwest. These results indicate that it was feasible for some of the TC leads in Capsule 1 to reach temperatures that would result in severe degradation and nickel migrating into the graphite holder.

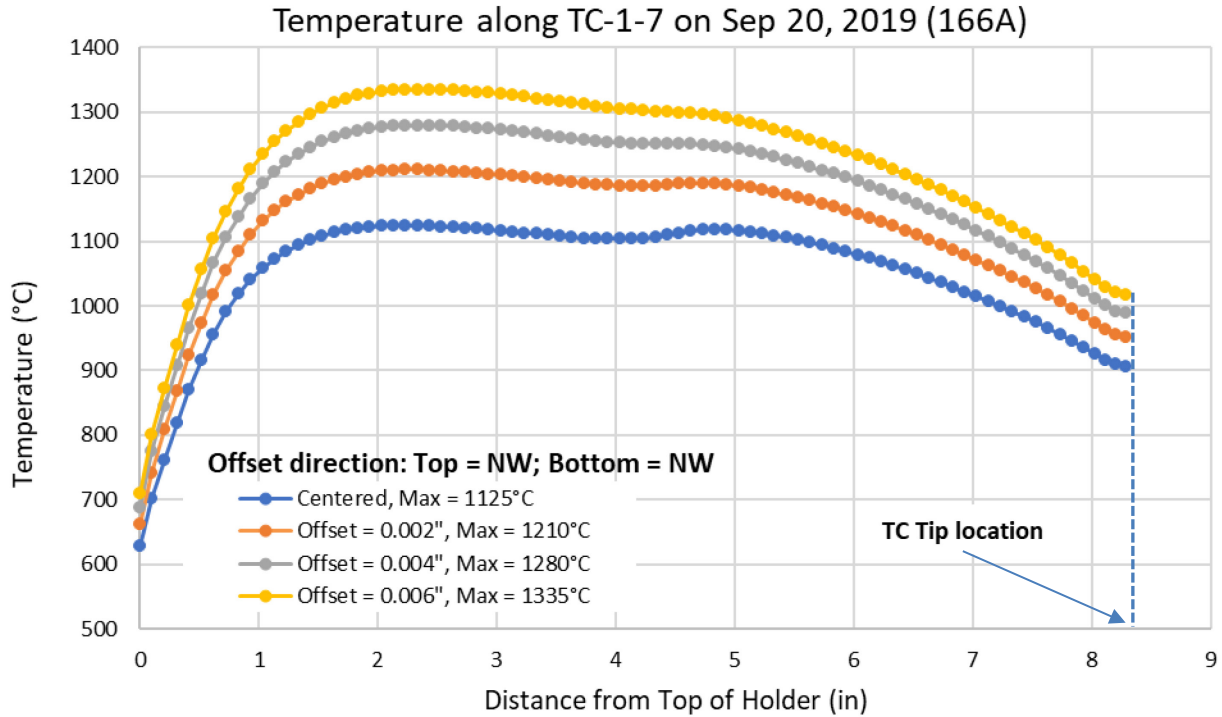


Figure 50. Temperature distribution along TC-1-7 from the holder top to tip, for four offset options: (zero, 0.002, 0.004, and 0.006 in.) for both the top and bottom shifted northwest for September 20, 2019.

#### 4.2.5 Capsule 1 Offset Discussion

A comparison was made of the best-fit options from the three dates during the first half of the AGR-5/6/7 irradiation experiment—when a number of operational TCs could be used for the RMSE calculation. Even though TC-1-4 behaved oddly relative to the other surviving TCs (as evidenced by the residuals, see Figure 40), TC-1-4 was not deemed “failed” in the data qualification report (Pham 2021). Therefore, results for August 12, 2018, were based on all seven operational TCs. For all three dates, the best-fit offset distances were similar (i.e., 0.002–0.0035 in.), but the azimuthal directions were quite different (Table 8). As shown in Table 4 through Table 6, the offset distances surrounding the best-fit distance yielded only a slightly larger RMSE, so the actual best-fit location could be similar for the three dates. For offset direction, the top offset seemed to be either the west or southwest, but the holder bottom had a wider range of best-fit offset directions (i.e., north, southeast, or northwest). This is consistent with Capsule 1 construction. Specifically, holder movement was somewhat constrained at the top by the TC leads running through the capsule head and into the holder, but the bottom did not have the same constraint. Some restraint is offered by the spring at the bottom of Capsule 1.

The offset helped significantly reduce the RMSE for all three dates, especially for March 3<sup>rd</sup> when all 17 operational TCs were still fresh (with minimal drift). For this case, the thermal model with the best-fit offset was able to match the measured TCs very well, as indicated by TC residuals scattering tightly around zero (Figure 32)—only about  $\sim 3^{\circ}\text{C}$  on average. For the two later dates when only 8 or 7 TCs remained, the reduction in the TC residual RMSE was less, and average values were positive (15 and  $23^{\circ}\text{C}$ , respectively). In general, the thermal model with the best-fit offset under-estimated temperatures at TC locations for the last two dates Figure 36 and Figure 40), especially for the last date, August 12, 2018. For this date (Figure 40), TC residuals are largely positive, except for TC-1-4, which varied within a wider range. This could be an indication that the thermal model experienced a gradual increase in bias as

the experiment progressed, due to increasing uncertainty in material properties as a function of temperature and neutron fluence (i.e., rate of the holder dimension change).

Table 8. Summary of best-fit options for three dates in 2018.

Date – Cycle	Distance, in.	Direction	No. of TCs	RMSE change (zero to best-fit), °C	Average residual, °C
March 3 – 162B	T- 0.002 B- 0.0035	T- West B- North	17	77.9 to 44.4	3.0
July 15 – 164A	T- 0.003 B- 0.003	T- West B- Southeast	8	65 to 53.8	15.3
August 12 – 164A	T- 0.0035 B- 0.0035	T- Southwest B- Northwest	7	73.6 to 47.9	22.6

Table 9 shows the Capsule 1 fuel compact temperatures (minimum, maximum, and average), as well as the corresponding compacts for the zero and best-fit offset for the selected dates. These temperatures were computed using the finite element centroid temperatures of the finite element volumes. For zero offset and best-fit offset, the hottest and coldest compacts stayed at the same level (the second number in the compact name), but the stack (the third number in the compact name) changed as the holder shifted azimuthally. This occurred because, when the holder moves closer to the capsule wall, the fuel temperature decreases, and vice versa. The offset led to a small reduction in capsule average temperature but a wider temperature range for Capsule 1 compacts (lower minimum temperature and higher maximum temperature). The hottest compact switched to the stack located next to the wider gas gap, and the coldest compact switched to the stack next to the narrower gas gap.

The peak compact temperatures are near the northwest location, where deposits on the Capsule 1 holder exterior surface were observed and are interpreted as an indication of where the capsule temperatures were highest (Stempien, Palmer, and Pham 2022). Figure 51 shows a photo of the Capsule 1 holder during PIE showing deposit stripes along the northwest outer side. Thus, the selected offset for the fourth date (September 20, 2019) analysis was assumed to be the direction that would result in peak temperatures in the northwest region.

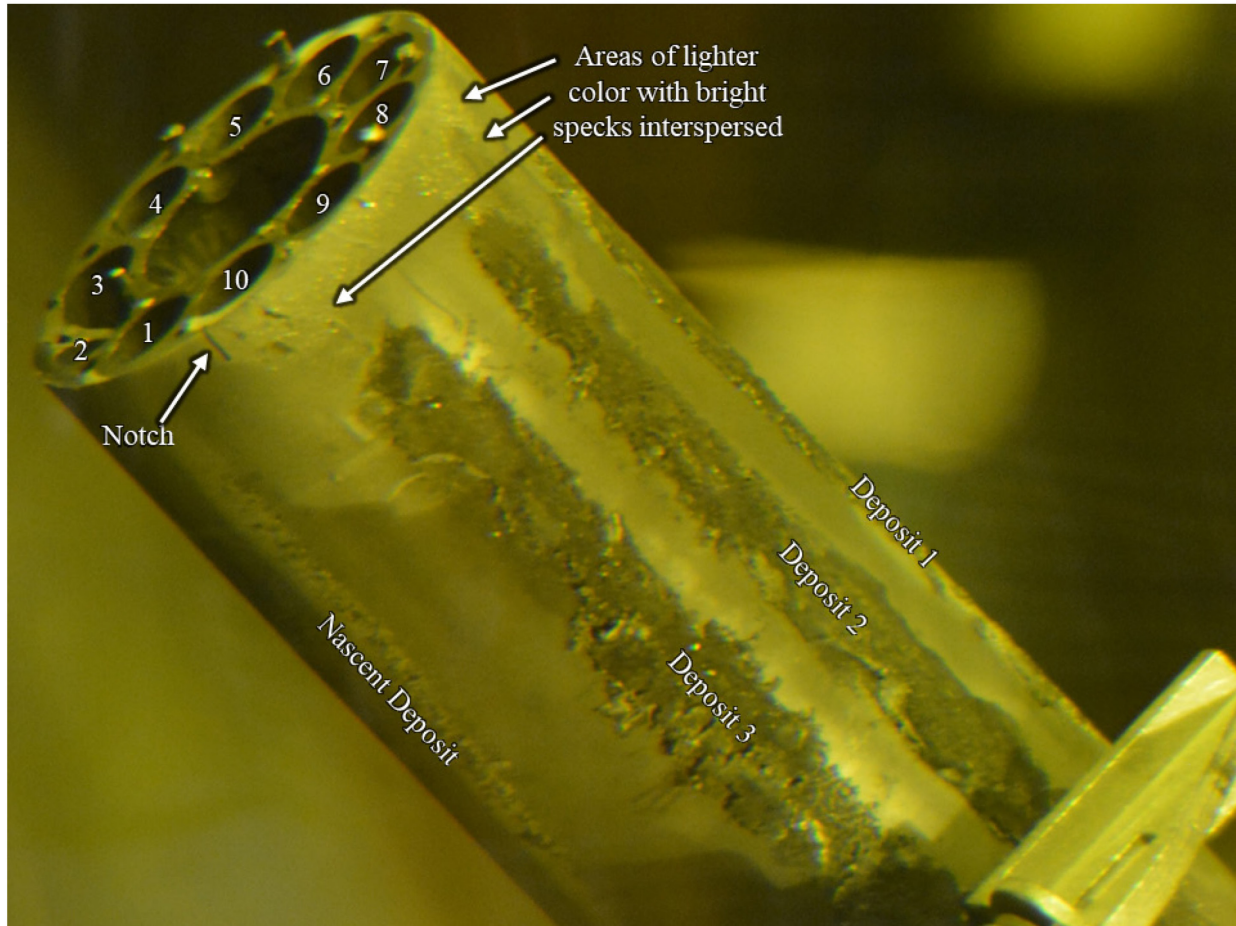


Figure 51. Photo of the holder showing the fuel stacks and major deposits.

Table 9. Capsule 1 fuel compact temperatures for zero and best-fit offset for four selected dates. Red indicates hottest compacts.

	Zero offset			Best-fit offset		
	Minimum	Maximum	Average	Minimum	Maximum	Average
March 3, 2018 (162B): Top: 0.002 in. West; Bottom: 0.0035 in. North						
Temperature, C	728	1350	1126	664	1414	1118
Compact name	1-1-1	1-7-7	—	1-1-5	1-7-9	—
July 15, 2018 (164A): Top: 0.003 in. West; Bottom: 0.003 in. Southeast						
Temperature, C	662	1319	1082	615	1374	1078
Compact name	1-1-1	1-8-5	—	1-1-9	1-8-7	—
August 12, 2018 (164A): Top: 0.0035 in. Northwest; Bottom: 0.0035 in. Northwest						
Temperature, C	652	1336	1086	589	1418	1080
Compact name	1-1-1	1-8-7	—	1-1-9	1-8-7	—
September 20, 2019 (166A): Top: 0.006 in. Northwest; Bottom: 0.006 in. Northwest (maximum offset)						
Temperature, C	731	1422	1184	518	1557	1143
Compact name	1-9-2	1-8-6	—	1-9-4	1-7-9	—

### 4.3 Capsule 2 Offset Holder Analysis

Capsule 2 was in the middle of the AGR-5/6/7 test train on top of Capsule 1. Capsule 2 contained 24 fuel compacts with calculated TA-VA compact temperatures at the end of irradiation between 752°C and 890°C when two low-power PALM cycles were excluded (Pham et al. 2021) and contained only eight Type-N TCs (Figure 52). These TCs terminated at different depths, as shown in Table 10. All of them were operational until the start of the third cycle (i.e., ATR Cycle 164A), and the last TC survived until the end of the sixth Cycle 166B (Pham 2021). Table 10 also shows the type of each TC, along with the cycle in which each TC failed.

Table 10. Depth of TC tip in the holder, type or material, and failure cycle for the eight TCs in Capsule 2.

TC Number	Penetration, in.	Type or material	Failure during cycle
TC-2-1	2.4	STD-N	164A
TC-2-2	2.4	STD-N	164B
TC-2-3	4.4	STD-N	165A
TC-2-4	4.4	STD-N	164B
TC-2-5	6.4	STD-N	166B
TC-2-6	6.4	STD-N	166B
TC-2-7	4.4	STD-N	164B
TC-2-8	2.4	STD-N	164A

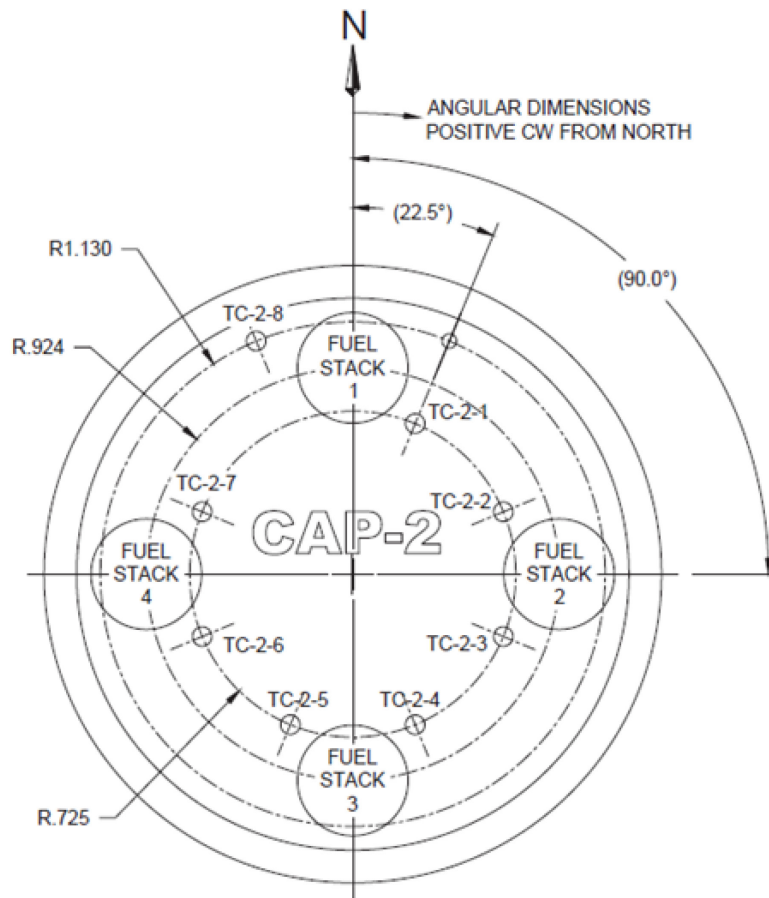


Figure 52. Cross section showing the eight TCs embedded throughout the Capsule 2 holder.

Figure 53 shows the original analysis TC residuals with the Capsule 2 holder centered. For Capsule 2, three time-steps over the AGR-5/6/7 irradiation were selected for analysis: March 3, 2018 (Cycle 1 162B), October 8, 2018 (Cycle 4 164B), and April 20, 2020 (Cycle 9 168A). The reasoning behind these selected dates is:

- March 3, 2018 (162B): This was near the beginning of irradiation, and the temperatures had been raised to the target range. All eight TCs were still fresh (with minimal drift) and operational, allowing for the best offset optimization.
- October 8, 2018 (164B): This date was selected to investigate whether the offset was stable over time, six of the eight TCs were still operational (shortly after this date another TC failure brought the number of operational TCs to five).
- April 20, 2020 (168A): This date was selected since Figure 24 shows it as the highest temperature during irradiation. The maximum allowable offset was implemented to find the resultant highest temperature.

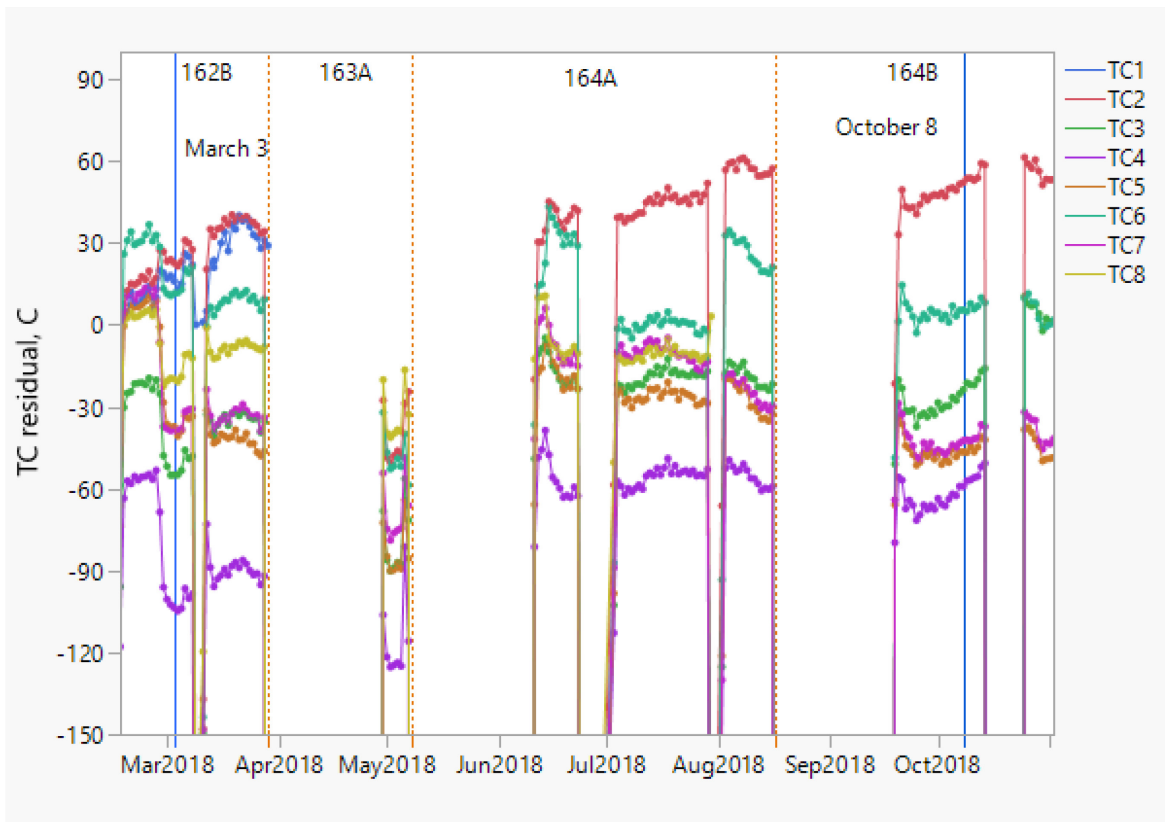


Figure 53. Capsule 2 TC residuals during the first four cycles, showing the first two selected dates (blue vertical lines).

Figure 54 shows the HGRs for the fuel compacts in Capsule 2 for the first two dates mentioned above. These values were imported from the neutronics analysis (Sterbentz 2020). Note that the HGRs for Oct 8, 2018, are lower, as the fuel had been partially depleted. Figure 55 shows the cumulative fast neutron fluence for the two dates chosen. This has a direct impact on the thermal conductivity of the graphite holder and gap width, due to the holder shrinkage. Thus, the HGR and fast neutron fluence are important inputs that affect the calculated temperatures.



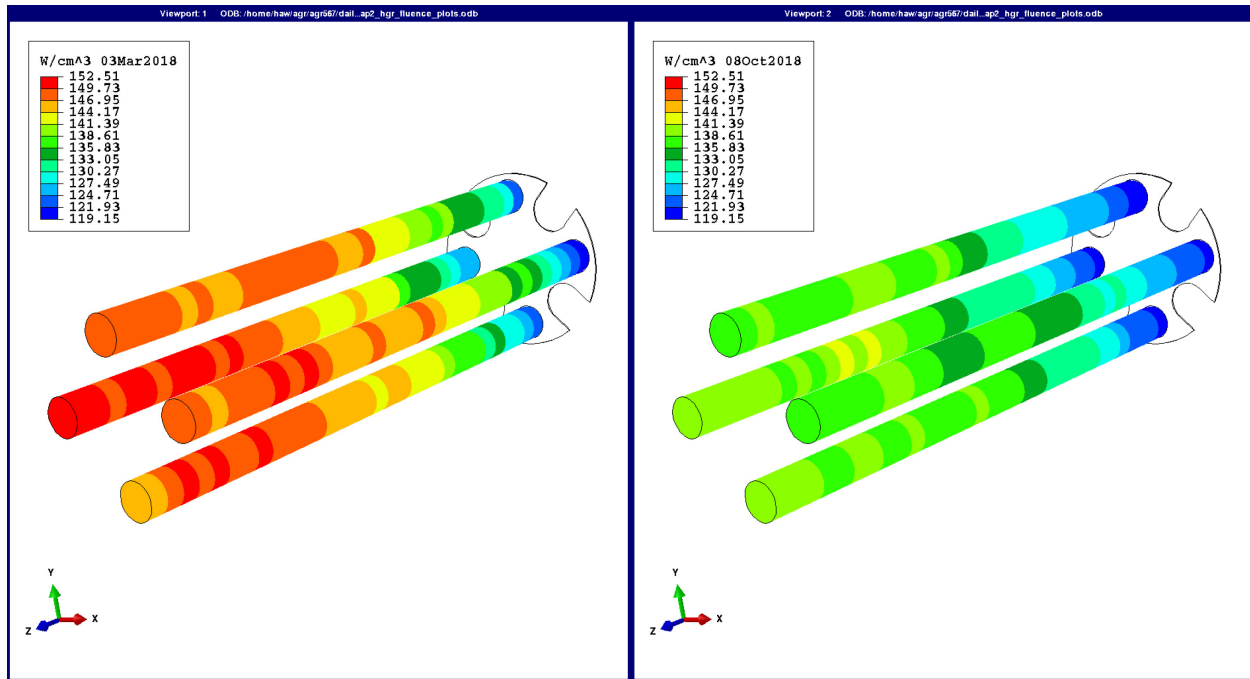


Figure 54. Heat generation rates ( $\text{W}/\text{cm}^3$ ) for the Capsule 2 fuel for March 3, 2018 (left), and Oct 8, 2018 (right).

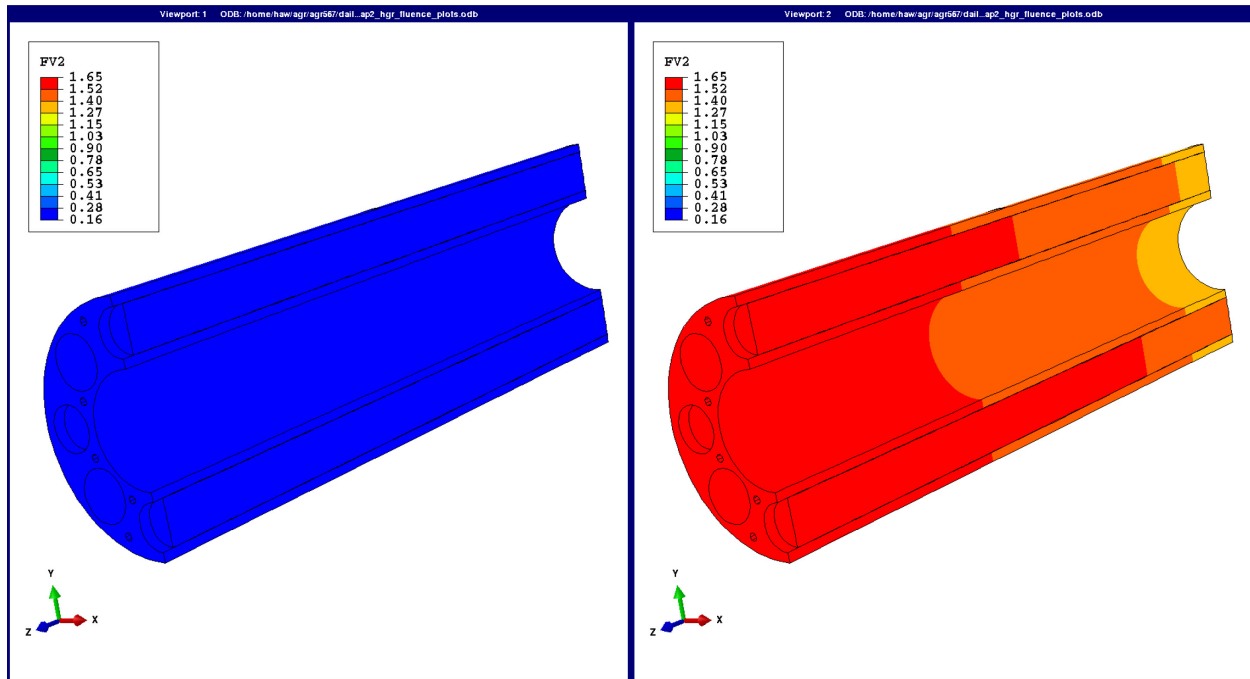


Figure 55. Fast neutron fluence ( $1.0 \times 10^{25}$  neutrons/ $\text{m}^2$  ( $E_n > 0.18$  MeV)) for the Capsule 2 holder for March 3, 2018 (left) and Oct 8, 2018 (right).

#### 4.3.1 March 3, 2018, ATR Cycle 162B

Table 11 shows the best-fit directions for Capsule 2 that resulted in the minimum RMSE for each pair of nine offset distances, which is reduced from the original 16 distances based on the results of Capsule 1,

calculated for March 3, 2018 (162B). The top offset of 0.004 in. to the northeast and the bottom offset of 0.003 in. to the west (orange cell) resulted in the minimum residual RMSE from eight operational TCs (minimum RMSE value of 26.0°C versus 51.9°C for centered [zero offset] holder). Other offset options also yielded very close TC residual RMSEs to the best fit.

The TC residuals (Figure 56) and the average and RMSE values (Figure 57) as a function of the 65 azimuthal position clearly indicate that the best-fit offset position (t4b3) resulted in the smallest spread of TC residuals, as they are scattered around the zero horizontal line (~18°C average). This indicates a well-balanced thermal model with small bias. The TC residual plots for the zero and best-fit offsets (Figure 58) also show a significant reduction in residuals for most of the eight operational TCs in Capsule 2. Figure 59 shows a temperature contour plot for a 0.25 in. axial slice in which the highest temperature occurs for the best-fit offset. The maximum temperature of 962°C occurs in Stack 1, Compact Level 4 in the north direction.

Table 11. Capsule 2 best-fit options for each of the nine offset distances, best-fit direction, and minimum RMSE for March 3, 2018 (162B). The best-fit option is shaded orange.

March 3, 2018 (162B)—All Eight TCs Remained: Distances / Directions / Minimum RMSE		
t2b2 / tNEbW / 36.3	t2b3 / tNEbW / 37.4	t2b4 / tNEbW / 40.4
t3b2 / tNEbW / 30.7	t3b3 / tNEbW / 30.8	t3b4 / tNEbW / 33.2
t4b2 / tNEbW / 27.3	t4b3 / tNEbW / 26.0	t4b4 / tNEbW / 27.5

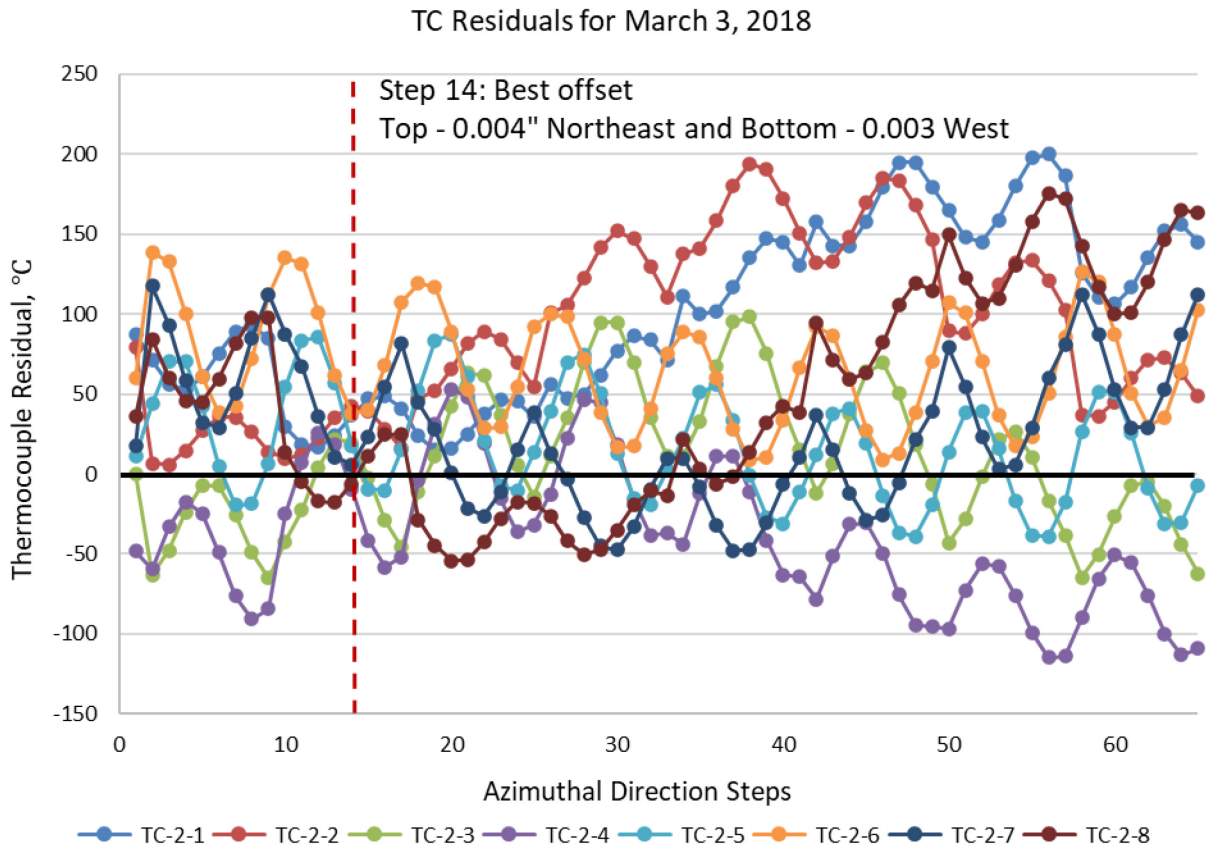


Figure 56. Capsule 2 residuals of eight TCs as a function of offset direction (Table 2) for the best-fit offset, showing the smallest variation of TC residuals to be at Step 14 for March 3, 2018 (Cycle 162B).



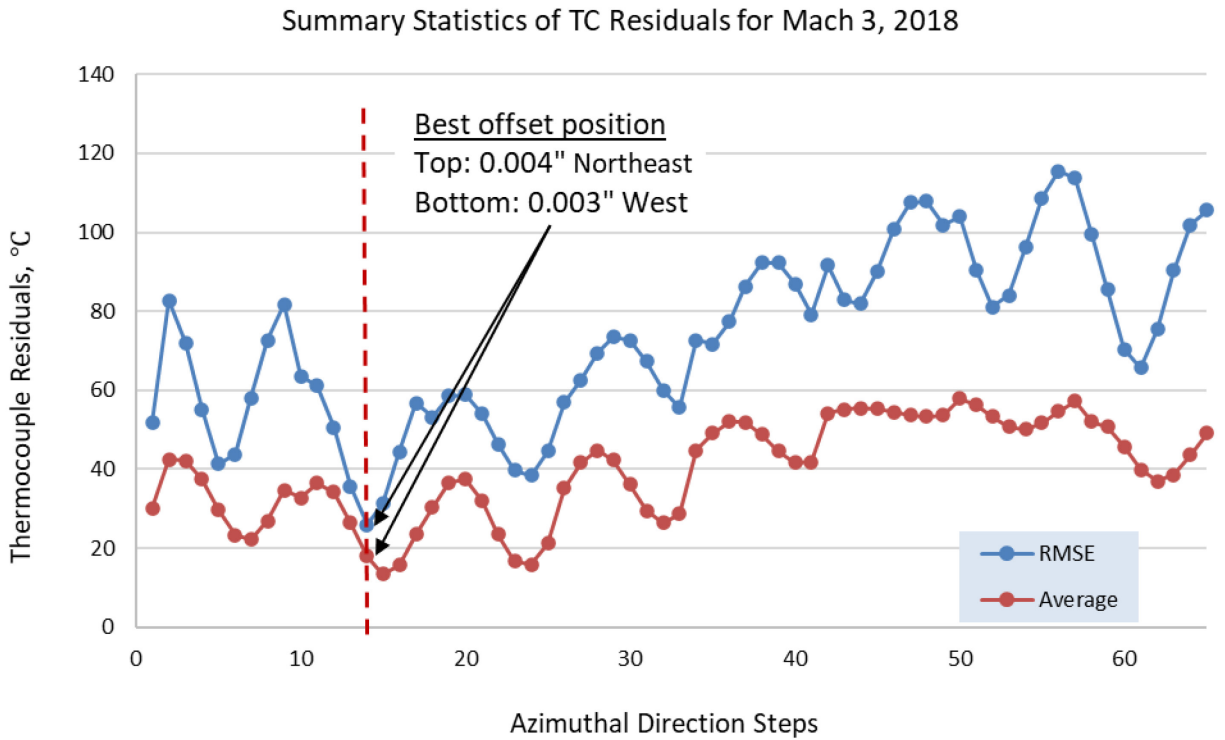


Figure 57. Capsule 2 average and RMSE residuals from the eight TCs as a function of offset direction step (Table 2), showing the best offset position to be at Step 14 for March 3, 2018 (Cycle 162B).

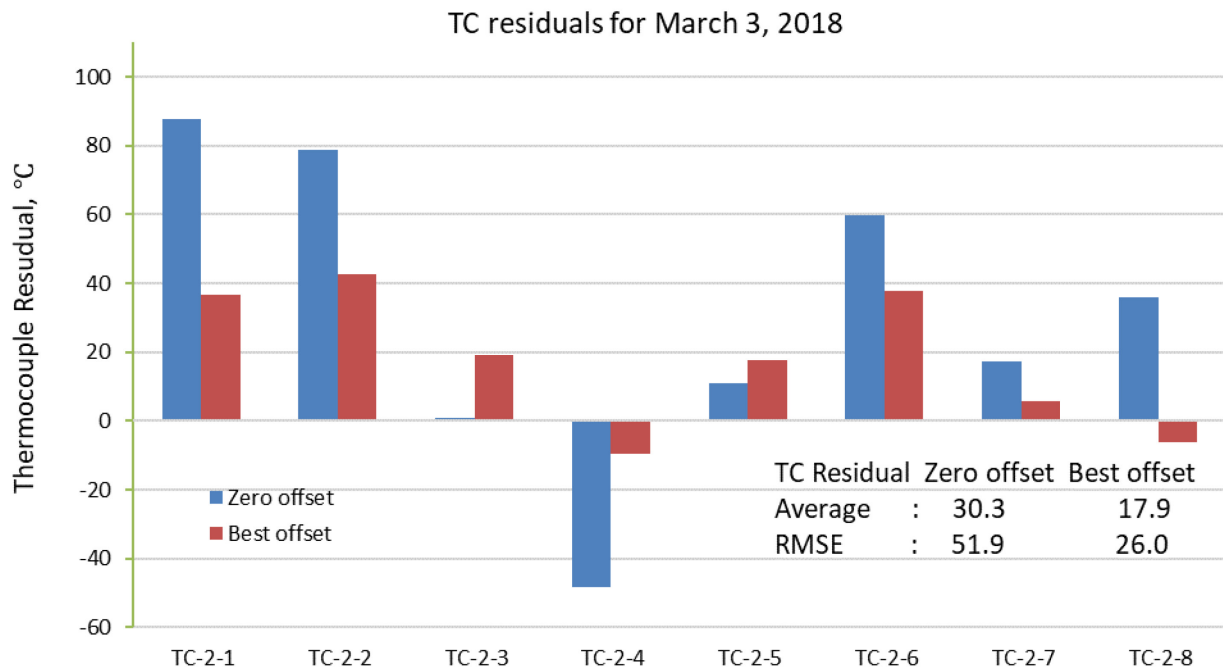


Figure 58. Capsule 2 TC residuals of zero and best-fit offset for March 3, 2018 (Cycle 162B).

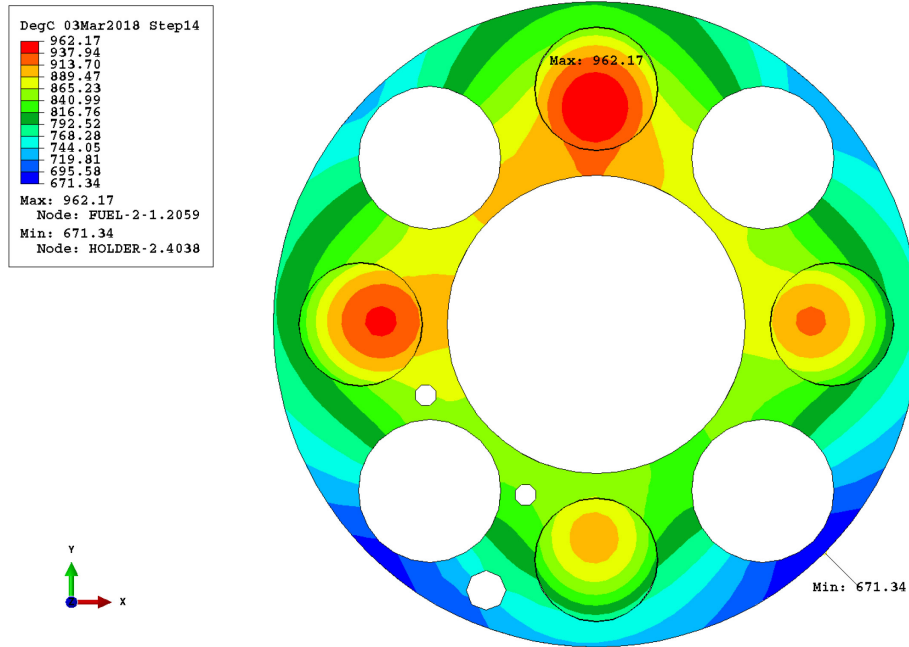


Figure 59. Capsule 2 temperature (°C) contour plot of the 0.25 in. slice (level 4) in which the highest temperature occurs for March 3, 2018, the best-fit offset position being 0.004 in. top northeast and 0.003 in. bottom west (Step 14).

#### 4.3.2 October 8, 2018, ATR Cycle 164B

Table 12 shows the best-fit directions for Capsule 2 that resulted in the minimum RMSE for each pair of nine offset distances calculated for October 8, 2018 (164B). The top offset of 0.004 in. to the east and the bottom offset of 0.003 in. to the northwest (orange cell) resulted in the minimum residual RMSE from six operational TCs (minimum RMSE value of 18.5°C versus 41.0°C for centered holder). Other offset options also yielded very close TC residual RMSEs to the best fit.

The TC residuals (Figure 60) and the average and RMSE values (Figure 61) as a function of the 65 azimuthal positions clearly indicate that the best-fit offset position (t4b3) resulted in the smallest spread of TC residuals, as they are scattered tightly around the zero horizontal line (only ~3°C average). This indicates a well-balanced thermal model with minimal bias. The TC residual plots for the zero and best-fit offsets (Figure 62) also show a significant reduction in residuals for four of the six operational TCs in Capsule 2. Figure 63 shows a temperature contour plot for a 0.25 in. axial slice in which the highest temperature occurs for the best-fit offset. The maximum temperature of 971°C occurs in Stack 1, Compact Level 4 in the north direction.

Table 12. Capsule 2 best-fit options for each of the nine offset distances, best-fit direction, and minimum RMSE for October 8, 2018 (164B). The best-fit option is shaded orange.

October 8, 2020 (164B)—Six TCs Remained: Distances / Directions / Minimum RMSE		
t2b2 / tEbNW / 27.3	t2b3 / tEbNW / 28.2	t2b4 / tEbNW / 32.2
t3b2 / tEbNW / 23.5	t3b3 / tEbNW / 21.8	t3b4 / tEbNW / 24.4
t4b2 / tNEbW / 20.3	t4b3 / tEbNW / 18.5	t4b4 / tEbNW / 18.5

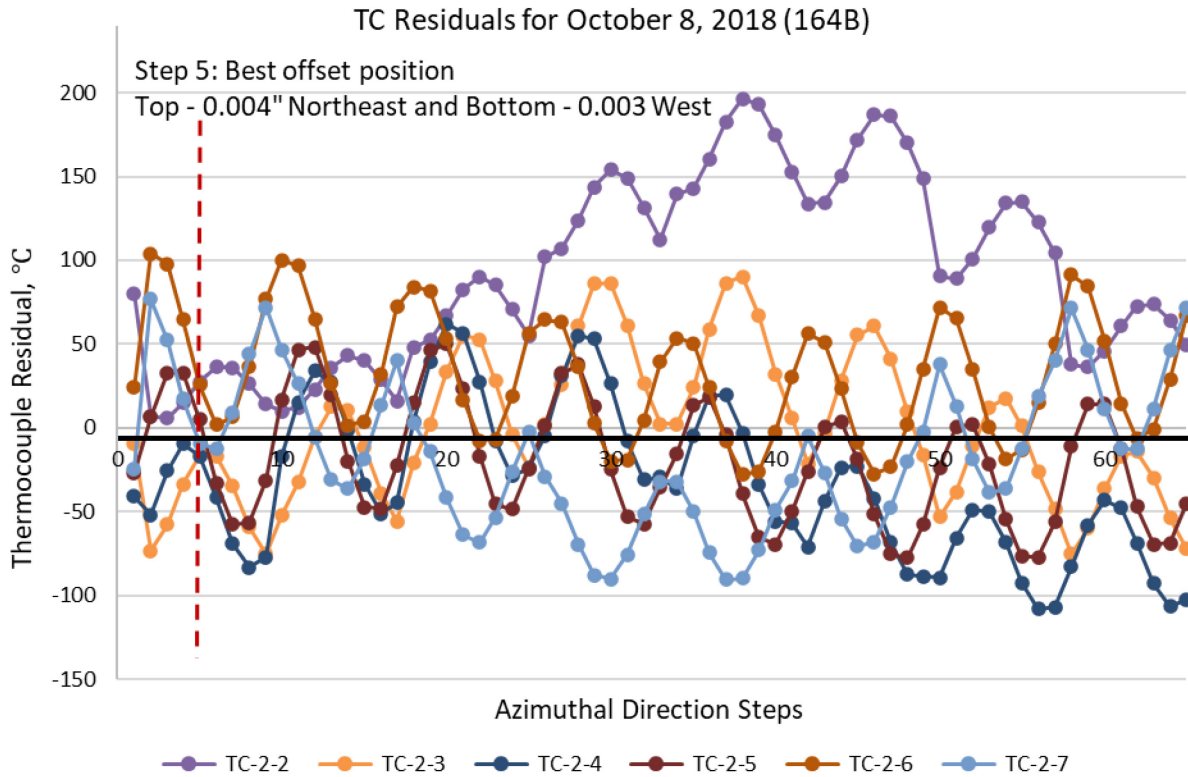


Figure 60. Capsule 2 residuals of six TCs as a function of offset direction (Table 2) for the best-fit offset, showing the smallest variation of TC residuals to be at Step 5 for October 8, 2018 (Cycle 164B).

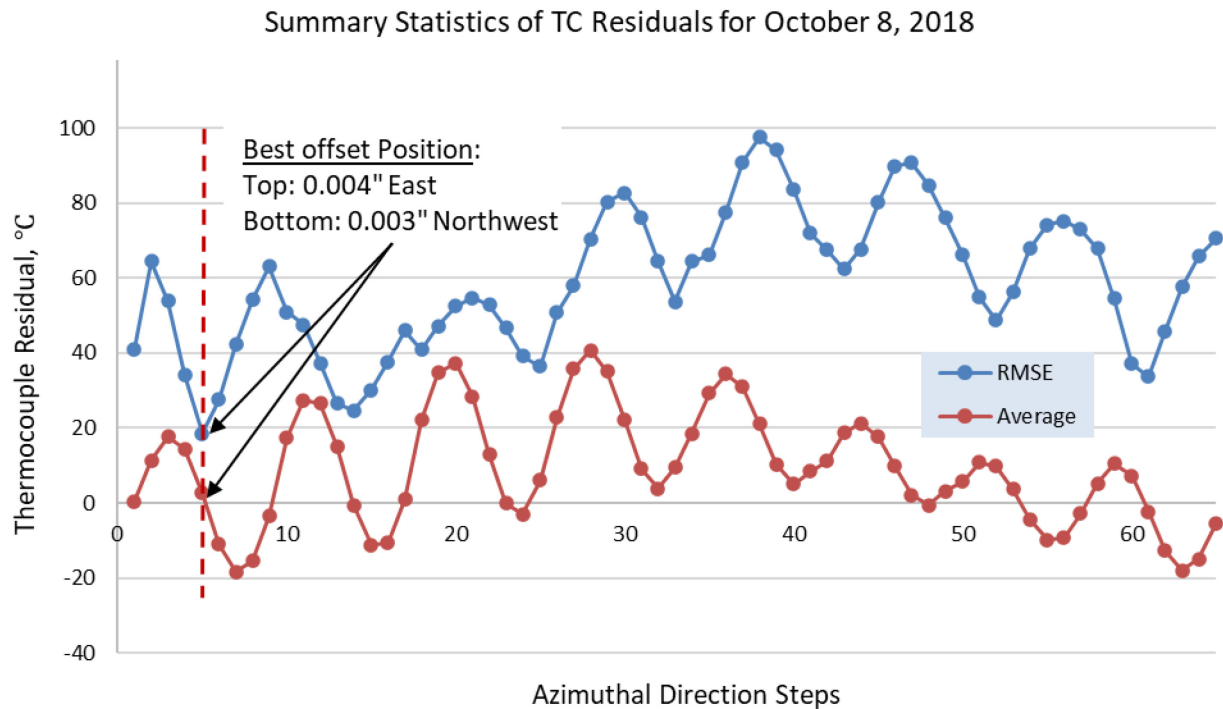


Figure 61. Capsule 2 average and RMSE residuals from the six TCs as a function of offset direction step (Table 2), showing the best offset position to be at Step 5 for October 8, 2018 (Cycle 164B).

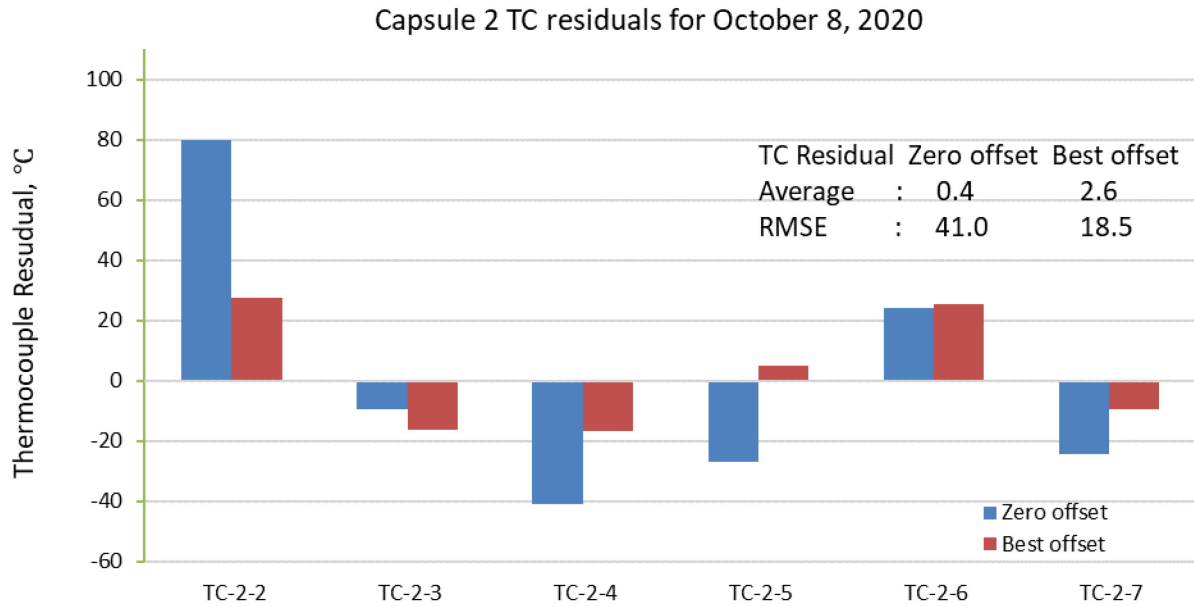


Figure 62. Capsule 2 TC residuals of zero and best-fit offset for October 8, 2018 (Cycle 164B).

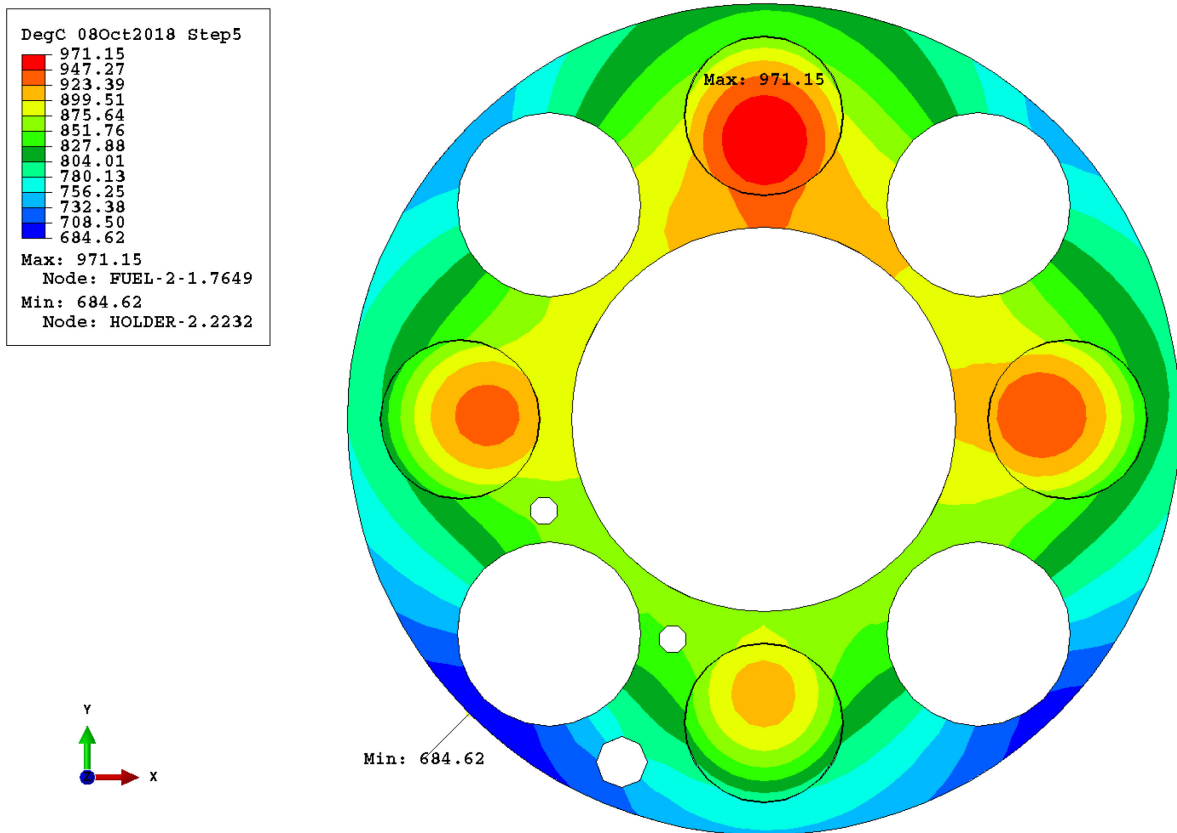


Figure 63. Temperature (°C) contour plot of the 0.25 in. slice (Level 4) in which the highest temperature occurs for October 8, 2018, the best-fit offset position being 0.004 in. top east and 0.003 in. bottom northwest of Capsule 2 holder (Step 5).

### 4.3.3 Highest Possible Temperature, April 20, 2020, ATR Cycle 168A

An analysis was performed to find the highest possible temperature in Capsule 2 during any point in time of the irradiation. Figure 24 shows that the highest calculated temperature was near EFPD 320 for Capsule 2. This was taken as April 20, 2020 (Cycle 168A). For the original centered calculation (Hawkes 2021), the peak temperature was in the south stack (Stack 3). By increasing the offset gap to its maximum allowable value in the south, it would yield the highest possible temperature. After iterating to find the maximum possible offset and considering negative gas gaps, an offset of 0.0068 in. in the south yielded the highest possible temperature. Higher offset values were tried but would not converge due to a prediction of a negative gap during the iterations.

Figure 64 shows a temperature contour plot for April 20, 2020, of the Capsule 2 fuel stacks with a one-quarter slice being taken out to show the inner fuel temperature regions. The bottom Grafoil was added on the right of fuel stacks to help with the perspective view. The fuel stack locations are labeled in the figure as Stack 1 was in the north, Stack 2 east, Stack 3 south, and Stack 4 west. Table 14 in Appendix B lists the volume average, minimum, and peak temperatures for each fuel compact with zero offset and this configuration of a 0.0068 in. offset on the south for April 20, 2020. Since the offset is in the south, the peak temperature increased from 994°C to 1111°C (for the highest temperature Compact 2-4-3, located in the middle of Stack 3 (south stack in Figure 64) near the larger gas gap. In contrast, the lowest temperature compact shifted from Compact 2-1-1 (capsule bottom north position) to Compact 2-8-1 (capsule top north position) and the minimum temperature decreased from 571°C to 349°C.

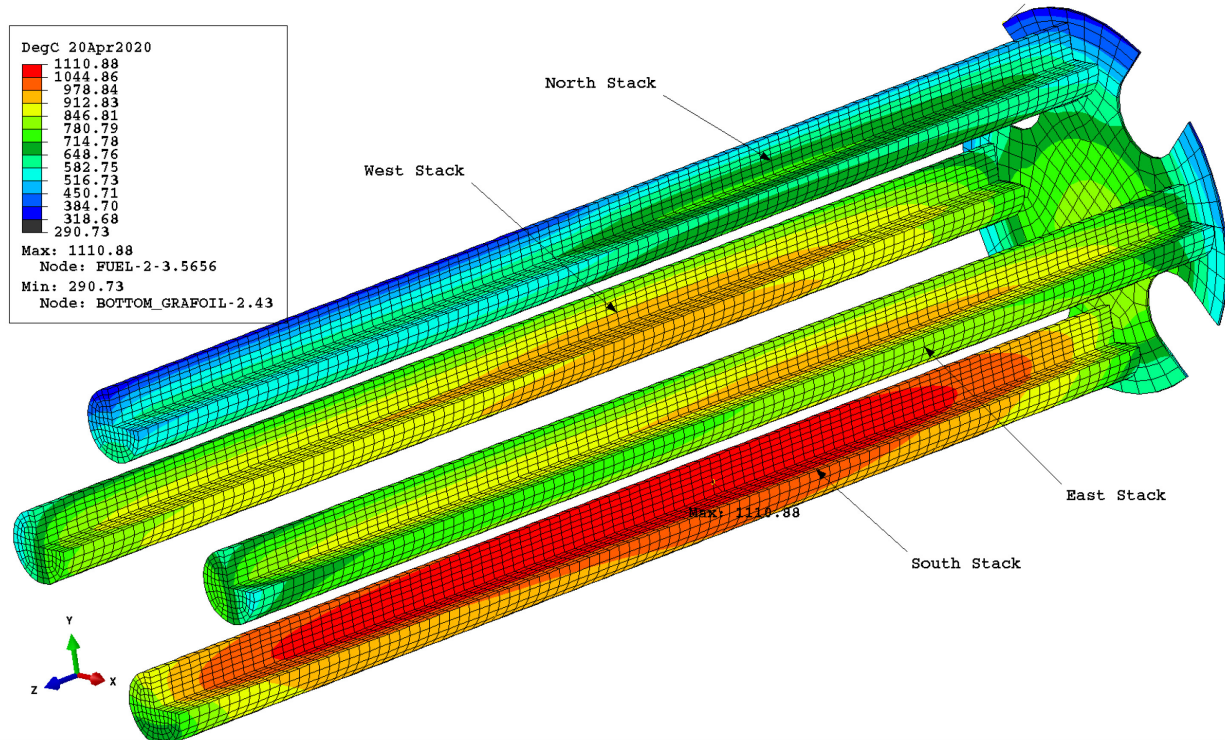


Figure 64. Temperature (°C) contours of Capsule 2 fuel with each fuel stack one-quarter slice taken out, including the bottom Grafoil (to help with perspective), for April 20, 2020, with top and bottom offset to the south at 0.0068 in.



Figure 65 shows the temperature along the length of the highest TC temperature with a peak of 1029°C. This peak temperature is well below the 1100°C value where TC degradation occurs.

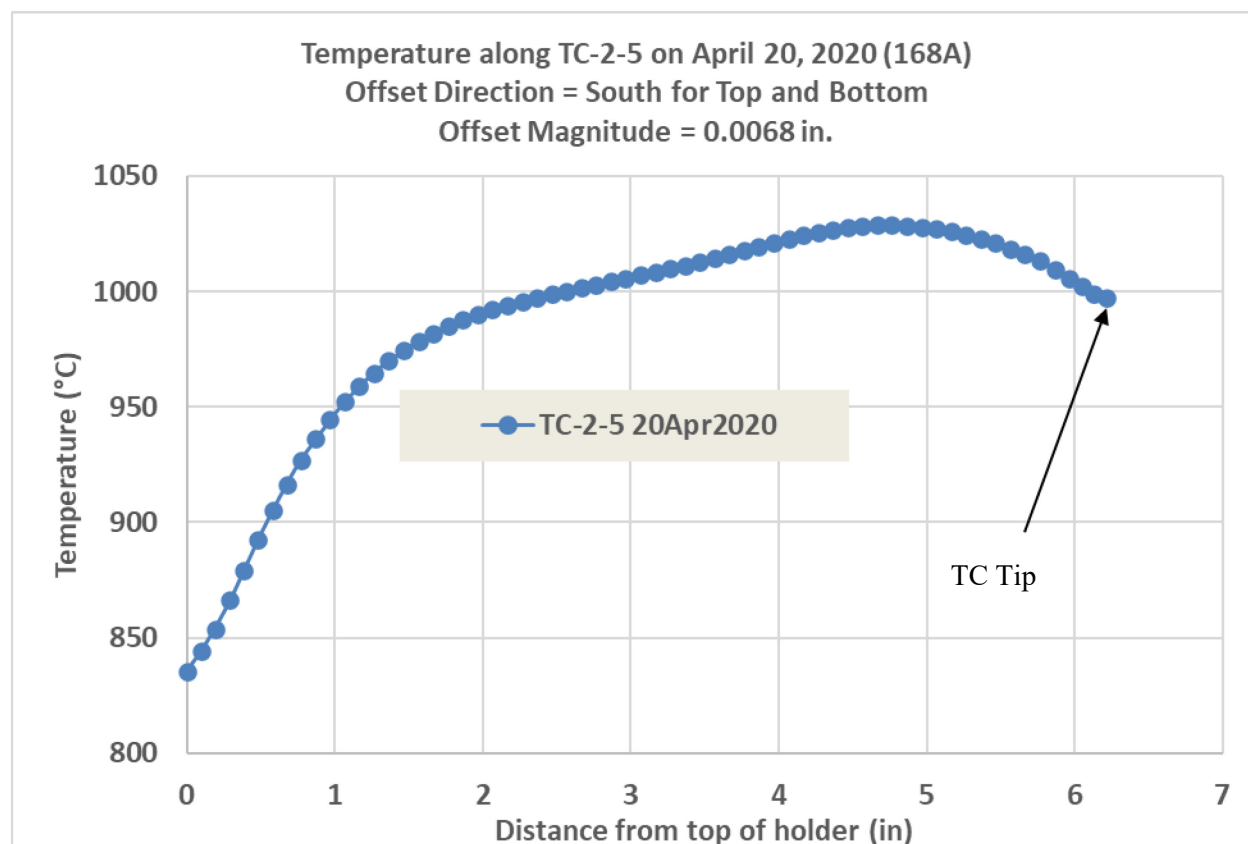


Figure 65. Temperature (°C) along TC-2-5 on April 20, 2020, with the top and bottom offset to the south and magnitude of 0.0068 in.

#### 4.3.4 Capsule 2 Offset Discussion

For Capsule 2, a comparison was made of the best-fit options from the two dates during Cycle 162B and 164B—when a number of operational TCs could be used for the RMSE calculation. For both dates, the best-fit offset distances were similar (i.e., 0.004 in. top and 0.003 in. bottom), but the azimuthal directions were different (Table 13). For offset direction, however, the top offset direction moved from the northeast to the east and the bottom offset direction moved from the west to the northwest. This is consistent with Capsule 1 holder offsets, which were not in the same direction over the irradiation time. The offset helped significantly reduce the RMSE for both dates (Table 13) when eight and six TCs remained and average values were positive (17.9°C and 2.6°C, respectively).

Table 13. Summary of best-fit options for the first two dates in 2018 for Capsule 2.

Date—Cycle	Distance, in.	Direction	No. of TCs	RMSE Change (zero to best-fit), °C	Average Residual, °C
March 3—162B	T- 0.004 B- 0.003	T- Northeast B- West	8	51.9 to 26.0	17.9
October 8—164B	T- 0.004 B- 0.003	T- East B- Northwest	6	41.0 to 18.5	2.6

Table 14 shows the Capsule 2 fuel compact temperatures (minimum, maximum, and average), as well as the corresponding compacts for the zero and best-fit offset for the selected dates. These temperatures were computed using the finite-element centroid temperatures of the finite-element volumes. For zero offset and best-fit offset, the hottest and coldest compacts stayed at the same level (the second number in the compact name), but the stack (the third number in the compact name) changed as the holder shifted azimuthally. This occurred because, when the holder moves closer to the capsule wall, the fuel temperature decreases, and vice versa. The offset led to a small reduction in capsule average temperature but a wider temperature range for Capsule 2 compacts (lower minimum temperature and higher maximum temperature). The hottest compact switched to the stack located next to the widest gas gap, and the coldest compact switched to the stack next to the narrowest gas gap. Results for April 20, 2020, in Table 14 show that the peak temperature went from 994°C when centered to the highest possible offset and temperature of 1110°C when making the gap 0.0068 in. towards the south direction for the top and bottom.

Table 14. Capsule 2 fuel compact temperatures for zero and best-fit offset for four selected dates. Red indicates hottest compacts.

	Zero Offset			Best-Fit Offset		
	Minimum	Maximum	Average	Minimum	Maximum	Average
March 3, 2018 (162B): Top: 0.004 in. Northeast; Bottom: 0.003 in. West						
Temperature, °C	597	942	833	530	961	826
Compact name	2-8-2	2-3-3	—	2-8-3	2-4-1	—
October 8, 2018 (164b): Top: 0.004 in. East; Bottom: 0.003 in. Northwest						
Temperature, °C	601	948	838	511	970	831
Compact name	2-1-2	2-3-3	—	2-8-4	2-4-1	—
April 20, 2020 (168A): Top: 0.0068 in. South; Bottom: 0.0068 in. South						
Temperature, °C	571	994	874	349	1110	826
Compact name	2-1-1	2-4-3	—	2-8-1	2-4-3	—

As seen in Table 16 (Appendix B), the variation in volume-average temperature among the four compacts at a given level is relatively small. For example, on April 20, 2020, the average temperature for the compacts at Level 4 ranged from 919°C (Compacts 2-4-1 and 2-4-2) to 930°C (Compact 2-4-3). When the offset is applied, this range increases substantially, with average temperatures ranging from 658°C (Compact 2-4-1) to 1060°C (Compact 2-4-3). This indicates that deviations in graphite holder orientation from the nominal centered geometry can result in differences in compact temperatures of several hundred degrees, contrasted with the relatively uniform temperatures observed with the centered holder.

## 5. CONCLUSIONS

Fuel compact temperatures are a crucial factor in assessing the irradiation performance of TRISO fuel particles. In the absence of direct measurement, fuel compact temperatures are calculated using a thermal model subject to simulation uncertainty to evaluate the possible maximum fuel compact temperature. The most dominant factor in the uncertainty of the calculated fuel temperature is the gas gap uncertainty due to the nub-to-shell clearance caused by a design error (Pham and Hawkes, 2022). Here, the best-fit offset of the holder was estimated based on the minimum RMSE of residuals for all the operational TCs. These results led to the following conclusions:

1. For Capsule 1, during earlier cycles (162A–164A), when numerous TCs were still operational, the best-fit offset distance varied over a specific range (0.002–0.0035 in.) for both the top and bottom of the offset, while the offset azimuthal direction varied widely, especially for the offset at the bottom. This is consistent with Capsule 1 construction. Specifically, holder movement was somewhat constrained at the top by the TC leads running through the capsule head and into the holder, but the bottom did not have this type of constraint.
2. For Capsule 1 and Capsule 2, various offsets led to slightly lower average temperatures but wider temperature variations (lower minimum and higher peak fuel temperatures).
3. For Capsule 1, the maximum offset of 0.006 in. to the northwest direction for both the top and bottom yielded a much higher temperature than the original peak fuel temperature, which increased from 1422°C to 1557°C (i.e., a 135°C increase) on September 20, 2019 (166A). This is consistent with the hypothesized cause of massive particle failure near the end of Cycle 166A.
4. For Capsule 1, even though the highest temperature at the tip of TC-1-7 slightly exceeded 1000°C, the temperature along the TC wire reached as high as 1335°C, assuming an offset of 0.006 in. in the northwest. This temperature significantly exceeds the temperature threshold at which Type-N TC degradation is expected. The nickel released by degradation contributed to considerable particle failures in Capsule 1.
5. For Capsule 2, the best-fit offset directions are closer to each other for the dates analyzed, relative to Capsule 1 offsets. The best-fit offset for the two dates analyzed had the top in the northeast (162B) and east (164B), while the bottom was west (162B) and northwest (164B).
6. For Capsule 2, the peak fuel temperature could reach 1110°C with the maximum-possible offset of 0.0068 in. during the last cycle (ATR Cycle 168A), and the corresponding peak TC line temperature was 1029°C.
7. For Capsule 2, the difference in average temperature of the four compacts in a single level was negligible with a centered holder geometry but could be as much as ~400°C with a severe offset holder.



## 6. REFERENCES

- ASTM. 2014. “Standard Practice for Testing Graphite and Boronated Graphite Materials for High--Temperature Gas--Cooled Nuclear Reactor Components.” American Society for Testing & Materials Standard-Designation C781-08. ASTM International, West Conshohocken, Pennsylvania.
- Dassault Systèmes. 2014. ABAQUS version 6.14-2. [www.simulia.com](http://www.simulia.com) or [www.abaqus.com](http://www.abaqus.com), Providence, Rhode Island.
- Gontard, R., and H. Nabielek. 1990. “Performance Evaluation of Modern HTR TRISO Fuels,” Forschungszentrum Julich GmbH., HTA IB 05/90. [https://inis.iaea.org/search/search.aspx?orig\\_q=RN:52011643](https://inis.iaea.org/search/search.aspx?orig_q=RN:52011643).
- Gonzo, E. E. 2002. “Estimating Correlations for the Effective Thermal Conductivity of Granular Materials.” *Chemical Engineering Journal*. 90(3): 299–302. [https://doi.org/10.1016/S1385-8947\(02\)00121-3](https://doi.org/10.1016/S1385-8947(02)00121-3).
- Hawkes, G. L., J. W. Sterbentz, J. T. Maki, and B. T. Pham. 2017. “Thermal Predictions of the AGR-3/4 Experiment with Post Irradiation Examination Measured Time-Varying Gas Gaps.” *ASME Journal of Nuclear Engineering and Radiation Science* 3(4), 041007. Paper No: NERS-17-1008; <https://doi.org/10.1115/1.4037095>.
- Hawkes, G. L., J. W. Sterbentz, and B. T. Pham, B. T. 2015. “Thermal Predictions of the AGR-2 Experiment with Variable Gas Gaps.” *Nuclear Technology*, Volume 190(3): 245–253, Technical Paper, Thermal Hydraulics, <https://doi.org/10.13182/NT14-73>.
- Hawkes, G. L., J. W. Sterbentz, J. T. Maki, and B. T. Pham. 2012. “Daily Thermal Predictions of the AGR-1 Experiment with Gas Gaps Varying with Time.” Paper #12111. In proceedings of the International Congress on the Advances in Nuclear Power Plants (ICAPP 2012), Chicago, IL, Jun 24–28, 2012.
- Hawkes, G. L. 2021. “AGR-5/6/7 Daily As-Run Thermal Analyses.” ECAR-5633, Idaho National Laboratory, Idaho Falls, ID.
- MCNP. 2017. MCNP Code Manual, <https://mcnp.lanl.gov/references.shtml>, Los Alamos National Laboratory, accessed Dec 2017.
- Mitchell, T. R. 2022. “Technical Program Plan for INL Advanced Reactor Technologies Advanced Gas Reactor Fuel Development and Qualification Program.” PLN-3636, Rev. 11, Idaho National Laboratory, Idaho Falls, ID. <https://www.osti.gov/biblio/1776792-technical-program-plan-inl-advanced-reactor-technologies-advanced-gas-reactor-fuel-development-qualification-program>.
- NDMAS. 2021. Nuclear Data Management and Analysis System, <https://ndmashome.inl.gov/htr/agrSite/agrIrrSite/AGR567IrrSite/SitePages/Home.aspx>, AGR5\_DailyIrrad.xlsx, accessed Aug 2021.
- Kestin, J., et. al. 1984. “Equilibrium and Transport Properties of the Noble Gases and Their Mixtures at Low Density.” *Journal of Physical and Chemical Reference Data* 13(1):229–303. <https://doi.org/10.1063/1.555703>.
- Konings, R. J. M. 2012. “Comprehensive Nuclear Materials, Volume 4, Radiation Effects in Structural and Functional Materials for Fission and Fusion Reactors.” Section 4.11.5.7 Table 9, ISBN: 978-0-08-056033-5, 2012 Copyright Elsevier.
- Palmer, J. A., A. E. Skifton, W. D. Swank, D. C. Haggard, A. C. Matthews, and D. L. Cotel. 2022. “Thermocouple Testing in Support of the AGR-5/6/7 Experiment.” INL/RPT-22-66266. Idaho National Laboratory, Idaho Falls, ID. <https://doi.org/10.2172/1871307>.

- Pham, B. T., and G. L. Hawkes. 2022. "Uncertainty Quantification of Calculated Temperatures for AGR-5/6/7 Experiment." INL/RPT-22-67132, Rev. 0. Idaho National Laboratory, Idaho Falls, ID. <https://www.osti.gov/biblio/1906513>.
- Pham, B.T. 2021. "AGR-5/6/7 Data Qualification Report for ATR Cycles 162B through 168A." INL/EXT-21-62180. Idaho National Laboratory, Idaho Falls, ID. <https://www.osti.gov/biblio/1777247>.
- Pham, B. T., J. J. Palmer, D. W. Marshall, J. W. Sterbentz, G. L. Hawkes, and D. M. Scates. 2021. "AGR-5/6/7 Irradiation Test Final As-Run Report." INL/EXT-21-64221. Idaho National Laboratory. <https://www.osti.gov/biblio/1822435>.
- Shibata, T., M Eto, E. Kunimoto, S. Shiozawa, K. Kazuhiro, T. Oku, and T. Maruyama. 2010. "Draft of Standard for Graphite Core Components in High Temperature Gas-cooled Reactors." Japan Atomic Energy Agency Research 2009-042. [https://inis.iaea.org/search/search.aspx?orig\\_q=RN:42011318](https://inis.iaea.org/search/search.aspx?orig_q=RN:42011318).
- Stempien, J. D. , L. Cai. 2023. "AGR-5/6/7 Irradiation Disassembly and Metrology First Look." INL/RPT-23-71033, Rev 0, Idaho National Laboratory, Idaho Falls, ID. <https://doi.org/10.2172/1960206>.
- Stempien, J. D., J. J. Palmer, B. T. Pham. 2022. "Initial Observations from AGR-5/6/7 Capsule 1." INL/RPT-22-66720, Rev 0, Idaho National Laboratory, Idaho Falls, ID. <https://www.osti.gov/biblio/1863261>.
- Sterbentz, J. W. 2020. "JMOCUP Physics Depletion Calculation for the As-Run AGR-5/6/7 TRISO Particle Experiment in ATR Northeast Flux Trap." ECAR-5321. Idaho National Laboratory, Idaho Falls, ID. <https://www.osti.gov/biblio/1774808>.
- Swank, D., J. Lord, D. Rohrbaugh, and W. Windes. 2010. "AGC-2 Graphite Pre-irradiation Data Package." INL/EXT-10-19588, Rev 1. Idaho National Laboratory, Idaho Falls, ID. <https://doi.org/10.2172/1070123>.
- Windes, W., D. Rohrbaugh, D. Swank. 2017. "AGC 2 Irradiated Material Properties Analysis." INL/EXT-17-41165 Rev 0, Idaho National Laboratory, Idaho Falls, ID. <https://doi.org/10.2172/1369362>.
- Windes, W., D. Swank, D. Rohrbaugh, and J. Lord. 2013. "AGC-2 Graphite Preirradiation Data Analysis Report." INL/EXT-13-28612, Rev 1. Idaho National Laboratory, Idaho Falls, ID. <https://doi.org/10.2172/1097190>.
- Windes, W. 2012. "Data Report on Post-Irradiation Dimensional Change in AGC-1 Samples." INL/EXT-12-26255. Idaho National Laboratory, Idaho Falls, ID. <https://www.osti.gov/biblio/1975204>.

## **Appendix A**

### **Capsule 1 Compact Temperatures for Zero and Best-fit Offset Calculated for Selected Dates**

Table 15. Capsule 1 compact temperature (minimum, maximum, and average) for zero and best-fit offset, calculated for selected dates during the AGR-5/6/7 irradiation.

Compact	Minimum Temperature (°C)	Maximum Temperature (°C)	Averaged Temperature (°C)	Minimum Temperature (°C)	Maximum Temperature (°C)	Averaged Temperature (°C)
	Zero offset – March 3, 2018 (162B)			Best-fit offset – March 3, 2018 (162B)		
1-1-1	728	986	877	769	1032	921
1-1-2	728	986	877	745	1003	893
1-1-3	733	992	881	711	968	858
1-1-4	733	998	886	675	935	825
1-1-5	741	1006	892	664	923	811
1-1-6	741	1013	898	673	944	827
1-1-7	742	1013	898	706	981	863
1-1-8	742	1008	894	748	1017	901
1-1-9	735	1002	889	771	1043	927
1-1-10	733	993	881	782	1047	934
1-2-1	871	1107	1002	927	1156	1054
1-2-2	871	1107	1002	890	1122	1018
1-2-3	875	1111	1006	844	1081	976
1-2-4	880	1118	1012	802	1046	938
1-2-5	886	1126	1020	786	1037	926
1-2-6	891	1134	1027	803	1064	948
1-2-7	891	1135	1028	848	1107	992
1-2-8	886	1130	1022	897	1148	1036
1-2-9	881	1124	1016	933	1174	1067
1-2-10	875	1113	1007	944	1176	1072
1-3-1	957	1199	1094	1015	1246	1146
1-3-2	957	1196	1094	972	1206	1105
1-3-3	959	1202	1098	921	1165	1061
1-3-4	964	1212	1105	879	1136	1026
1-3-5	970	1222	1113	866	1134	1018
1-3-6	975	1228	1120	888	1164	1045
1-3-7	976	1230	1121	939	1211	1094
1-3-8	972	1228	1118	993	1254	1141
1-3-9	966	1217	1110	1027	1274	1168
1-3-10	959	1204	1100	1035	1268	1169
1-4-1	1018	1259	1161	1072	1300	1208
1-4-2	1016	1258	1159	1024	1257	1162
1-4-3	1020	1263	1164	976	1217	1119
1-4-4	1027	1270	1171	939	1192	1089
1-4-5	1034	1280	1182	933	1199	1091
1-4-6	1037	1287	1188	959	1233	1122

Compact	Minimum Temperature (°C)	Maximum Temperature (°C)	Averaged Temperature (°C)	Minimum Temperature (°C)	Maximum Temperature (°C)	Averaged Temperature (°C)
1-4-7	1037	1290	1190	1012	1282	1174
1-4-8	1036	1286	1186	1068	1323	1220
1-4-9	1027	1279	1178	1096	1340	1242
1-4-10	1019	1269	1167	1096	1333	1236
1-5-1	1040	1281	1189	1076	1314	1227
1-5-2	1041	1281	1190	1022	1268	1181
1-5-3	1041	1282	1192	975	1227	1137
1-5-4	1043	1286	1196	947	1204	1110
1-5-5	1047	1292	1203	956	1217	1118
1-5-6	1049	1299	1208	995	1259	1155
1-5-7	1051	1302	1211	1057	1310	1210
1-5-8	1048	1298	1208	1106	1347	1254
1-5-9	1045	1293	1203	1126	1362	1273
1-5-10	1042	1287	1196	1115	1350	1264
1-6-1	1040	1313	1203	1074	1332	1230
1-6-2	1041	1312	1203	1018	1284	1178
1-6-3	1041	1312	1203	972	1246	1136
1-6-4	1043	1312	1205	947	1231	1116
1-6-5	1046	1320	1211	956	1255	1133
1-6-6	1049	1324	1216	997	1299	1178
1-6-7	1051	1323	1217	1058	1346	1232
1-6-8	1048	1322	1214	1107	1381	1272
1-6-9	1045	1321	1211	1126	1391	1286
1-6-10	1042	1319	1208	1114	1375	1271
1-7-1	1058	1344	1234	1073	1347	1244
1-7-2	1057	1346	1234	1019	1302	1192
1-7-3	1057	1345	1232	979	1271	1156
1-7-4	1057	1343	1232	964	1267	1147
1-7-5	1060	1347	1237	984	1297	1175
1-7-6	1063	1349	1241	1031	1342	1223
1-7-7	1062	1350	1240	1088	1387	1272
1-7-8	1060	1348	1239	1129	1413	1306
1-7-9	1060	1348	1238	1141	1414	1311
1-7-10	1060	1347	1237	1121	1390	1288
1-8-1	1040	1345	1231	1021	1345	1222
1-8-2	1042	1347	1234	975	1302	1179
1-8-3	1042	1346	1233	955	1271	1153
1-8-4	1042	1344	1232	965	1270	1156

Compact	Minimum Temperature (°C)	Maximum Temperature (°C)	Averaged Temperature (°C)	Minimum Temperature (°C)	Maximum Temperature (°C)	Averaged Temperature (°C)
1-8-5	1042	1347	1233	1003	1299	1188
1-8-6	1043	1349	1234	1051	1344	1234
1-8-7	1042	1350	1234	1094	1389	1279
1-8-8	1041	1347	1233	1115	1412	1302
1-8-9	1040	1349	1233	1103	1414	1298
1-8-10	1040	1347	1232	1068	1388	1267
1-9-1	772	1280	1068	751	1266	1051
1-9-2	771	1285	1071	722	1233	1020
1-9-3	772	1286	1072	716	1214	1007
1-9-4	773	1286	1073	728	1224	1019
1-9-5	771	1286	1072	754	1255	1048
1-9-6	773	1286	1073	786	1294	1084
1-9-7	772	1284	1071	809	1328	1112
1-9-8	771	1283	1070	816	1343	1123
1-9-9	771	1282	1069	805	1335	1114
1-9-10	772	1280	1068	782	1305	1086
	Zero offset – July 15, 2018 (164A)			Best-fit offset – July 15, 2018 (164A)		
1-1-1	662	936	821	642	914	800
1-1-2	662	935	821	668	940	827
1-1-3	666	938	824	694	966	852
1-1-4	666	944	828	704	982	867
1-1-5	676	955	838	709	989	871
1-1-6	678	964	845	690	979	859
1-1-7	677	965	845	662	955	831
1-1-8	676	958	839	634	922	800
1-1-9	668	951	832	615	902	781
1-1-10	667	942	826	622	898	782
1-2-1	813	1059	950	783	1032	922
1-2-2	812	1057	949	818	1057	951
1-2-3	815	1060	951	849	1084	980
1-2-4	818	1067	957	867	1105	999
1-2-5	827	1077	967	871	1113	1006
1-2-6	833	1087	976	852	1108	996
1-2-7	834	1087	976	817	1082	966
1-2-8	829	1083	972	781	1052	933
1-2-9	822	1077	965	759	1031	911
1-2-10	816	1065	955	760	1020	906
1-3-1	899	1155	1046	865	1125	1014

Compact	Minimum Temperature (°C)	Maximum Temperature (°C)	Averaged Temperature (°C)	Minimum Temperature (°C)	Maximum Temperature (°C)	Averaged Temperature (°C)
1-3-2	899	1152	1044	897	1143	1039
1-3-3	899	1153	1045	928	1168	1066
1-3-4	904	1160	1051	951	1191	1089
1-3-5	912	1169	1060	958	1204	1100
1-3-6	918	1179	1069	944	1204	1094
1-3-7	919	1182	1071	911	1188	1070
1-3-8	915	1177	1067	876	1159	1039
1-3-9	909	1170	1060	851	1134	1014
1-3-10	902	1163	1052	846	1121	1004
1-4-1	963	1218	1116	925	1184	1080
1-4-2	961	1217	1114	949	1197	1098
1-4-3	961	1217	1114	977	1218	1121
1-4-4	966	1222	1120	1003	1243	1147
1-4-5	973	1229	1127	1017	1260	1164
1-4-6	978	1239	1136	1010	1269	1166
1-4-7	980	1242	1139	985	1260	1151
1-4-8	976	1237	1134	953	1234	1122
1-4-9	970	1231	1127	925	1208	1094
1-4-10	966	1224	1121	916	1188	1079
1-5-1	991	1243	1147	940	1203	1105
1-5-2	992	1244	1146	946	1209	1115
1-5-3	992	1244	1147	968	1227	1136
1-5-4	994	1248	1150	1000	1254	1164
1-5-5	996	1253	1154	1029	1279	1186
1-5-6	998	1257	1162	1043	1293	1198
1-5-7	997	1256	1162	1034	1288	1189
1-5-8	997	1256	1160	1008	1271	1167
1-5-9	995	1253	1156	978	1245	1138
1-5-10	993	1249	1151	952	1220	1114
1-6-1	991	1280	1164	939	1236	1117
1-6-2	992	1280	1165	942	1228	1116
1-6-3	992	1280	1166	959	1241	1132
1-6-4	994	1279	1166	992	1267	1161
1-6-5	996	1283	1170	1028	1301	1194
1-6-6	999	1287	1175	1044	1326	1216
1-6-7	997	1286	1173	1037	1331	1216
1-6-8	997	1286	1173	1016	1321	1201
1-6-9	995	1286	1173	984	1295	1173
1-6-10	993	1283	1169	954	1262	1139

Compact	Minimum Temperature (°C)	Maximum Temperature (°C)	Averaged Temperature (°C)	Minimum Temperature (°C)	Maximum Temperature (°C)	Averaged Temperature (°C)
1-7-1	1012	1315	1198	955	1269	1147
1-7-2	1013	1315	1199	945	1249	1132
1-7-3	1013	1316	1199	951	1256	1142
1-7-4	1011	1315	1198	988	1285	1173
1-7-5	1013	1316	1200	1033	1324	1213
1-7-6	1015	1317	1202	1063	1357	1245
1-7-7	1014	1316	1202	1073	1372	1259
1-7-8	1014	1315	1203	1058	1366	1251
1-7-9	1013	1316	1202	1024	1342	1221
1-7-10	1012	1314	1200	984	1302	1181
1-8-1	1001	1316	1201	943	1270	1150
1-8-2	1003	1318	1204	907	1250	1125
1-8-3	1002	1318	1203	905	1256	1126
1-8-4	1001	1318	1203	940	1285	1158
1-8-5	1002	1319	1204	997	1325	1205
1-8-6	1004	1318	1204	1048	1358	1245
1-8-7	1003	1316	1202	1079	1374	1267
1-8-8	1000	1315	1201	1077	1369	1263
1-8-9	1001	1317	1202	1046	1346	1236
1-8-10	1001	1314	1200	994	1305	1191
1-9-1	705	1259	1039	668	1217	1000
1-9-2	706	1263	1042	637	1193	973
1-9-3	705	1263	1041	631	1192	970
1-9-4	706	1262	1040	656	1219	995
1-9-5	705	1264	1042	695	1261	1036
1-9-6	708	1264	1043	735	1299	1073
1-9-7	707	1263	1043	758	1319	1097
1-9-8	707	1261	1042	760	1318	1097
1-9-9	706	1261	1041	741	1296	1076
1-9-10	706	1259	1039	706	1257	1038
	Zero offset – August 12, 2018 (164A)			Best-fit offset – August 12, 2018 (164A)		
1-1-1	652	947	824	660	954	831
1-1-2	652	946	824	625	917	795
1-1-3	656	950	826	599	893	769
1-1-4	659	962	835	592	897	769
1-1-5	669	974	845	615	927	794
1-1-6	670	981	852	650	968	834
1-1-7	669	978	849	685	1000	868



Compact	Minimum Temperature (°C)	Maximum Temperature (°C)	Averaged Temperature (°C)	Minimum Temperature (°C)	Maximum Temperature (°C)	Averaged Temperature (°C)
1-1-8	667	971	843	709	1017	887
1-1-9	658	960	834	706	1010	883
1-1-10	656	952	827	692	988	863
1-2-1	808	1070	956	813	1071	958
1-2-2	808	1068	955	767	1029	915
1-2-3	810	1073	959	734	1007	889
1-2-4	818	1085	970	733	1018	894
1-2-5	828	1100	982	764	1058	929
1-2-6	833	1112	990	811	1107	977
1-2-7	830	1111	988	858	1142	1018
1-2-8	825	1099	979	885	1153	1035
1-2-9	815	1088	969	880	1144	1028
1-2-10	811	1077	961	855	1112	1000
1-3-1	893	1161	1048	889	1151	1040
1-3-2	891	1159	1047	838	1110	996
1-3-3	894	1164	1051	809	1093	974
1-3-4	902	1173	1060	814	1110	986
1-3-5	914	1187	1073	856	1154	1028
1-3-6	921	1198	1084	910	1206	1082
1-3-7	921	1203	1086	961	1245	1127
1-3-8	912	1194	1076	983	1253	1140
1-3-9	902	1181	1065	972	1235	1125
1-3-10	896	1170	1055	937	1198	1088
1-4-1	953	1222	1114	934	1197	1092
1-4-2	951	1220	1113	885	1160	1050
1-4-3	954	1225	1117	864	1151	1036
1-4-4	960	1235	1125	877	1178	1057
1-4-5	970	1246	1137	925	1226	1105
1-4-6	976	1254	1145	981	1275	1158
1-4-7	979	1256	1148	1032	1309	1200
1-4-8	973	1249	1142	1050	1313	1210
1-4-9	963	1239	1131	1029	1289	1187
1-4-10	956	1229	1121	987	1246	1143
1-5-1	975	1245	1143	915	1203	1103
1-5-2	976	1246	1143	873	1170	1065
1-5-3	978	1250	1147	873	1171	1061
1-5-4	982	1257	1154	912	1207	1093
1-5-5	988	1266	1163	976	1262	1147
1-5-6	992	1274	1171	1032	1313	1202

Compact	Minimum Temperature (°C)	Maximum Temperature (°C)	Averaged Temperature (°C)	Minimum Temperature (°C)	Maximum Temperature (°C)	Averaged Temperature (°C)
1-5-7	991	1273	1170	1074	1339	1236
1-5-8	987	1268	1165	1077	1337	1238
1-5-9	982	1260	1157	1037	1305	1208
1-5-10	976	1251	1148	974	1255	1156
1-6-1	975	1279	1159	908	1218	1098
1-6-2	976	1277	1159	870	1189	1065
1-6-3	978	1281	1162	872	1202	1071
1-6-4	982	1288	1168	913	1250	1116
1-6-5	988	1298	1177	979	1311	1180
1-6-6	992	1304	1184	1040	1360	1235
1-6-7	991	1303	1183	1078	1380	1263
1-6-8	987	1299	1179	1077	1369	1256
1-6-9	982	1294	1173	1036	1330	1216
1-6-10	977	1286	1165	969	1272	1154
1-7-1	994	1308	1189	901	1230	1108
1-7-2	993	1311	1189	873	1214	1083
1-7-3	995	1315	1193	887	1239	1103
1-7-4	999	1321	1199	944	1295	1159
1-7-5	1005	1328	1206	1018	1356	1227
1-7-6	1009	1334	1213	1079	1403	1281
1-7-7	1009	1335	1213	1110	1417	1302
1-7-8	1004	1330	1208	1094	1396	1284
1-7-9	1001	1323	1203	1041	1348	1233
1-7-10	996	1315	1196	962	1285	1165
1-8-1	984	1310	1192	865	1230	1097
1-8-2	983	1313	1194	851	1215	1083
1-8-3	985	1317	1198	889	1243	1114
1-8-4	989	1324	1203	964	1301	1177
1-8-5	992	1330	1207	1040	1360	1243
1-8-6	997	1335	1212	1090	1404	1290
1-8-7	998	1336	1214	1103	1418	1305
1-8-8	994	1331	1209	1068	1397	1277
1-8-9	989	1324	1203	997	1347	1218
1-8-10	986	1317	1197	919	1284	1149
1-9-1	677	1260	1032	591	1177	949
1-9-2	678	1261	1034	589	1169	945
1-9-3	680	1265	1038	621	1201	976
1-9-4	683	1270	1041	673	1256	1028

Compact	Minimum Temperature (°C)	Maximum Temperature (°C)	Averaged Temperature (°C)	Minimum Temperature (°C)	Maximum Temperature (°C)	Averaged Temperature (°C)
1-9-5	684	1275	1046	721	1311	1082
1-9-6	690	1280	1050	752	1348	1115
1-9-7	688	1281	1050	754	1355	1120
1-9-8	685	1277	1046	728	1331	1094
1-9-9	681	1271	1041	680	1281	1045
1-9-10	680	1265	1036	627	1221	989

## **Appendix B**

### **Capsule 2 Compact Temperatures for Zero and Best-fit Offset Calculated for Selected Dates**

Table 16. Capsule 2 compact temperature (minimum, maximum, and average) for zero and best-fit offset, calculated for selected dates during the AGR-5/6/7 irradiation.

Compact	Minimum Temperature (°C)	Maximum Temperature (°C)	Averaged Temperature (°C)	Minimum Temperature (°C)	Maximum Temperature (°C)	Averaged Temperature (°C)
	Zero offset – March 3, 2018 (162B)			Best-fit offset – March 3, 2018 (162B)		
2-1-1	602	850	759	601	855	760
2-1-2	598	846	754	556	801	710
2-1-3	602	853	760	595	842	751
2-1-4	604	854	761	633	888	793
2-2-1	767	912	848	768	925	857
2-2-2	764	910	846	710	871	802
2-2-3	769	918	853	751	898	836
2-2-4	770	917	852	809	947	886
2-3-1	814	934	884	826	957	902
2-3-2	813	934	885	769	910	852
2-3-3	818	942	891	793	913	865
2-3-4	818	940	890	851	959	915
2-4-1	812	935	887	850	961	916
2-4-2	812	935	887	802	917	872
2-4-3	816	942	894	768	911	856
2-4-4	814	939	891	813	956	899
2-5-1	779	917	859	829	952	900
2-5-2	777	919	858	786	913	861
2-5-3	782	925	864	716	881	812
2-5-4	782	922	863	757	921	852
2-6-1	764	891	838	820	936	888
2-6-2	764	890	837	786	902	857
2-6-3	769	897	844	689	839	778
2-6-4	770	897	844	720	876	812
2-7-1	738	873	817	791	924	868
2-7-2	737	874	818	772	902	850
2-7-3	743	880	823	655	812	748
2-7-4	744	883	824	673	841	773
2-8-1	600	839	753	641	887	797
2-8-2	597	838	751	631	873	785
2-8-3	601	845	757	530	773	686
2-8-4	603	847	758	539	791	700
	Zero offset – October 8, 2018 (164B)			Best-fit offset – October 8, 2018 (164B)		
2-1-1	605	856	763	627	885	788
2-1-2	601	851	758	573	824	730

Compact	Minimum Temperature (°C)	Maximum Temperature (°C)	Averaged Temperature (°C)	Minimum Temperature (°C)	Maximum Temperature (°C)	Averaged Temperature (°C)
2-1-3	605	858	765	571	819	728
2-1-4	607	859	765	625	878	784
2-2-1	771	917	854	803	949	885
2-2-2	768	916	852	734	899	828
2-2-3	774	924	858	726	883	816
2-2-4	774	923	858	793	933	872
2-3-1	819	940	890	854	969	921
2-3-2	818	940	890	798	941	882
2-3-3	823	948	897	776	910	856
2-3-4	823	946	896	829	943	897
2-4-1	817	941	893	845	970	921
2-4-2	817	941	893	835	950	904
2-4-3	821	948	899	783	911	863
2-4-4	819	945	896	786	937	878
2-5-1	783	923	864	804	949	888
2-5-2	782	925	864	828	948	897
2-5-3	787	931	870	750	897	836
2-5-4	787	928	868	725	898	825
2-6-1	769	897	844	778	917	860
2-6-2	769	896	843	828	938	894
2-6-3	774	903	849	741	873	820
2-6-4	775	903	850	687	848	781
2-7-1	743	879	823	740	891	829
2-7-2	742	880	823	814	938	885
2-7-3	747	887	829	719	862	806
2-7-4	749	889	830	640	811	741
2-8-1	604	844	758	599	847	757
2-8-2	601	844	756	658	905	814
2-8-3	605	851	762	589	832	745
2-8-4	607	852	763	511	762	671
	Zero offset – April 20, 2020 (168A)			Max-temperature offset – April 20, 2020 (168A)		
2-1-1	571	915	795	424	719	614
2-1-2	571	915	796	555	899	776
2-1-3	576	923	803	640	1012	884
2-1-4	574	922	801	553	898	775
2-2-1	782	966	892	519	746	660
2-2-2	782	967	892	743	951	870
2-2-3	787	977	900	911	1083	1009

Compact	Minimum Temperature (°C)	Maximum Temperature (°C)	Averaged Temperature (°C)	Minimum Temperature (°C)	Maximum Temperature (°C)	Averaged Temperature (°C)
2-2-4	786	974	898	738	948	866
2-3-1	821	983	920	529	753	673
2-3-2	822	982	920	781	966	898
2-3-3	828	993	929	971	1107	1050
2-3-4	826	990	927	772	964	893
2-4-1	809	983	919	477	753	658
2-4-2	809	982	919	766	966	896
2-4-3	818	994	930	984	1110	1060
2-4-4	815	991	927	755	964	892
2-5-1	772	964	889	401	707	587
2-5-2	773	965	890	729	950	868
2-5-3	781	978	901	965	1105	1047
2-5-4	778	974	897	716	948	861
2-6-1	764	941	872	396	662	564
2-6-2	765	942	874	722	929	852
2-6-3	773	955	885	954	1092	1035
2-6-4	771	951	882	710	925	846
2-7-1	751	932	863	399	657	564
2-7-2	750	933	863	708	919	841
2-7-3	757	945	872	922	1079	1014
2-7-4	755	943	870	696	916	834
2-8-1	590	912	806	349	654	551
2-8-2	589	912	805	565	897	783
2-8-3	593	922	813	695	1042	925
2-8-4	593	920	811	559	894	779